UNCLASSIFIED

GEMP-29A

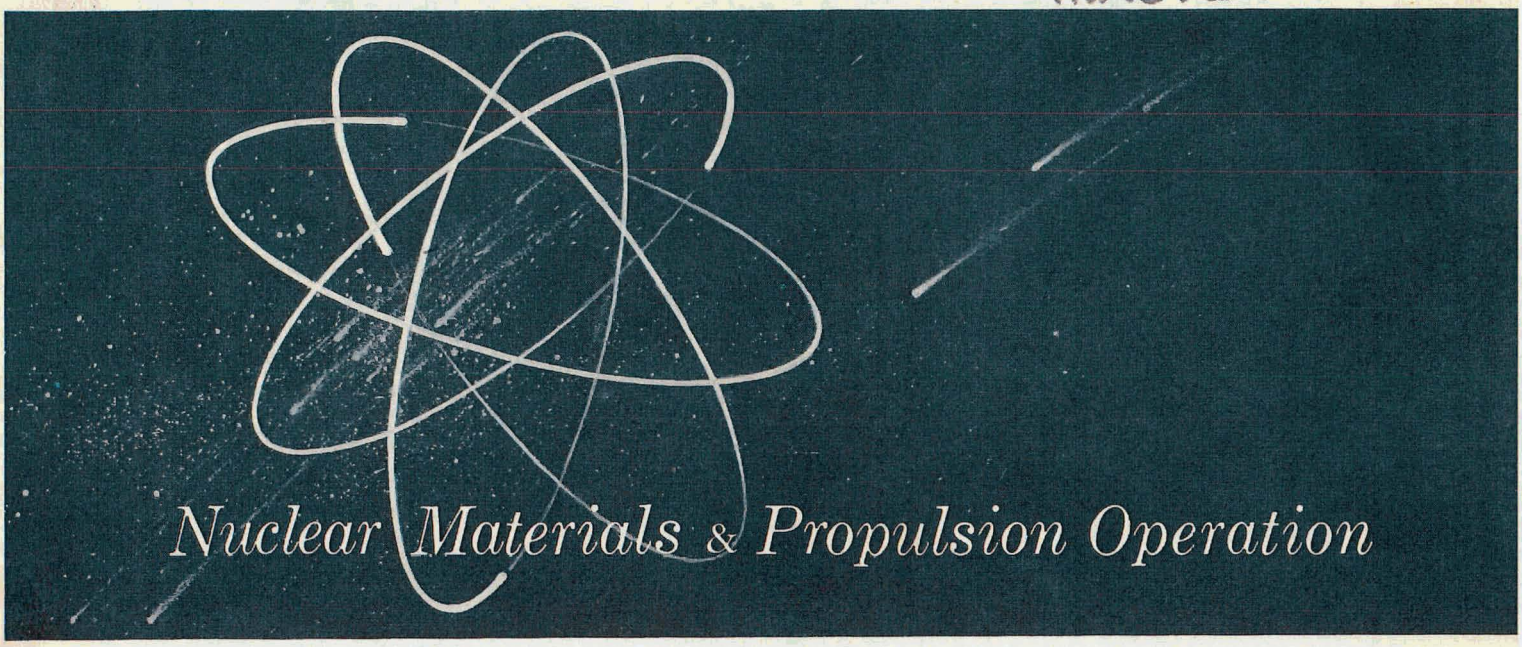

High-Temperature Materials Program

Progress Report No. 29, Part A

November 30, 1963

ADVANCED TECHNOLOGY SERVICES

GENERAL ELECTRIC

UNCLASSIFIED

DISCLAIMER

LEGAL NOTICE

Printed in USA. Price $2.00 Available from the

Office of Technical Services

U. S. Department of Commerce

Washington 25, D. C.

GEMP-29A
UC-25 Metals, Ceramics,
and Materials
TID-4500 (25th Ed.)

High-Temperature Materials Program
Progress Report No. 29, Part A

November 30, 1963

United States Atomic Energy Commission Contract No. AT(40-1)-2847

NUCLEAR MATERIALS and PROPULSION OPERATION
ADVANCED TECHNOLOGY SERVICES
GENERAL ELECTRIC
Cincinnati 15, Ohio

DISTRIBUTION

EXTERNAL

AEC Headquarters
- E. M. Douthett
- I. Hoffman
- T. W. McIntosh
- F. C. Schwenk
- J. M. Simmons (2)
- W. R. Voight
- G. W. Wensch
- M. J. Whitman

AEC, OROO
- D. F. Cope (3)
- D. S. Zachry, Jr.

AEC, CANEL Project Office
- A. J. Alexander

AEC, CAO
- C. L. Karl
- J. F. Weissenberg

AEC, SAN
- Lt. Col. J. B. Radcliffe, Jr.

AEC, MCR Project Office
- S. Meyers

General Atomic
- G. B. Engle
- W. C. Moore

Pratt and Whitney Aircraft (CANEL)
- L. M. Raring (3)

ORNL
- R. E. Blanco
- R. E. Clausing
- D. A. Douglas, Jr.
- W. R. Grimes
- W. O. Harms
- W. D. Manly
- A. J. Miller
- N. W. Rosenthal

BMI
- R. W. Dayton

LASL
- R. D. Baker

Lawrence Radiation Laboratory
- R. E. Batzel
- C. Cline
- A. J. Rothman

Atomics International
- R. Balent
- S. C. Carniglia

Wah Chang Corp.
- S. Worchester

W. R. Grace and Company
- F. T. Fitch

NASA Headquarters
- J. J. Lynch

NASA, Lewis Research Center
- J. W. Creagh
- N. Saunders

INTERNAL

- E. A. Aitken
- W. G. Baxter
- J. R. Beeler
- J. C. Blake
- B. Blumberg
- H. C. Brassfield
- R. W. Brisken
- J. J. Caldwell, HAPO
- V. P. Calkins
- C. L. Chase (3)
- C. G. Collins
- E. S. Collins
- J. F. Collins
- P. K. Conn
- J. B. Conway
- E. B. Delson
- H. S. Edwards
- E. W. Filer
- P. N. Flagella
- J. E. Fox
- E. S. Funston
- M. Goldstein
- G. F. Hamby
- J. O. Hibbits
- L. D. Jordan
- G. Korton
- M. C. Leverett, HAPO
- W. H. Long
- R. A. Lutter
- J. E. McConnelee
- L. R. McCreight, MSD
- J. A. McGurty
- C. I. McVey
- J. W. Morfitt
- J. Moteff
- R. E. Motsinger
- G. T. Muehlenkamp
- C. E. Niemeyer
- W. E. Niemuth
- G. W. Pomeroy
- W. Z. Prickett
- R. Pustell, Lynn
- R. C. Rau
- R. Reid
- F. C. Robertshaw
- C. P. Schiltz
- E. J. Schmidt, ATS
- M. T. Schoenberger
- R. J. Spera
- H. R. Stephan
- G. Thornton
- P. P. Turner
- F. O. Urban
- G. R. Van Houten
- H. Wagner
- J. F. White
- D. B. Williams
- O. G. Wolke
- R. E. Wood
- Library (10)

CONTENTS

FIGURES

Page

TABLES

CONVERSION TABLE

To Convert From	To	Multiply By
Atmospheres	Pounds/inch^2	14.7
Calories (mean)	Btu (mean)	0.00397
Calories/gram-^oC	Btu/pound-^oF	1.0
Calories/sec-cm-^oC	Btu/hr-ft-^oF	241.8
Calories/sec-cm^2	Btu/hr-ft^2	1.32 x 10^4
Calories/sec-cm^2-^oC	Btu/hr-ft^2-^oF	7370
Centimeters	Feet	0.03281
	Inches	0.3937
Cubic centimeters	Cubic feet	3.531 x 10^{-5}
	Cubic inches	0.06103
Grams	Pounds	0.002205
Grams/cm^3	Pounds/ft^3	62.43
Grams/cm^2	psi	0.01422
Kilograms	Pounds	2.205
Kilograms/cm^2	Atmospheres	0.9678
	Pounds/ft^2	2.048
	Pounds/inch^2	14.22
Kilowatts	Btu/sec	0.948
Liters	Cubic feet	0.0353
Meters	Inches	39.37
Millimeters of mercury	Atmospheres	0.001316
Square centimeters	Square feet	0.001076
	Square inches	0.155
Torr	mm of Hg	1.0
	Atmospheres	0.001316
Watts/cm-^oC	Btu/hr-ft-^oF	57.8
Watt-seconds	Btu	0.000948
Watts/cm^2-^oC	Btu/hr-ft^2	3170
Watts/cm^2-^oC	Btu/hr-ft^2-^oF	1760
Centimeters/sec	Feet/sec	0.03281
Meters/sec	Feet/sec	3.281

1. INTRODUCTION AND SUMMARY

Introduction

This report is the unclassified portion of the twenty-ninth in a series of monthly reports of the work in process on materials development for the Atomic Energy Commission under Contract AT(40-1)-2847.

Included is a summary of the work from August 15, 1963 to October 15, 1963, on two of the sixteen specific development programs in process. Five of the remaining programs are reported in the classified portion of this report, GEMP-29, Part B. The other nine, involving the development of ceramic fuel materials, are reported in alternate months.

Summary

HIGH-TEMPERATURE REACTOR MATERIALS FABRICATION RESEARCH (57003)

One to 10 hour stress-rupture and creep tests of arc-melted molybdenum TZM at 2000°C and 2200°C in a hydrogen atmosphere show this material to be stronger than arc-melted molybdenum. This difference is decreased as the temperature is increased.

When tested at 2600°C, powder metallurgy W - 25Re (at. %), sintered at approximately 2400°C, has a higher rupture strength in hydrogen than in argon. Heat treatment at 2800°C prior to stress-rupture testing yields similar results at 2600°C in hydrogen or argon.

The correlation of the stress-rupture time (t_R) and minimum creep rate (mcr) data yields the empirical relationship $t_R \times mcr = c$ (c is a constant) for the refractory metals, tungsten, molybdenum, tantalum, and some of their alloys with W - 25Re being a notable exception.

The development program on fabricating high-quality W - 25Re alloys has shown that the agglomeration of fine tungsten powders must be prevented to minimize tungsten agglomerates in finished sheet.

EFFECTS OF RADIATION ON HIGH-TEMPERATURE ALLOYS (57004)

The fabrication of an elevated-temperature cartridge for irradiating refractory metals was completed and shipped to ITS for the October ETR cycle.

Creep-rupture testing of irradiated cold-worked tungsten flat specimens continued. Several specimens were annealed at 1900°C for 1 hour and then creep-rupture tested at 1100°C. The radiation-induced hardening was not completely removed by this treatment as shown by comparison with a corresponding unirradiated specimen which was annealed at the same time.

Tungsten resistance specimens were annealed for 1 hour at 1900°C with little change in resistance being noted for the high-irradiation specimen (3.3×10^{19} nvt, $E_n \geq 1$ Mev) when compared to corresponding data obtained after annealing between 1000° and 1650°C.

Testing of A-286 alloy specimens containing various additions of natural boron continued. The specimens having the lowest boron concentration (0.00085%) showed the largest reduction in rupture life because of irradiation. Specimens having the highest boron concentration (0.010%) did not show any effect of irradiation when compared on the basis of rupture life; however, there was a marked reduction in ductility as indicated by elongation.

Computer calculations were made on the initial damage state produced in finite, neutron-irradiated iron specimens. A Monte Carlo calculation was used to compute the number of primary knock-on atoms produced per incident neutron and their energy spectrum.

2. HIGH-TEMPERATURE REACTOR MATERIALS FABRICATION RESEARCH

(57003)

The purpose of this program is to develop and evaluate methods of preparing and joining refractory metals and alloys and other high-temperature materials for use as fueled and non-fueled high-temperature (1000° to 3000°C) reactor components.

STRESS-RUPTURE STUDIES

Stress-rupture and creep measurements on refractory metals and their alloys in the temperature range of 2000° to 2800°C is an important part of this work. During this report period the molybdenum alloy TZM was initially evaluated.

Molybdenum Alloy TZM

TZM (molybdenum - 0.5% Ti - 0.1% Zr) is a commercial arc-melted material developed to improve the strength of molybdenum primarily in the 900° to 1400°C temperature range and to increase the recrystallization temperature. In the 900° to 1400°C temperature range the 10-hour rupture strength is 2 to 4 times greater than that of arc-melted molybdenum. Published ultimate tensile strength data show the difference in tensile strength between TZM and molybdenum to decrease with increasing temperature to 1400°C, but no data are available beyond this temperature.

TZM alloy was creep-rupture tested at 2000°C and 2200°C in a hydrogen atmosphere to determine if the material continued to show greater rupture strength over molybdenum at these temperatures. The material used was commercial, arc-melted, recrystallized 0.051-centimeter-thick sheet. The test samples had a gage section 2.54 centimeters long and 0.64 centimeter wide. Table 2.1 lists the chemical analysis of the material and samples before and after test. It can be seen that in all cases the amounts of titanium and zirconium are below the nominal composition specified for TZM (0.5% Ti - 0.1% Zr). No significant loss of these materials occurred nor were the samples contaminated during the test. Table 2.2 lists the test conditions and results and Figure 2.1 is a photograph of the tested sheet samples. Figure 2.2 is a photomicrograph of the recrystallized, as-received material. Figure 2.3 is a photomicrograph of a sample tested for 4.23 hours at 2000°C. The grain size is predominantly large (425 to 450 microns) with some duplexing, and it appears to be single phase. Some grain-boundary voids appear throughout the sample. Figure 2.4 is a photomicrograph of a sample tested for 5.97 hours at 2200°C. The grain size is very large (700 to 900 microns) and it is single phase. It appears that the additional 200°C promotes additional grain growth and leads to a more uniform grain size. The grain structure of TZM at 2200°C is very similar to the grain size of molybdenum at the same temperature.

Results of creep-rupture testing of TZM at 2000°C and 2200°C in a hydrogen atmosphere are shown in Figures 2.5 and 2.6. For comparison, curves previously developed for pure

TABLE 2.1

CHEMICAL ANALYSIS OF MOLYBDENUM-TZM SAMPLES

	Composition, ppm																
	O_2[a]	H_2[a]	N_2[a]	C[b]	Ti[c]	Zr[c]	W[c]	Si[c]	Fe[c]	Al[c]	V[c]	Mn[c]	Cr[c]	Ta[c]	Cu[c]	Ca[c]	Ni[c]
As-received (per vendor)	-	-	-	310	4200	580	-	35	85	-	-	-	-	-	-	-	10
As-received	76.1	6.5	6.9	243	3600	600	<500	30	70	<10	-	<5	<10	-	<10	<10	<10
After testing 1.0 hr at 2000°C	-	-	-	55	-	-	-	-	-	-	-	-	-	-	-	-	-
After testing 4.2 hr at 2000°C	49.3	6.0	7.3	-	4300	500	400	<100	<100	<50	<100	<50	-	<500	<50	<10	-
After testing 1.7 hr at 2200°C	-	-	-	27	-	-	-	-	-	-	-	-	-	-	-	-	-
After testing 6.0 hr at 2200°C	20.2	1.5	5.7	-	4200	400	400	<100	<100	<50	<100	<50	-	<500	<50	<10	-

[a]Vacuum fusion analysis.
[b]Conductometric carbon analysis.
[c]Semi-quantitative spectrographic analysis.

TABLE 2.2

STRESS-RUPTURE TEST RESULTS FOR MOLYBDENUM-TZM

Temperature, °C	Atmosphere	Stress, kg/mm^2	Time To Rupture, hr	Percent Elongation In 2.54 cm Gage Length	Linear Creep Rate, min^{-1}
2000	H_2	0.844	4.23	41	7.10×10^{-4}
2000	H_2	1.125	1.01	45	3.84×10^{-3}
2200	H_2	0.316	5.97	51	8.00×10^{-4}
2200	H_2	0.366	3.44	52	1.40×10^{-3}
2200	H_2	0.422	1.71	74	3.29×10^{-3}

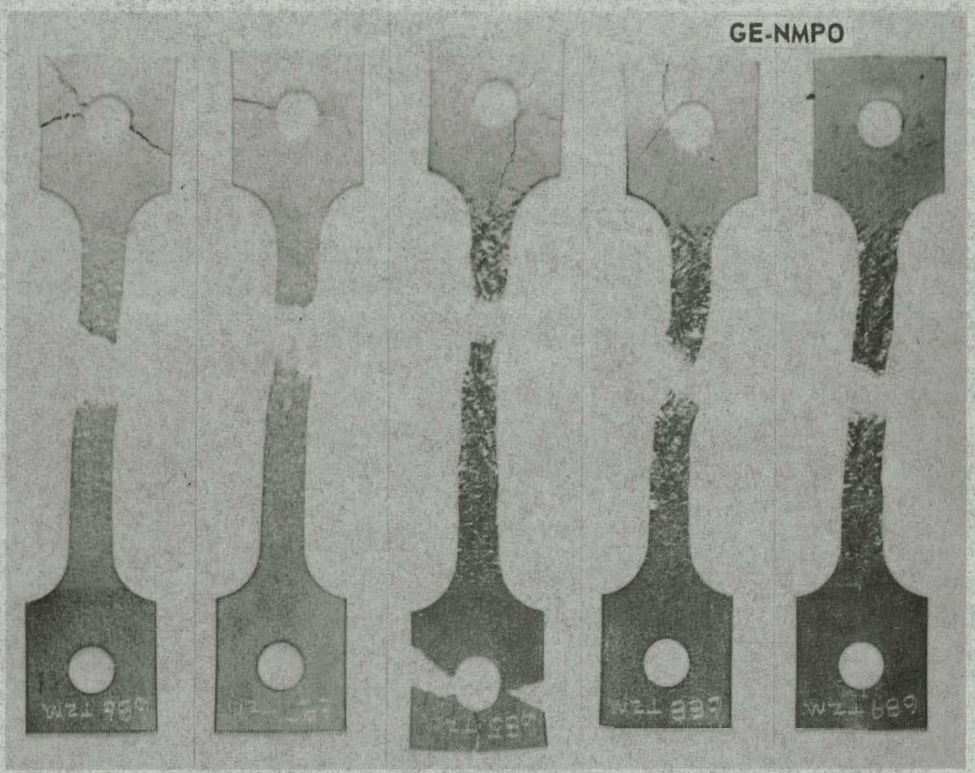

TEST TEMPERATURE, °C	2000	2000	2200	2200	2200
INITIAL STRESS, psi	1200	1600	600	450	520
TIME TO RUPTURE, hr	4.23	1.01	1.71	5.97	3.44
PERCENT OF ELONGATION WITH 1 INCH GAGE LENGTH	41.0	45.0	73.5	51.0	51.5

Fig. 2.1 – Post-test condition of molybdenum–TZM stress-rupture specimens 0.050-centimeter-thick sheet tested in hydrogen

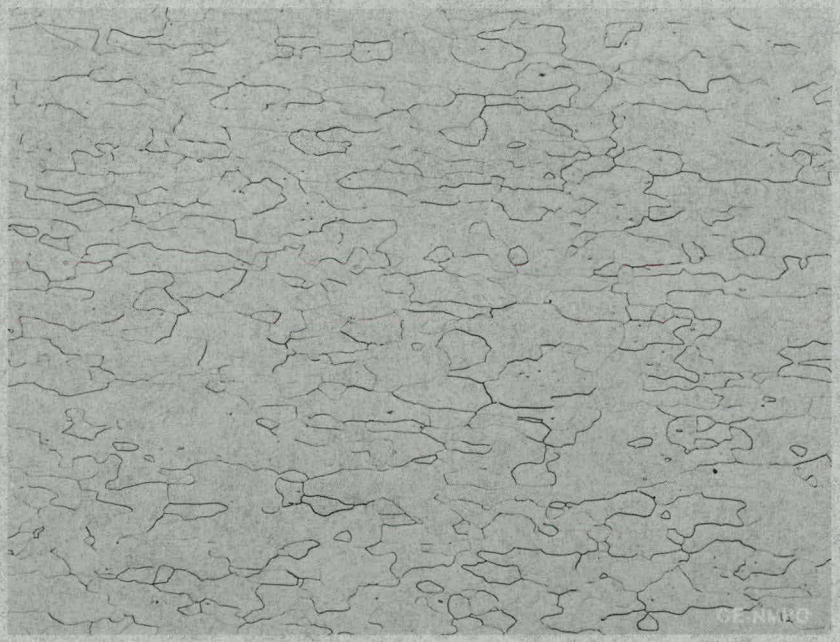

Neg. 3060, ETCHED 250 X

Fig. 2.2 – Photomicrograph of as-received recrystallized molybdenum – TZM

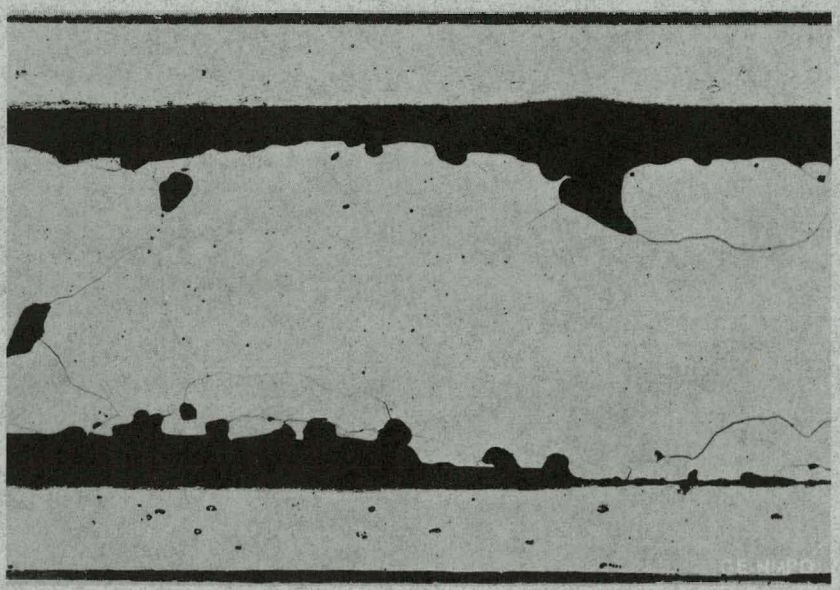

Neg. 3455, ETCHED 100 X

Fig. 2.3 – Photomicrograph of molybdenum – TZM after 4.23 hours at 2000°C and 0.844-kg/mm^2 stress in a hydrogen atmosphere

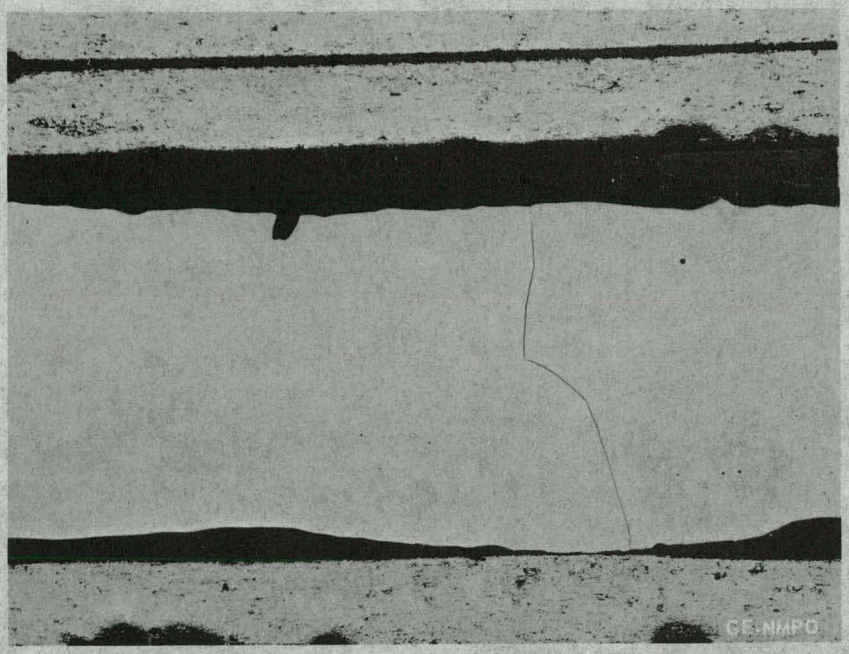

Fig. 2.4 – Photomicrograph of molybdenum – TZM after 5.97 hours at 2200°C and 0.316-kg/mm^2 stress in a hydrogen atmosphere

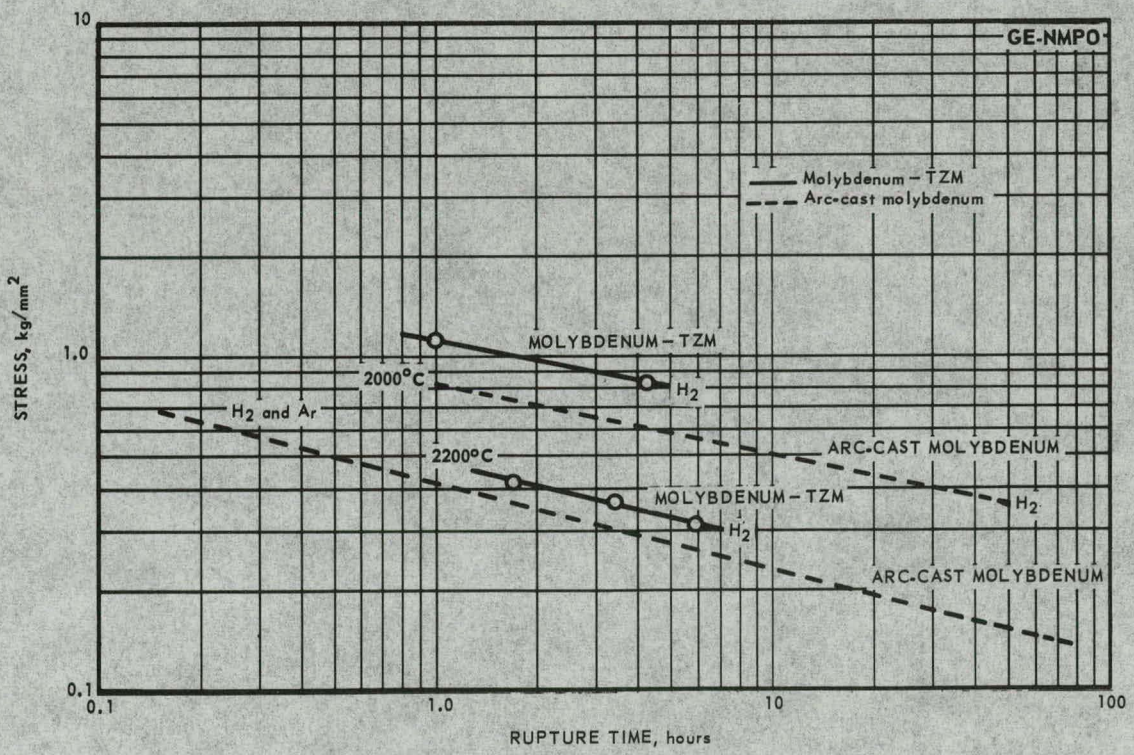

Fig. 2.5 – Stress-rupture data for molybdenum-TZM and arc-cast molybdenum

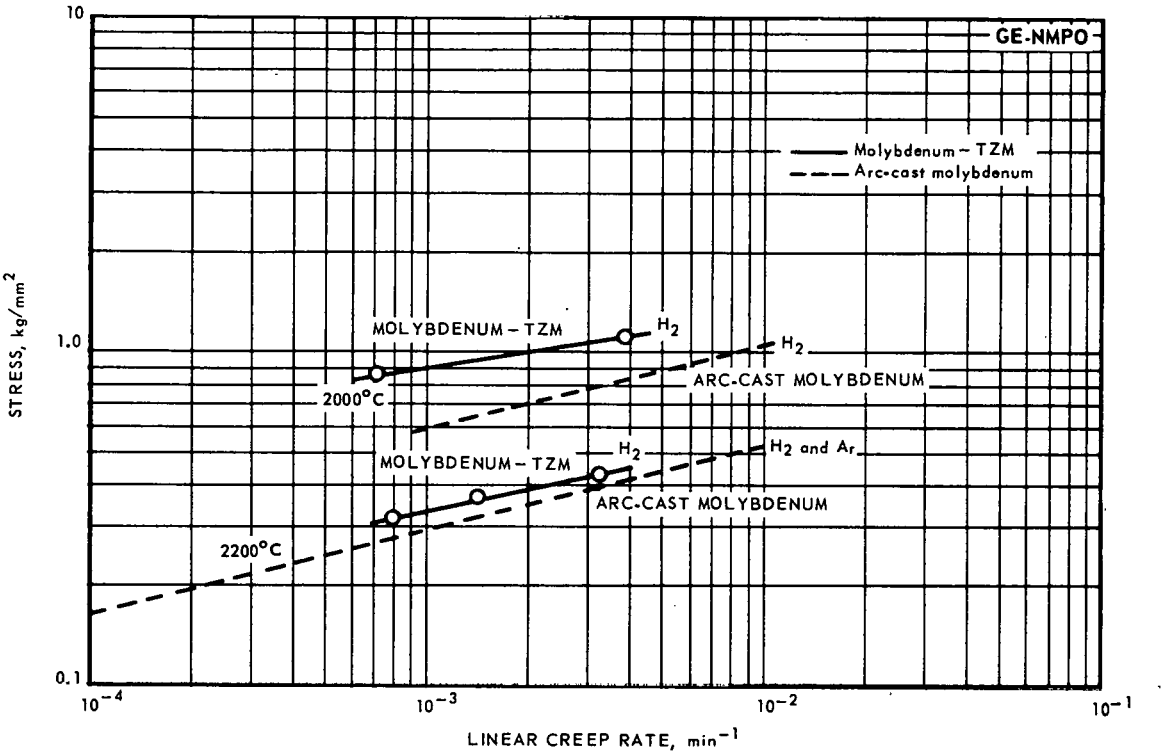

Fig. 2.6 – Stress versus creep rate for molybdenum-TZM and arc-cast molybdenum

arc-melted molybdenum are also shown. It can be seen from Figure 2. 5 that the rupture strength for TZM is greater than molybdenum at both 2000°C and 2200°C but that the difference is less at 2200°C. Figure 2. 6 shows that TZM is much more creep resistant than molybdenum at 2000°C but that this difference is much smaller at 2200°C.

This stress-rupture data and data from the literature indicate that the additions of Ti and Zr to Mo have a strengthening effect up to about 2000°C but the effect is negligible at 2200°C. Based on total elongations of the samples at rupture, TZM exhibits the same order of magnitude of ductility as arc-cast molybdenum at these temperatures.

Tungsten - 25 Rhenium

Stress-rupture and creep test results of sintered W - 25Re at 2400°C and 2600°C in hydrogen and argon atmospheres were presented previously.* It was shown that the material has a greater rupture strength and is more creep resistant in a hydrogen atmosphere than in an argon atmosphere at both 2400°C and 2600°C.

During this report period, creep-rupture tests were performed at 2600°C in both hydrogen and argon atmospheres with certain pre-test heat treatment of the samples. These heat treatments were performed in an attempt to identify the reason for the different rupture strengths measured in the two atmospheres. Table 2. 3 lists the tests performed with the results shown in Figures 2. 7 and 2. 8.

Two samples were heat treated at 2600°C in an argon atmosphere, one for 1 hour and the other for 4 hours, and then tested at 2600°C in an argon atmosphere. It can be seen from Figures 2. 7 and 2. 8 that neither the rupture strength nor the creep rate were significantly affected when compared to results of samples not heat treated. Two additional

*"High-Temperature Materials Program Progress Report No. 27, Part A," GE-NMPO, GEMP-27A, September 30, 1963, p. 11.

TABLE 2.3

2600°C STRESS-RUPTURE TEST RESULTS FOR SINTERED W - 25Re

Heat Treatment			Test Conditions and Results				
Temperature, °C	Time, hr	Atmosphere	Stress, kg/mm^2	Atmosphere	Time To Rupture, hr	Linear Creep Rate, min^{-1}	Percent Elongation In 2.54 cm Gage Length
2600	4	H_2	0.60	H_2	2.6	2.2×10^{-4}	8
2600	1	Ar	0.60	Ar	0.7	8.2×10^{-4}	8
2600	4	Ar	0.60	Ar	1.0	8.8×10^{-4}	15
2800	1	Ar	0.56	Ar	2.5	4.9×10^{-4}	13
2800	1	H_2	0.56	Ar	2.5	1.9×10^{-4}	6

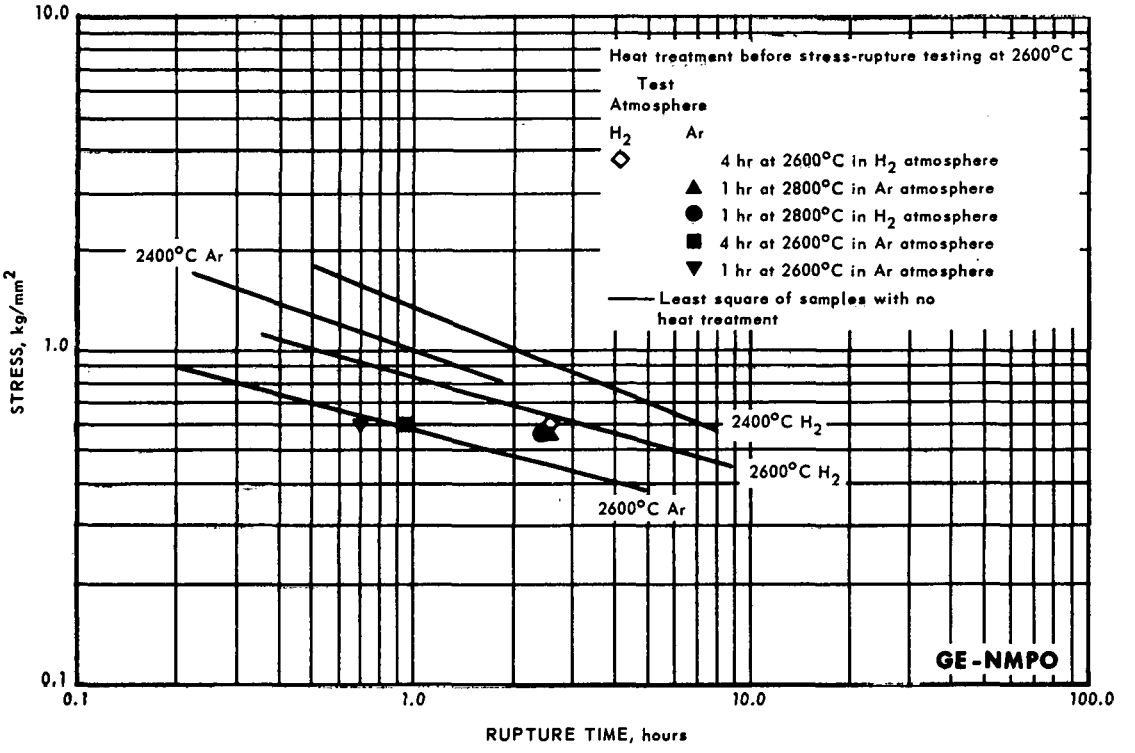

Fig. 2.7 – Stress-rupture data for W – 25Re

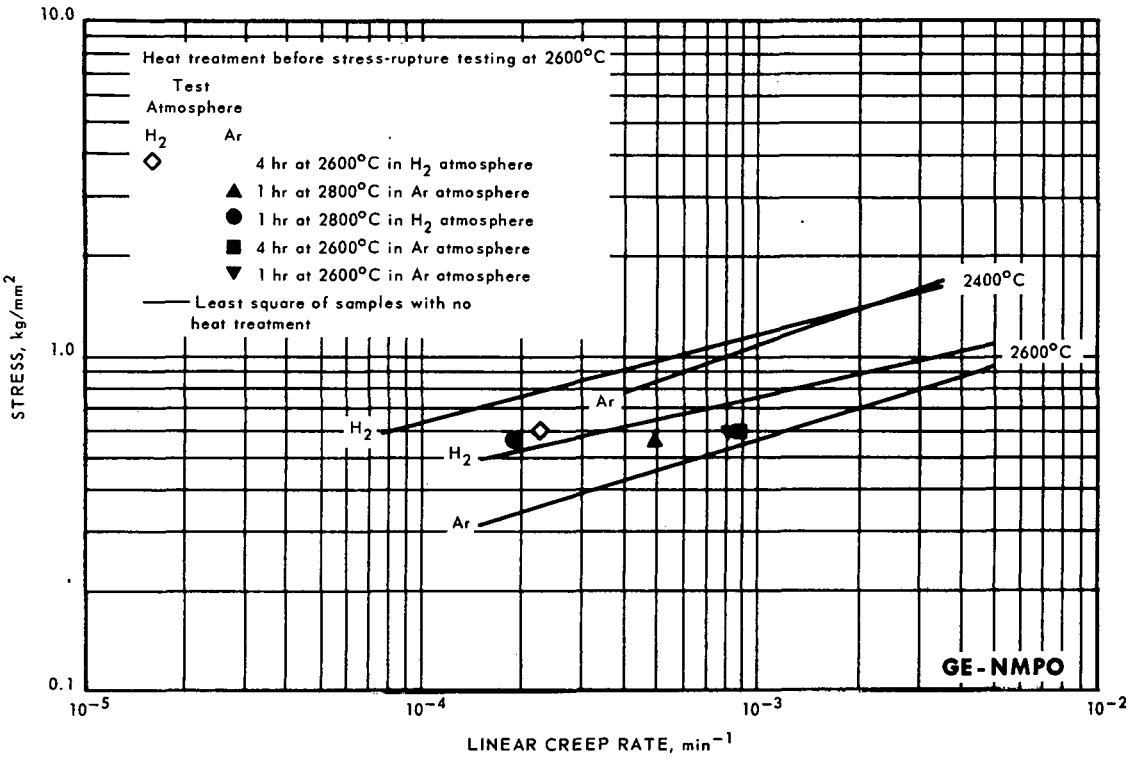

Fig. 2.8 – Stress versus creep rate for W – 25Re

samples were heat treated at 2800°C for 1 hour, one in hydrogen and the other in an argon atmosphere. They were then creep-rupture tested at 2600°C in argon; the results were identical. In both samples, the rupture strength was increased and the creep rate decreased indicating a strengthening of the material. A fifth sample was heat treated at 2600°C in hydrogen for 4 hours and then tested at 2600°C in hydrogen. No significant difference was observed when compared to results of samples not heat treated and tested in hydrogen at 2600°C.

This series of tests indicates that the 2600°C rupture strength of W - 25Re, sintered at approximately 2400°C (per vendor) will be greater in hydrogen than in argon if no additional heat treatment is employed. It is believed that testing at 2600°C in a hydrogen atmosphere (reducing) promotes additional sintering which increases the strength whereas an argon atmosphere (inert) does not. Additional tests are planned to confirm this.

Tungsten

Stress-rupture and creep test results of sintered tungsten, W(2), at 2400°C and 2800°C in hydrogen and argon atmospheres were previously reported.* Additional tests were performed during this report period at 2200°C as well as tests of samples heat treated and tested at 2400°C. The test data are tabulated in Table 2. 4 and the results shown in Figures 2. 9 and 2. 10 along with the curves presented in the previous report.

Neither the stress-rupture nor the creep curves at 2400°C appear to be consistent with those developed at 2200°C and 2800°C. Although the actual sintering temperature for the material could not be obtained from the vendor, indications are that it is between these two temperatures since similar rupture strengths were obtained in both hydrogen and

*"High-Temperature Materials Program Progress Report No. 25, Part A," GE-NMPO, GEMP-25A, July 31, 1963, p. 9.

TABLE 2.4

STRESS-RUPTURE TEST RESULTS FOR SINTERED TUNGSTEN, W(2)

Temperature, °C	Atmosphere	Stress, kg/mm^2	Time To Rupture, hr	Percent Elongation In 2.54 cm Gage Length	Linear Creep Rate, min^{-1}
2200	H_2	1.406	6.27	30	5.25×10^{-4}
		1.547	4.18	21	5.63×10^{-4}
		1.687	2.15	26	1.17×10^{-3}
		1.828	1.30	24	2.93×10^{-3}
2200	Ar	1.265	9.31	14	7.87×10^{-5}
		1.828	0.99	30	4.00×10^{-3}
2400	H_2	1.054	3.42[a]	17	3.94×10^{-4}
2400	Ar	1.054	3.84[b]	19	4.28×10^{-4}
		1.054	3.83[c]	13	3.65×10^{-4}

[a] 4 hours at 2400°C before test in H_2 atmosphere.
[b] 1 hour at 2400°C before test in Ar atmosphere.
[c] 4 hours at 2400°C before test in Ar atmosphere.

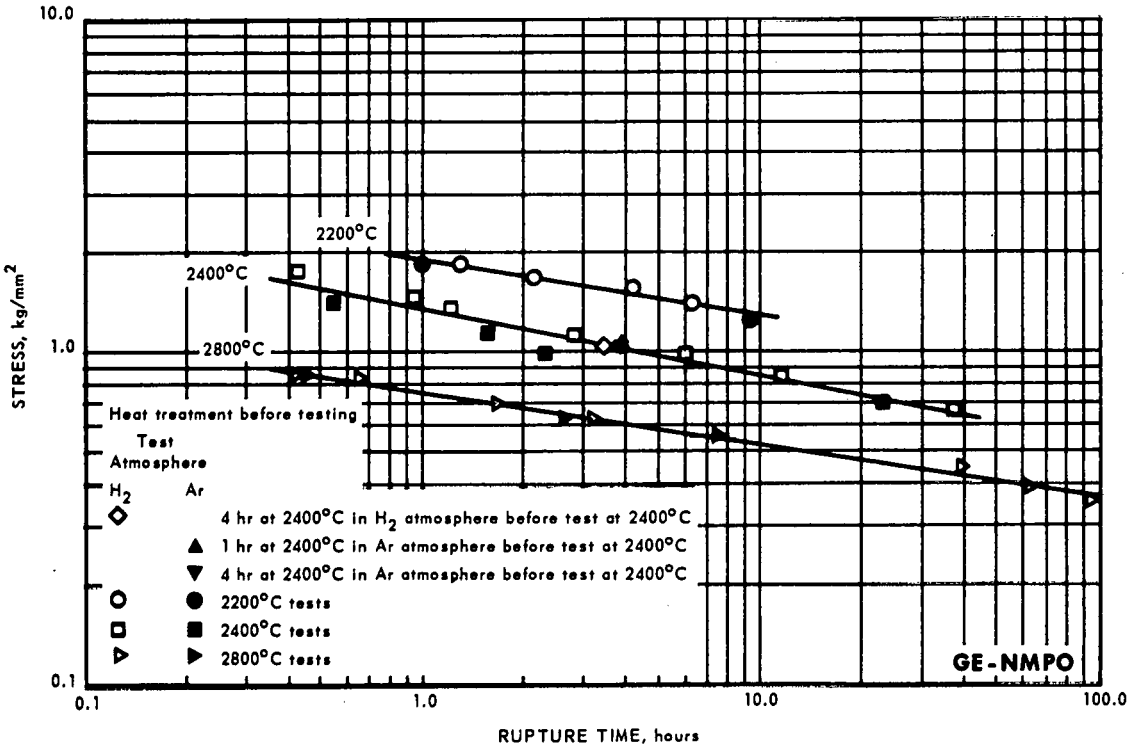

Fig. 2.9 – Stress-rupture data for sintered tungsten

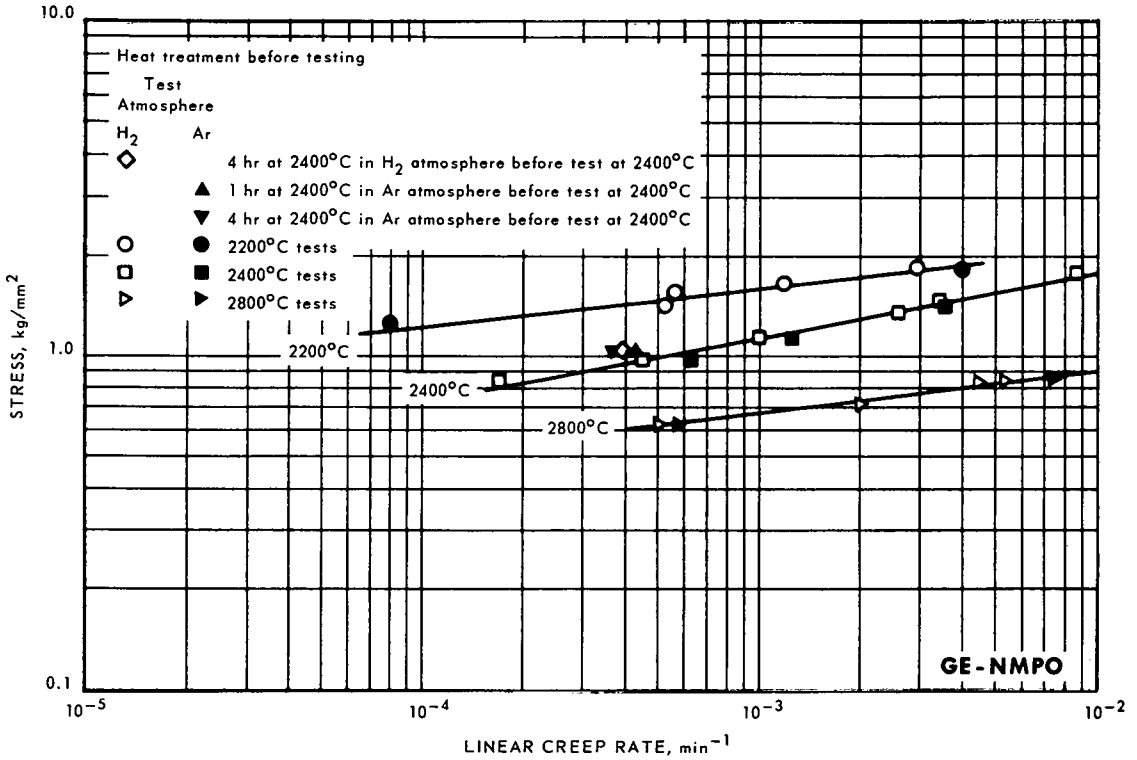

Fig. 2.10 – Stress versus creep rate for sintered tungsten

argon atmospheres at 2200°C and 2800°C, but not at 2400°C. These differences at 2400°C while small are definitely noticeable. Further, they decrease at longer test times (i. e., lower stresses) which seems consistent with sintering considerations since the longer exposures would allow additional sintering in argon and thereby cause the results to be identical in the two atmospheres.

Heat treating samples in both hydrogen and argon at 2400°C prior to creep-rupture testing at 2400°C provided rupture strengths that were the same. This is also shown in Figures 2. 9 and 2. 10.

Tungsten Contamination During Stress-Rupture Testing

During the stress-rupture testing of the various materials to 2800°C in both hydrogen and argon atmospheres, which has continued for over a year, some changes in the test operation and improvements in the equipment have been made. One change in the operation that appeared to reduce the contamination in test samples was to operate the tests with a static gas atmosphere rather than with flowing gas. This reduced the amount of impurities introduced to the system from the gas.

An additional improvement which was incorporated in the equipment was the substitution of a tungsten split-tube (0. 10-cm-thick) heating element for the initial heating element that consisted of 50 tungsten rods. This was done when it was demonstrated that with the split-tube element a considerably longer life could be obtained with little or no distortion of the heating element. The tungsten-rod element would become distorted after some use, especially at 2800°C, causing some question as to the uniformity of the temperature distribution along the specimen gage length.

During all periods of the testing program, representative samples were chemically analyzed after test for impurities and/or contamination. After testing a molybdenum

sample for 1000 hours at 2200°C in a static hydrogen atmosphere, it was determined that the sample had absorbed 10 weight percent tungsten during the testing. This contamination was the result of tungsten transport from the heating element which deposited on the sample.

As a result of this, additional tests were performed with a molybdenum protective foil around the molybdenum sample to reduce the amount of tungsten contamination. These results along with others are presented in Figure 2. 11. Based on these data, there appears to be a considerable reduction in the amount of tungsten absorbed by the samples when tested in a static atmosphere protected by the foil. Tests to date have not been performed with the tungsten split-tube heating element in flowing gas but these are being initiated.

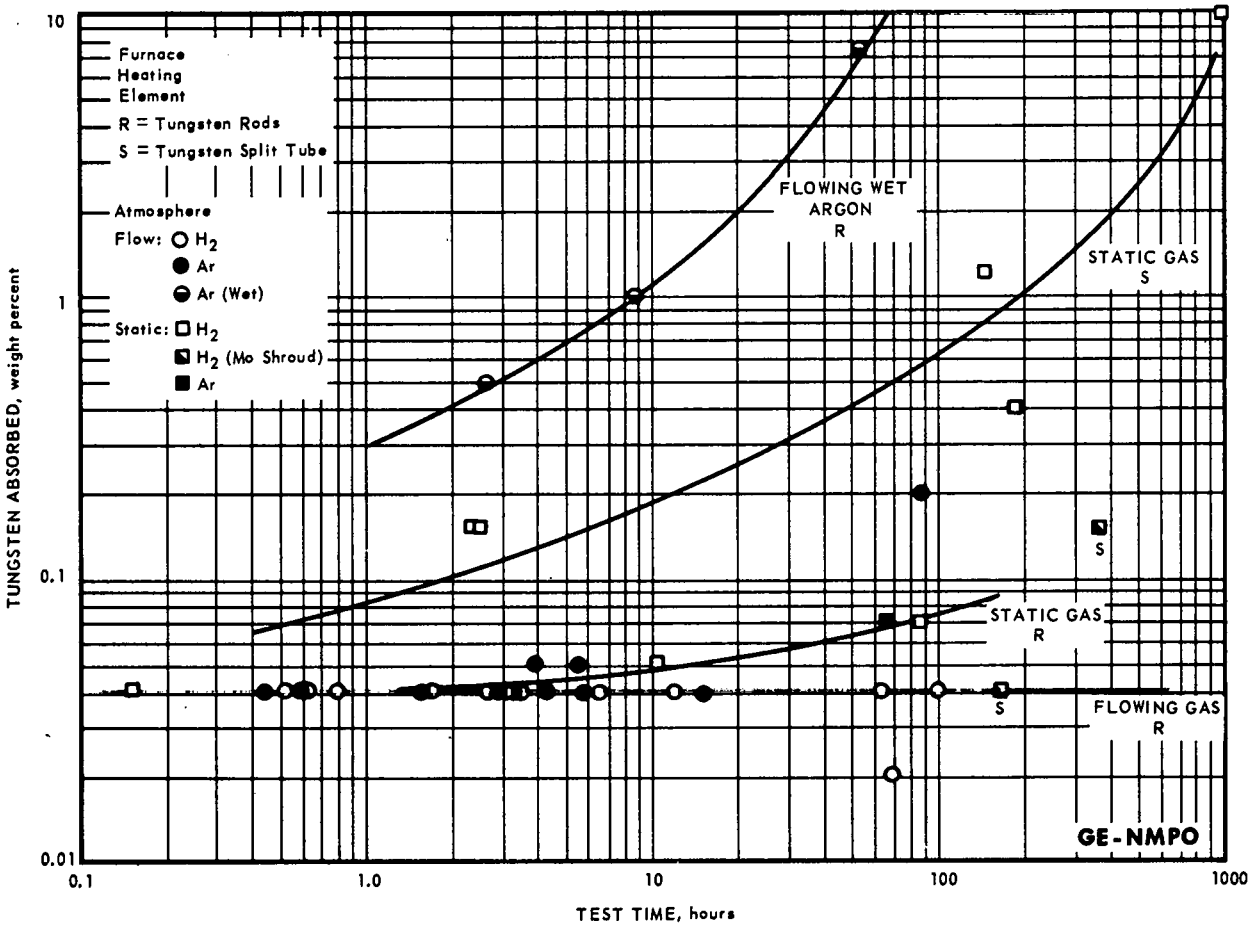

Fig. 2.11 – Tungsten contamination versus test time at 2200°C for various atmospheres and test configurations

The long-term (10 to 1000 hours) stress-rupture results for arc-cast molybdenum at 2200°C for static and flowing atmospheres are shown in Figure 2. 12. The lower curve represents the data for Mo-C obtained with a flowing gas using a tungsten-rod heating element. The middle curve represents data for Mo-C obtained with a static atmosphere using a tungsten split-tube heating element. The upper curve represents data for Mo-B' (different source of material) obtained with a static atmosphere using a tungsten split-tube heating element. The 33. 5-, 165-, and 368-hour tests of Mo-B' were performed with the molybdenum protective foil.

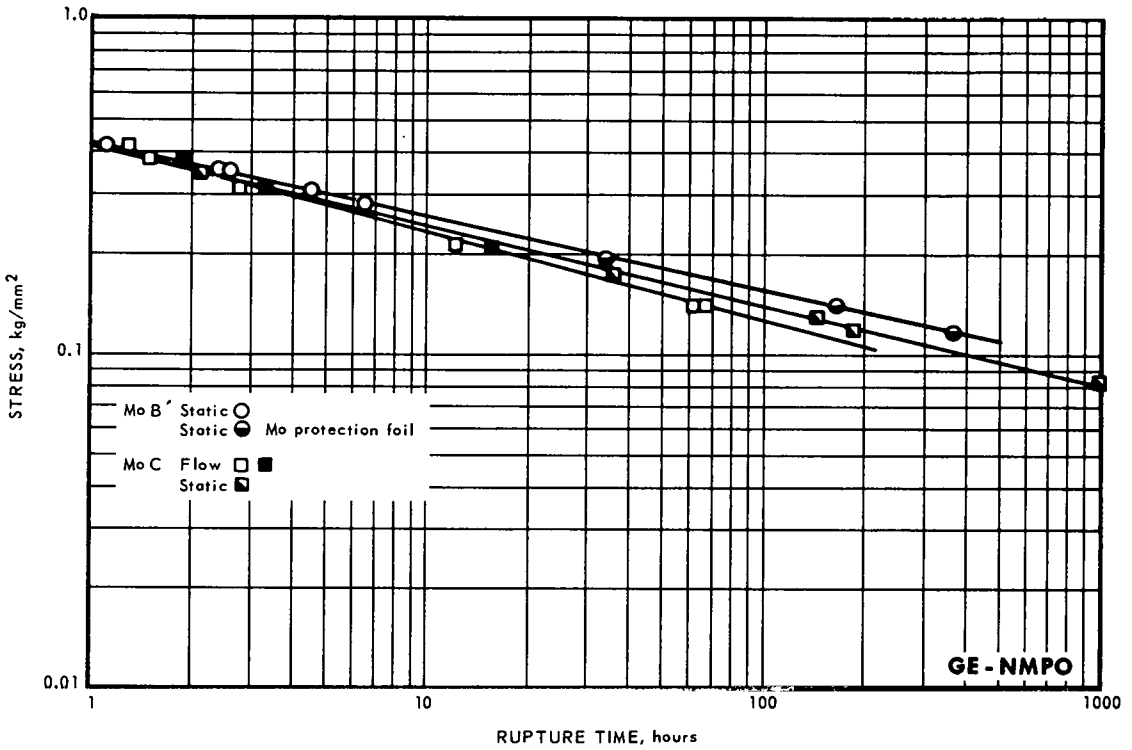

Fig. 2.12 – Stress-rupture data for arc-cast molybdenum at 2200°C in H_2 atmosphere

From Figure 2. 12, it appears that the short-term (1 to 10 hours) rupture strengths of the two sources of material are similar, but they deviate as the stress is reduced (or rupture time is increased at 2200°C). The effect of the tungsten contamination is also evident in comparing the two lower curves. The lower curve more nearly shows the true rupture strength of the material; the curve above it reflects the result of higher amounts of tungsten contamination.

As a result of this study, tests are being performed with a flowing gas atmosphere, and a purifier is being used to remove contaminants from the gas prior to being introduced to the furnace.

Correlation of Stress Rupture and Creep

It has been shown by Monkman and Grant* that an empirical relationship exists between rupture life and minimum creep rate independent of stress and temperature for aluminum, ferritic steels, austenitic stainless steels, etc. Using the stress-rupture and creep data for these lower melting point metals and alloys and testing between 400°C and 1000°C, the relationship gave a straight line on a log-log plot of the variables mentioned above, and in most cases the slope of these curves approached unity.

Using this method of correlation, similar curves were plotted for the refractory metals and alloys investigated in this program to 2800°C. Figure 2. 13 shows this relationship with all the materials having approximately the same slope with the exceptions of rhenium and W - 25Re.

*Monkman and Grant, "An Empirical Relationship Between Rupture Life and Minimum Creep Rate in Creep Rupture Tests," *American Society for Testing Materials*, Vol. 56, 1956, p. 593.

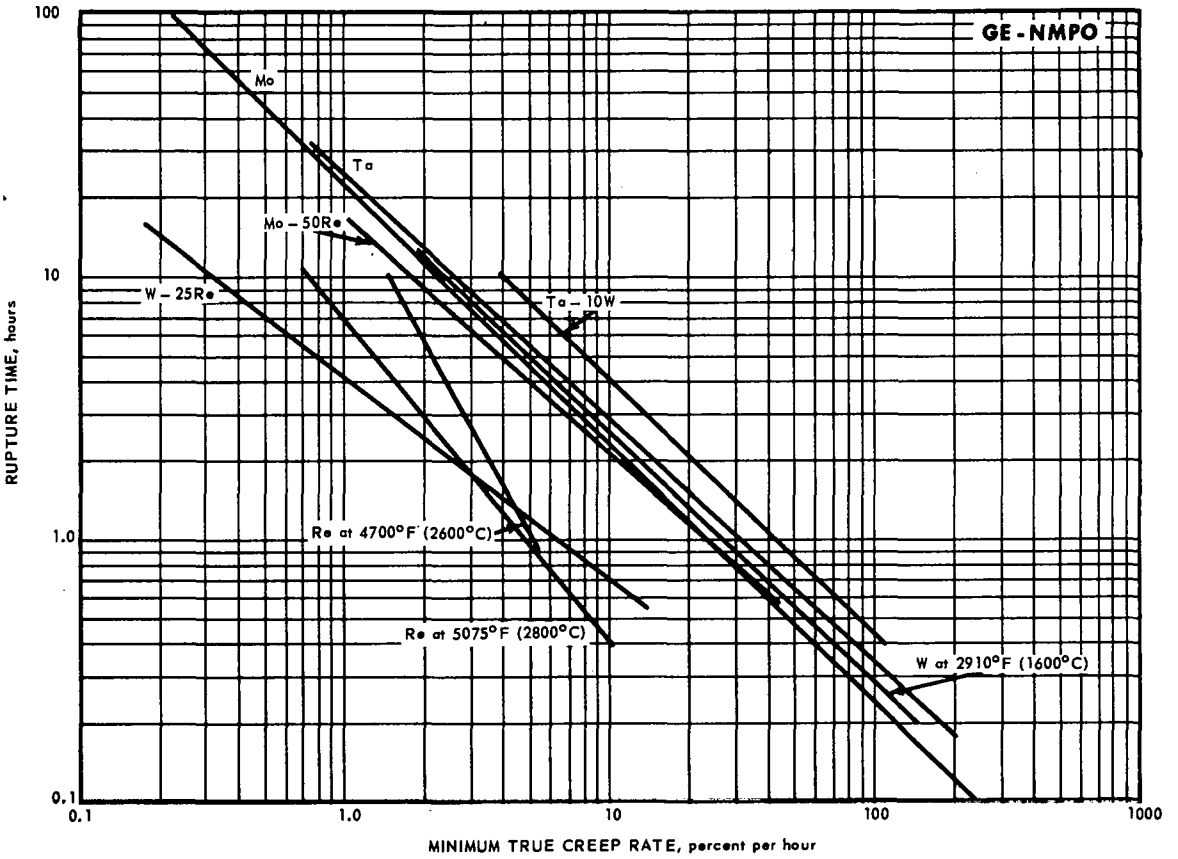

Fig. 2.13 – Rupture time versus minimum true creep rate of several refractory metals

Figure 2. 13 suggests that the general equation for the curves is:

$$\log t_R + m \log (mcr) = \log c$$

where:

t_R = rupture time, hours
mcr = minimum true creep rate, percent per hour
m = slope
c = intercept

Table 2. 5 lists the materials presented in Figure 2. 13 along with the slopes and intercepts. As mentioned above, it is seen that most of the slopes approximate unity. For unit slope, a more simplified equation is obtained:

$$\log t_R + \log (mcr) = \log c$$

eliminating logs:

$$t_R = \frac{c}{mcr}$$

This equation shows that the minimum creep rate is inversely proportional to the time of rupture. If the minimum creep rate is obtained in a relatively short time, the time to rupture may be predicted reasonably well. This may reduce the number of long-term tests required to obtain the stress-rupture strength of materials.

TABLE 2. 5

SLOPE, m, AND INTERCEPT, c, VALUES FOR EQUATION
$\log t_R + m \log (mcr) = \log c$
FOR SEVERAL METALS AND ALLOYS

Material	Test Temperature, °F	Slope, m	Intercept, c	Data Source
Molybdenum	1200 - 2400	0. 99	1. 35	GE-NMPO
Tantalum	2400 - 2600	0. 94	1. 39	GE-NMPO
Tungsten	1600	0. 96	1. 36	GE-NMPO
Aluminum	260 - 595	0. 85	1. 30	Monkman & Grant
Rhenium	2600	1. 86	1. 32	GE-NMPO
Rhenium	2800	1. 22	0. 83	GE-NMPO
Titanium	370 - 1090	0. 87	1. 00	Monkman & Grant
Ta - 10W	2400 - 2800	0. 98	1. 59	GE-NMPO
Mo - 50Re	2200	0. 90	1. 23	GE-NMPO
W - 25Re	2600	0. 78	0. 62	GE-NMPO
Monel	370 - 930	0. 92	0. 80	Monkman & Grant
Ferritic steels	425 - 705	0. 85	0. 56	Monkman & Grant
Austenitic stainless steel	540 - 815	0. 93	0. 89	Monkman & Grant
M 252	815	0. 89	0. 70	Monkman & Grant
Nimonic 80 and 90	705 - 815	0. 77	0. 48	Monkman & Grant
Inco 700	650 - 980	0. 80	0. 56	Monkman & Grant
S-816	650 - 1040	0. 88	0. 96	Monkman & Grant
S-590	650 - 1040	0. 88	0. 96	Monkman & Grant

W-Re ALLOY DEVELOPMENT

The primary objective of this effort is to obtain reliable materials for service at temperatures to 3000°C. Because portions of structures operating to 3000°C will be subject to lower temperatures, it is important that W - 25Re (at. %) alloys do not develop embrittling metallurgical reactions at low and intermediate temperatures. To explore the effects of prolonged low-temperature exposure, 0. 050-centimeter-thick bend specimens of alloys covering the W-Mo-Re compositions of most interest were held at the following temperatures for the periods indicated:

Holding Temperature, °C	Holding Period, hr	Exposure Atmosphere
1000	18	Hydrogen
1200	72	Hydrogen
1430	18	Vacuum
1800	67	Argon

Room-temperature bend-test results following the above treatments were similar in every instance. Bend-test results for the 67-hour, 1800°C treatment are shown graphically on the composition diagram in Figure 2. 14. These data indicate that the 25 or 30 atomic percent Re alloys retained their room-temperature ductility after the 67-hour treatment. Metallographic examination of the bend-test specimens showed the 25Re alloys to be free of sigma phase with sigma phase present at the 30 and 37Re levels as shown in Figure 2. 15. Similar specimens were treated 67 hours at 2200°C but were contaminated by a defective furnace atmosphere. However, structures observed in these specimens indicated that the 30Re alloys did not contain sigma phase while the 37Re alloys had high sigma phase content.

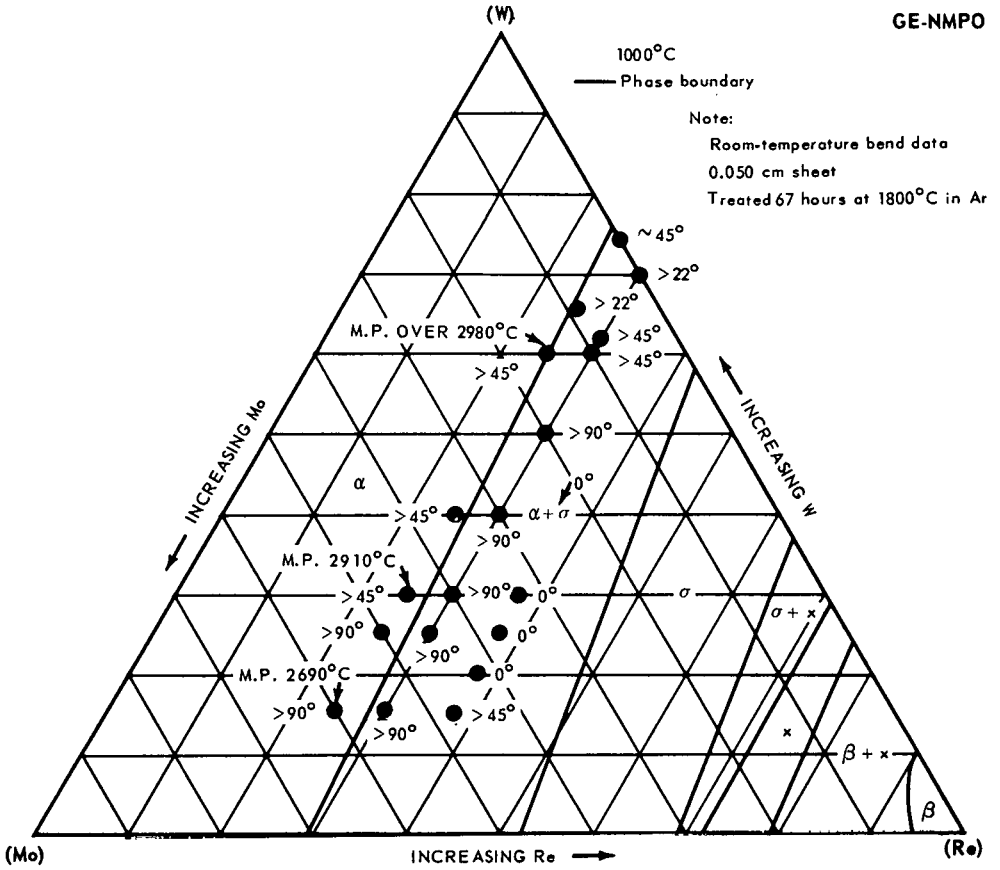

Fig. 2.14 – Bend test results of W-Mo-Re alloys

Melting points were determined for several W-Mo-Re alloys at the 25 atomic percent Re level and are indicated in Figure 2. 14. The melting point with only 30 atomic percent W present is 2910°C. The low tungsten content alloys appear to be important because of ease of fabricability which is comparable to commercial 50Mo - 50Re (wt %) alloy. The lower rhenium content of the tungsten-base alloys and much higher melting point are additional advantages in this system.

Agglomeration of Tungsten in Powder Metal Blending of W - 25Re

Electropolished and rolled W - 25Re sheet, processed from sintered metal powders, exhibited surface defects as shown in Figure 2. 16. An electron-beam microprobe analysis established the surface "spot" to be over 94 atomic percent pure tungsten. Sectioning of presintered blended W-Re powder compacts showed large agglomerated tungsten powder masses as shown in Figure 2. 16b. Generally, the tungsten agglomerates appeared to have high density throughout as shown in Figure 2. 16c. However in some cases, a soft core within a harder shell was also observed with only the shell remaining after polishing as shown in Figure 2. 16d. As normally viewed with the microscope, the protruding surface spots were not distinguishable from the overall sheet structure as illustrated by Figure 2. 16e, but a selective anodic-oxidation* treatment clearly showed unalloyed tungsten-rich areas within the W - 25Re sheet as shown in Figure 2. 16f.

*U. Wolff, "Anodic Oxidation to Prevent Inhomogeneity in Refractory Alloys," *Transaction of American Society of Metals*, Vol. 55, 1962, pp. 363–365.

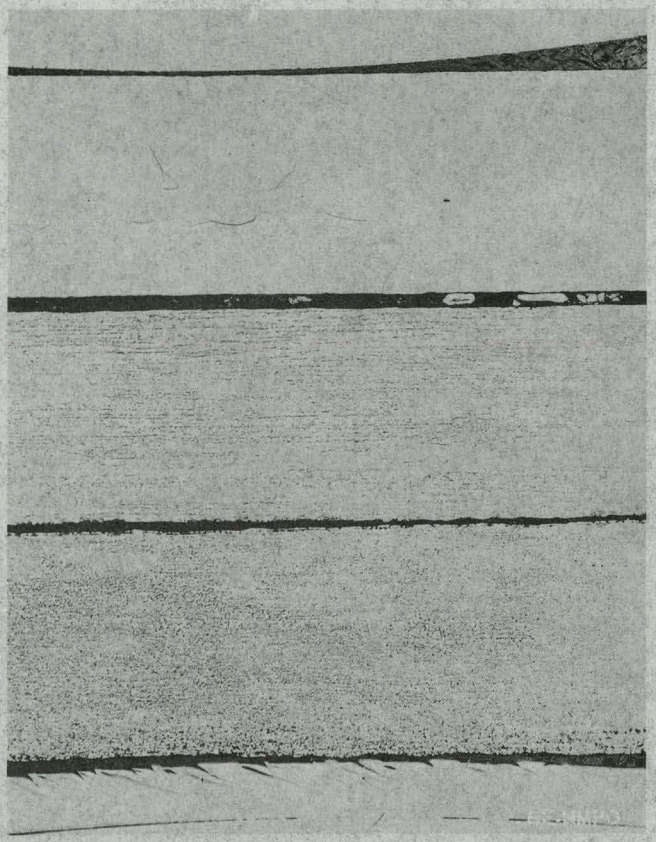

Fig. 2.15 – Photomicrograph of W-Mo-Re alloys after holding at 1800°C for 67 hours in argon atmosphere

An investigation was made to determine the agglomerating characteristics of 0. 88, 1. 44, and 2. 0+ average micron grain size tungsten powders. The 2. 0+ micron powder did not agglomerate, but the finer powders did. Screening of the 0. 88- and 1. 44-micron tungsten powders showed that the +400/-325 mesh particles pelletized to firm masses. Removal of the undesired size fraction and wet-blending in acetone, methanol, or carbon tetrachloride eliminated agglomeration in the W-Re powder blends.

Prior to application of a new lot of tungsten powder to W-Re alloy fabrication, a review of agglomerating characteristics as a dry-blended and presintered compact should be completed. This procedure has been included in the revised processing specification now followed in this program.

The sintering of blended powder compacts has been essentially standardized at 3000°C but a tendency to liquefy a portion of the compact in heating has been encountered. The liquid metal can form at the 2810°C W-Re eutectic temperature. This has been corrected by holding for 1 hour at about 2750°C to avoid the eutectic composition through Re diffusion. A void surrounded by W-Re eutectic formed on heating a powder compact to 3000°C is shown in Figure 2. 17. Compositions, determined by electron-beam microprobe analysis, of the various constituents are also shown in Figure 2. 17. The needle-like lamellae consist of the sigma-phase composition (42 at. % Re) with 35 atomic percent Re present between the needles. The constituent diffusing away from the original Re particle moving along the grain boundaries is also the sigma-phase composition (42 at. % Re).

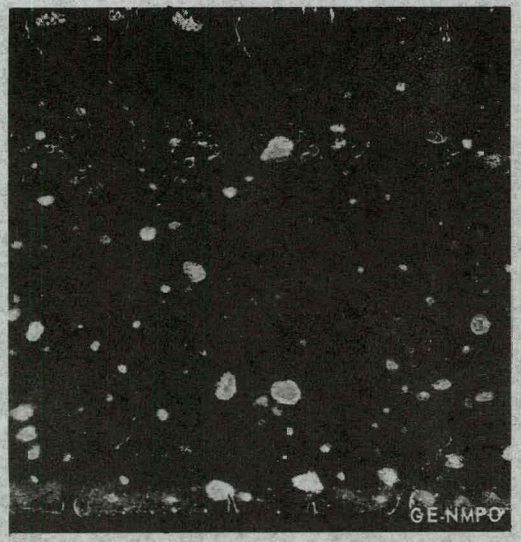

1 X

(a) Tungsten-rich areas on electro-polished sheet

10 X

(b) Agglomerated W in presintered W – 25Re powder compact

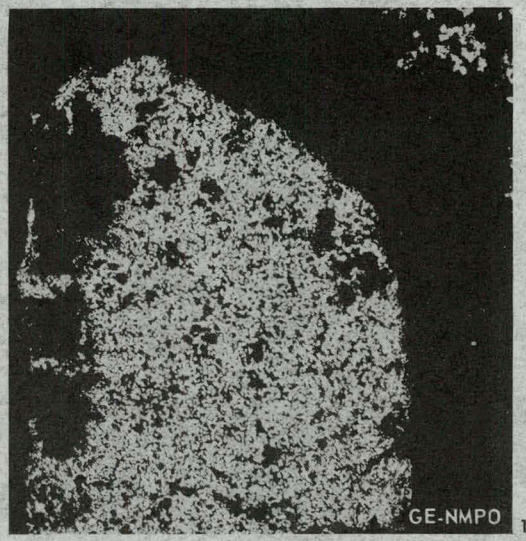

100 X

(c) Structure of W agglomerate – 1200°C presinter

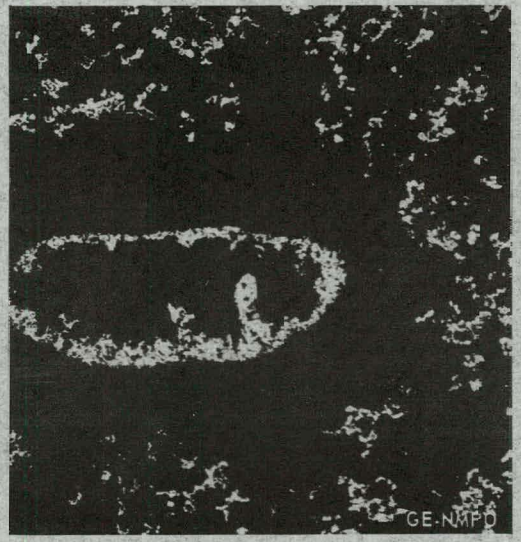

100 X

(d) Hard shell noted on some W agglomerates

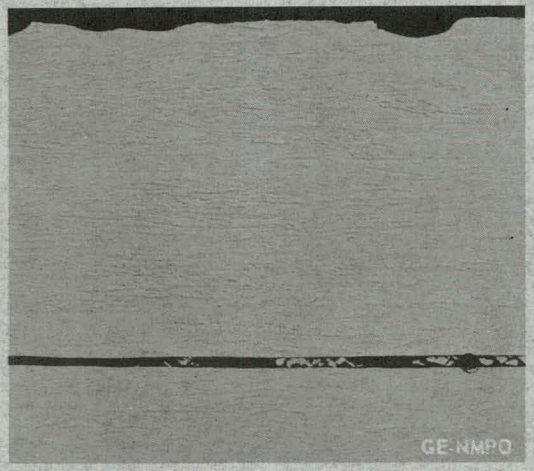

100 X

(e) W – 25Re sheet as-polished. No sigma phase present

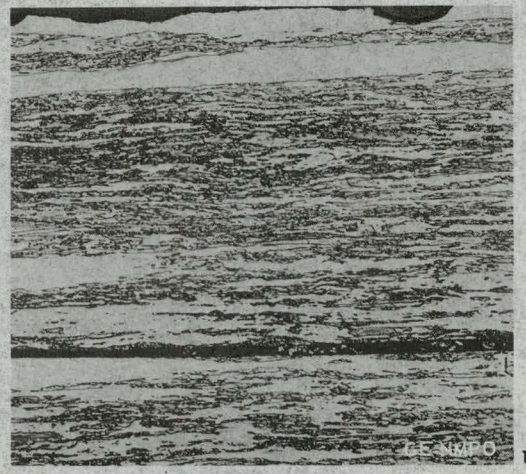

100 X

(f) Area as in (e). Anodic oxidation to show W-rich areas

Fig. 2.16 – Photomicrographs showing defects caused by tungsten powder agglomeration and segregation in W – 25Re processing

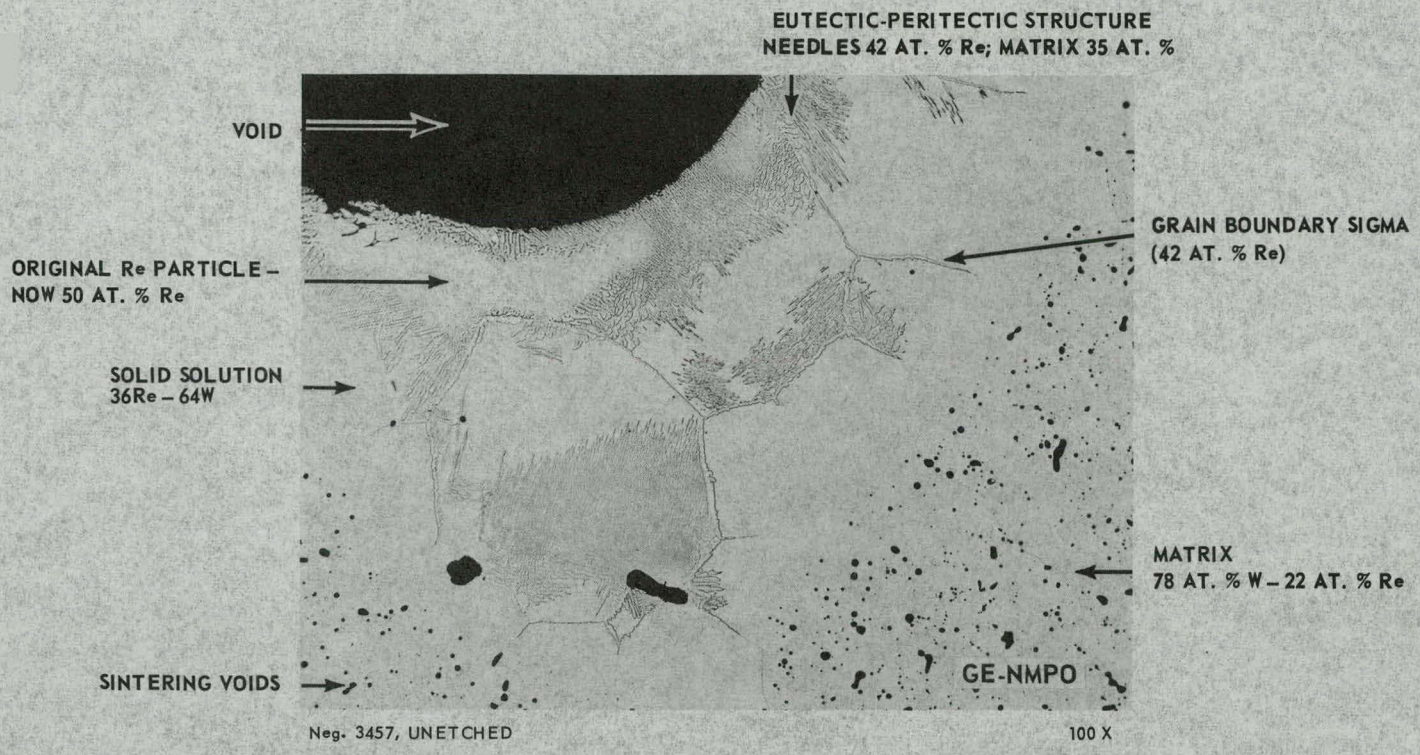

Fig. 2.17 – Photomicrograph showing eutectic-type structure surrounding a void developed during sintering of a W – 25Re powder-metal compact at 3000°C

Throughout this program, lamination within rolled sheet has been observed due to improper hot-rolling procedures or to improper die operations in powder compacting before sintering. Investigations have shown that a 2 percent reduction per pass in hot-rolling, with 5 minutes reheat between passes, avoids centerline defects in hot-rolling. Double pressing (reversing the die and repressing) in powder compacting avoids powder compact lamination. Two series of blended powders were processed to evaluate the influence of the quantity of powder or load per compact pressing and also the influence of different pressing loads on sintered billet density. Heavy pressing loads to 14 kg/mm^2 on the powder gave highest sintered densities, but the blended powder load (100 to 400 grams) quantity did not influence results.

Stress-relief treatments of 1 to 3 hours at 1200°C have not yielded optimum ductility in cold-rolled W - 25Re sheet. Vacuum sintering at 1300°C is currently being studied. Frequent stress relieving during cold-forming operations has been adopted because of the high rates of work hardening observed.

Defects in Commercially Produced W - 25Re Sheet and Tube

A recent shipment of commercially produced W - 25Re sheet obtained during this work period had a very high W-Re sigma-phase content as shown in Figure 2. 18. Sigma free structures produced in this program, and shown in Figure 2. 19, represent the quality sheet required to meet the 3000°C service requirements of this material. In heating to 3000°C, the commercial sheet developed large blisters or voids shown in Figure 2. 20. Similarly, W - 25Re tubing recently received from a commercial source was found irregular in wall thickness.

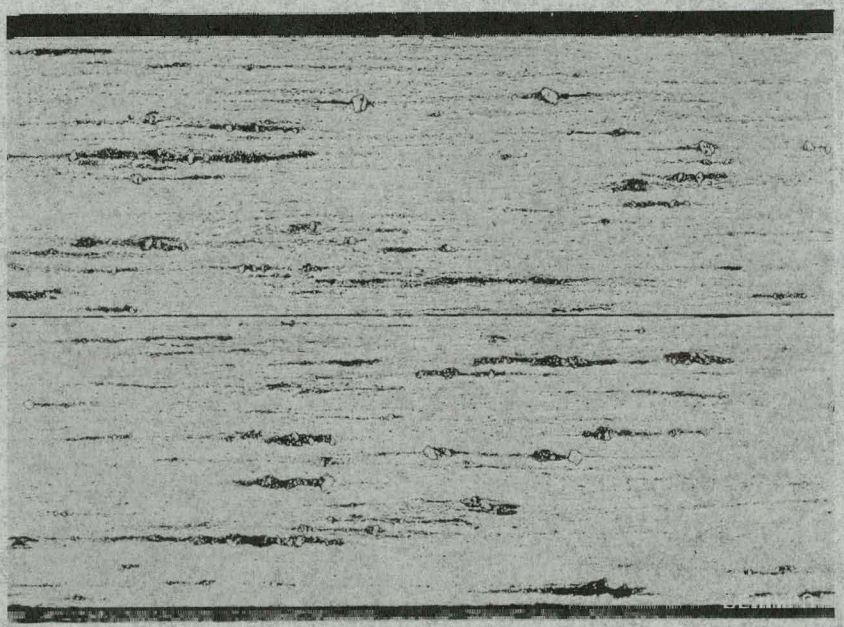

Neg. 3366, UNETCHED 100 X

Fig. 2.18 – Photomicrograph of a cross section through two samples of W – 25Re sheet received from a commercial vendor

Fabricated by Rolling Arc-Melted Button Ingots

Processed from Powders Using a 3000°C Sintering Treatment to Eliminate the W-Re sigma phase

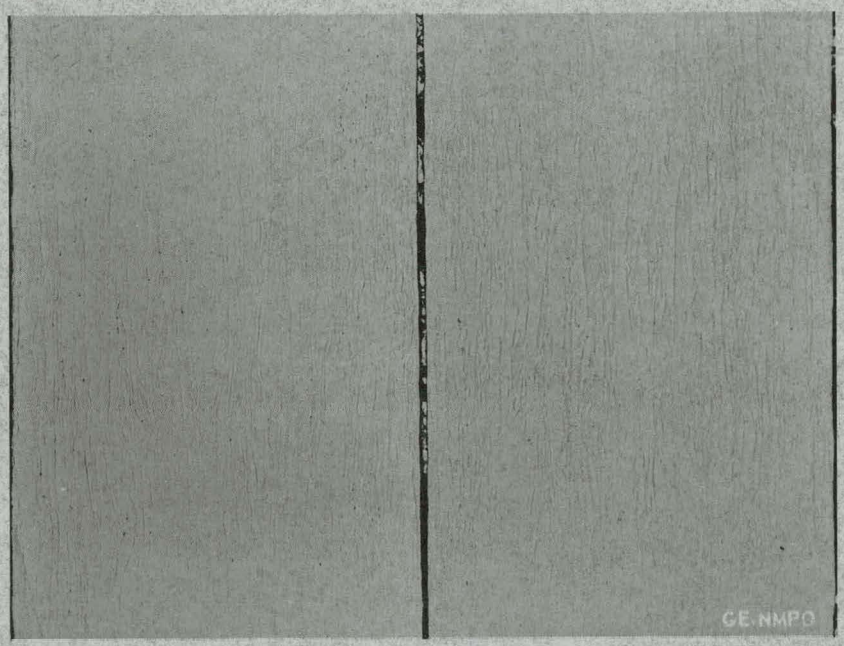

Neg. 3436, UNETCHED 100 X

Fig. 2.19 – Photomicrograph of cross sections of W – 25Re sheet of acceptable internal quality produced in the GE-NMPO laboratory

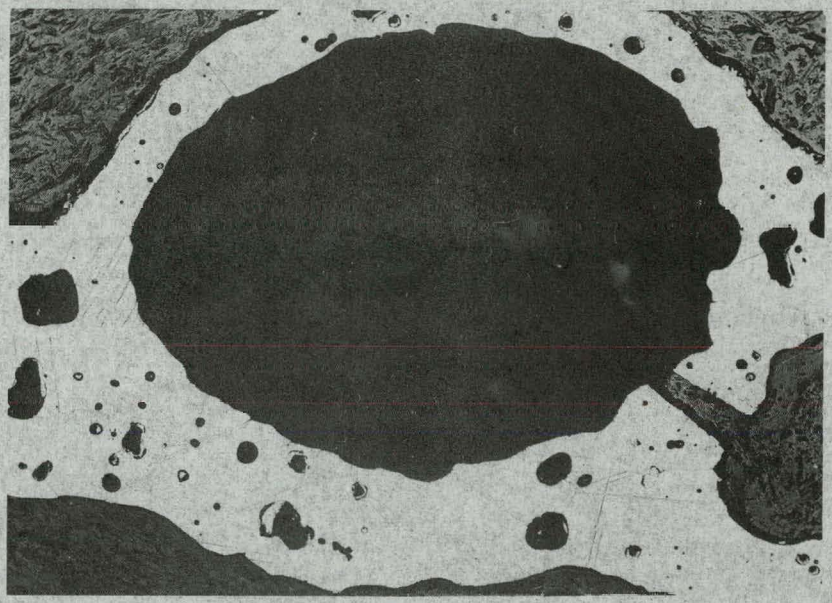

Neg. 3365, UNETCHED 75 X

Fig. 2.20 – Voids formed by gaseous constituents in commercially produced W – 25Re sheet in heating at 3000°C

WORK PLANNED FOR NEXT PERIOD

The effect of lower test temperature (2000° or 2200°C) on rupture strength of W - 25Re and tungsten as well as longer test times in both hydrogen and argon atmospheres will be determined.

Short-term (1 to 10 hour) stress-rupture and creep tests of rhenium at temperatures from 2000° to 2800°C will be initiated.

Sufficient W - 25Re sheet will be produced to qualify all portions of the present processing procedures for producing reliable material, and to satisfy test program requirements.

An electron-beam melted W - 30Re ingot which has been received and a similar cast ingot which has not yet been received will be extruded to tubing. Sintered powder billets are also being prepared for extrusion. Additional ingots will be ordered when the feasibility of the procedures has been proven.

3. EFFECT OF RADIATION ON HIGH-TEMPERATURE ALLOYS

(57004)

The objective of this program is to determine the effect of radiation on the time-, temperature-, and stress-dependent properties of selected high-temperature alloys and refractory metals, to identify the causes of any observed changes in these properties, and to develop remedial measures.

REFRACTORY METALS PROGRAM

Status of Irradiations

The data for the refractory-metal specimen irradiations are given in Table 3.1. The fabrication of cartridge MT-113 was completed and shipped to ITS for insertion in the ETR in the October cycle. This cartridge is the first elevated-temperature cartridge in the current program. It contains 5 molybdenum, 5 Mo-TZM, 10 W - 25Re, and 20 tungsten resistivity and hardness specimens. A schematic drawing of the four tubes showing the thermocouple, dosimeter, and specimen locations is given in Figure 3.1. Figure 3.2 shows the construction features of one of the tubes. The final assembly of the four tubes into the cartridge is shown in Figure 3.3. The location of 8 of the 12 dosimeters may be noted in this photograph.

The design temperature for the tungsten and W - 25Re specimens is 1300°C; the design temperature for the Mo and Mo-TZM specimens is 700°C. A plot of the calculated temperature values at a power level of 175 megawatts versus the reactor core position is shown in Figure 3.4.

The temperature of the specimens will be controlled by the flow and ratio of the He-to-Ar gas mixture. Two refractory-metal test facilities were installed in the ETR and are now being used for irradiation of both the refractory-metal and the refractory-metal-clad fuel specimens. Figure 3.5 is a schematic of one of the two identical loop facilities. It is composed of a helium and argon gas supply station, individual gas filters, dryers, rotameters, and temperature recorders located in the experiment control room. A 0.32-centimeter gas supply line extends from the control room to an auxiliary panel located in the reactor area. Parallel drives and oxygen getters are located in this area in addition to the necessary valves and fittings for evacuation and purging the upstream portion of the system. The oxygen getter material is titanium metal which is operated at a peak temperature of 870°C.

A shielded panel is located in the same area which houses the gas exit lines, carbon traps, and ion chambers. The gas exits into the off-gas system located in the reactor trench.

Every precaution was taken to insure an ultraclean system. Each component, including the stainless steel tubing, was individually cleaned, purged with inert gas, and sealed prior to final assembly. After facility installation, the entire system was purged with gettered

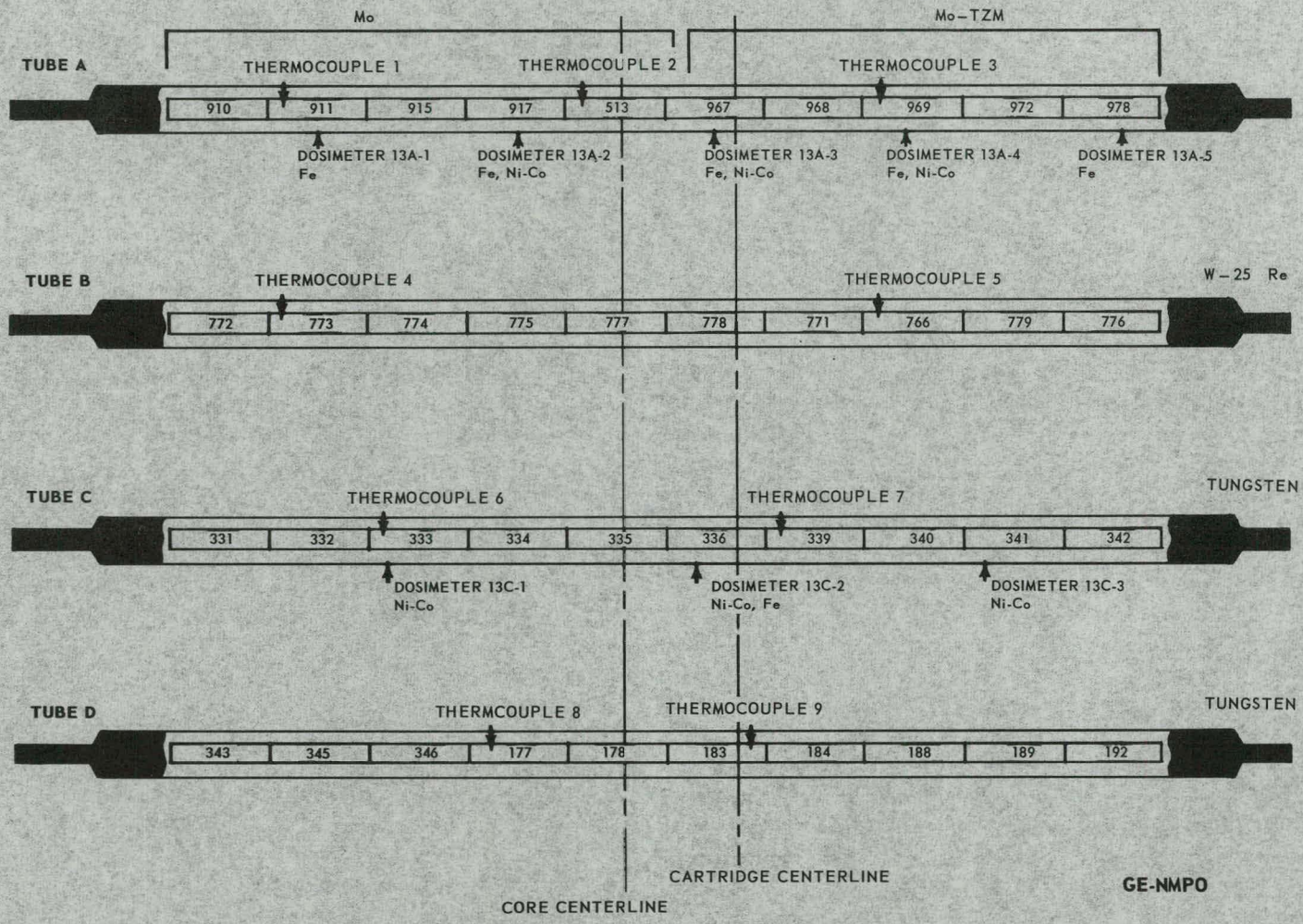

Fig. 3.1 – Specimen, thermocouple, and dosimeter locations of Capsule MT-113

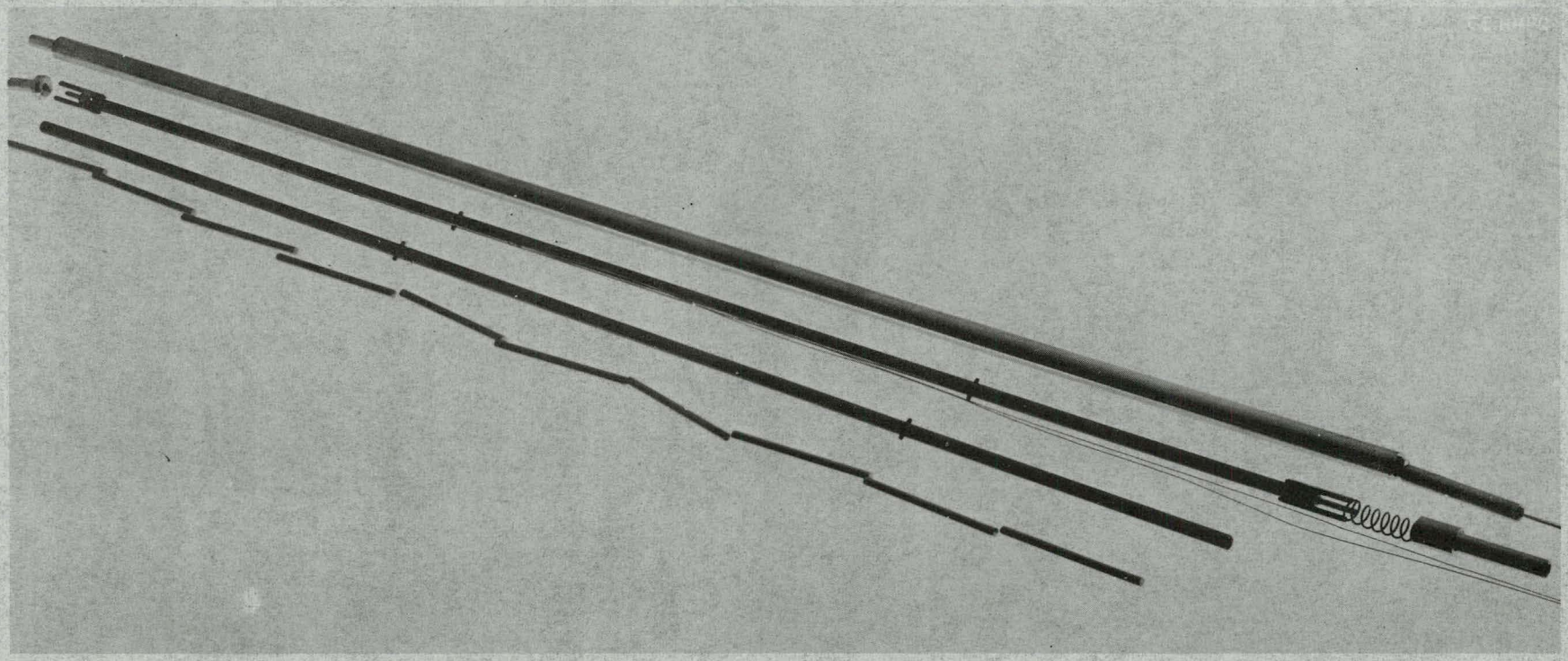

Fig. 3.2 – Construction of one of the tubes of Capsule 33MT-113 (Neg. 63-9-12A)

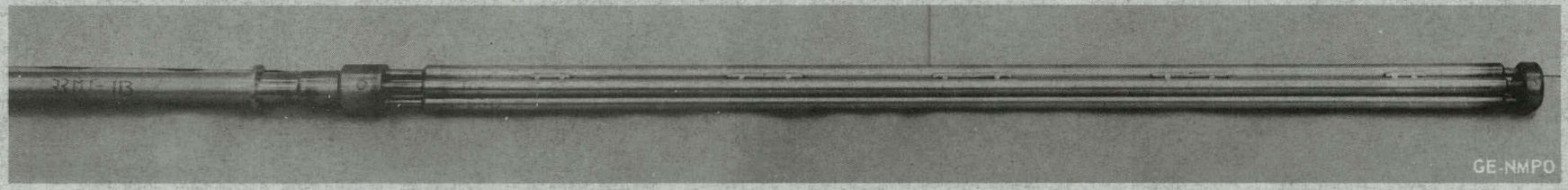

Fig. 3.3 – Tube assembly of high-temperature refractory-metal irradiation Capsule 33MT-113 (Neg. 63-9-12B)

TABLE 3.1

IRRADIATION DATA FOR REFRACTORY-METAL CAPSULES

	Specimen Data			Irradiation Data			
					Exposure,	Neutron Dose, nvt[b]	
Capsule	Material	Type[a]	Number	Facility	hours	Fast ($E_n \geq 1$ Mev)	Thermal
ORM-1	W	CR(F)	4	ORR F-9	1.0	5.3×10^{16}	3.8×10^{17}
ORM-2	W	CR(F)	4	ORR F-9	12.0	4.2×10^{17}	6.1×10^{18}
ORM-3	W	Wire	116	ORR F-9	12.0	6.9×10^{17}	4.9×10^{18}
ORM-4	W	CR(R)	4	ORR F-9	12.0	5.8×10^{17}	4.1×10^{18}
	W	T(R)	4	ORR F-9	12.0	6.8×10^{17}	5.1×10^{18}
ORM-5	W	CR(R)	7	ORR F-2	47.5	3.7×10^{18}[c]	2.0×10^{19}[c]
ORM-6	W	CR(R)	7	ORR F-2	47.5	3.7×10^{18}	2.0×10^{19}
ORM-7	W	H-R	10	ORR F-2	47.5	5.3×10^{18}	2.5×10^{19}
ORM-8	W	CR(R)	7	ORR F-2	240.0	2.5×10^{18}	9.5×10^{19}
ORM-9	W	T(R)	9	ORR F-2	47.5	5.1×10^{18}	2.8×10^{19}
ORM-10	W	T(R)	9	ORR F-2	240.0	1.7×10^{19}	9.3×10^{19}
ORM-11	W	H-R	10	ORR F-2	240.0	3.3×10^{19}	1.2×10^{20}
ORM-12	W	CR(F)	5	ORR F-2	240.0	3.2×10^{19}	1.5×10^{20}
ORM-13	Mo	CR(F)	7	ORR F-9	133.0	6.9×10^{18}	5.5×10^{19}
	Mo-TZM	CR(F)	7				
	Re	CR(F)	7				
	W - 25Re	CR(F)	7				
ORM-14	W	H-R	10	ORR F-9	249.0	1.3×10^{19}[c]	1.0×10^{20}[c]
	W - 25Re	H-R	10				
ORM-15	W	H-R	5	ORR F-9	249.0	1.3×10^{19}[c]	1.0×10^{20}[c]
	Mo	H-R	15				
MT-103	W	Wire	62	ETR L-6	-	2.1×10^{20}	7.9×10^{19}
MT-112	Mo	CR(F)	8	ETR I-13	-	-	-
	Mo-TZM	CR(F)	7				
	W - 25Re	CR(F)	7				
	Mo	H-R	4				
	W	H-R	7				
	W - 25Re	H-R	4				
MT-113	Mo	H-R	5	ETR	-	-	-
	Mo-TZM	H-R	5				
	W - 25Re	H-R	10				
	W	H-R	20				

[a]Coded as follows: CR = creep-rupture specimen; (R) = round type; (F) = flat type
H-R = hardness and resistivity
T = tensile specimen

[b]Based on $Ni^{58}(n, p)\ Co^{58}$ and $Co^{59}(n, \gamma)\ Co^{60}$ reactions.

[c] Estimated dosage.

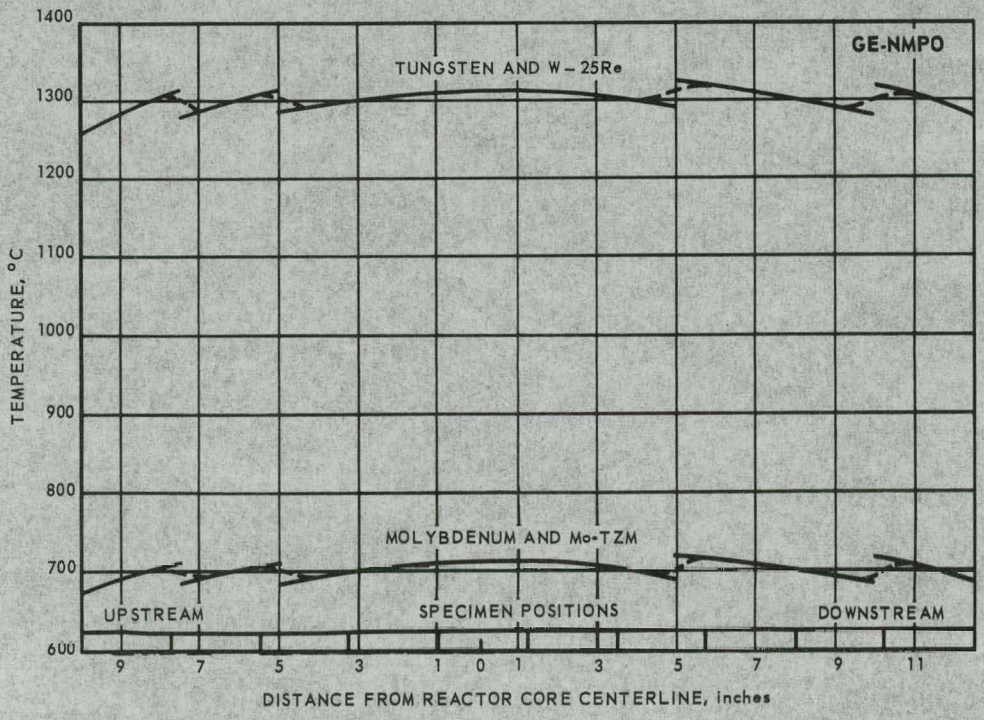

Fig. 3.4 – Calculated temperatures versus core position of Capsule 33MT-113

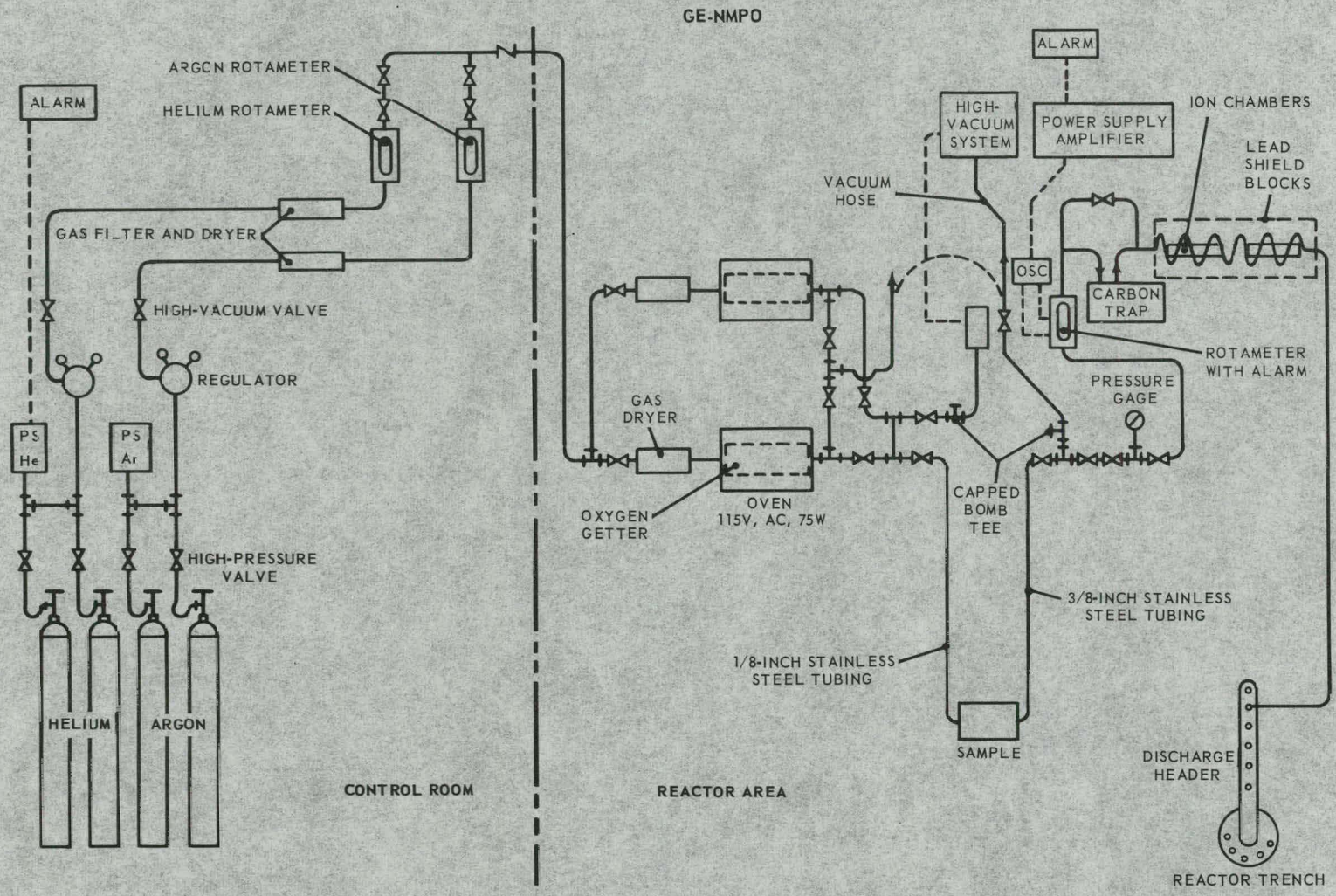

Fig. 3.5 – Schematic of refractory-metal test facility

helium and evacuated several times, a procedure which is followed each time a lead tube assembly is installed.

The reactor ambient-temperature capsule MT-112 was removed from the ETR in September and shipped to Evendale in October. This test assembly, consisting of three capsules,* was irradiated for approximately 3800 megawatt days in moderator water of the I-13 hole. Upon withdrawal from the reactor, two of the resistivity specimens were discovered to be broken. Examination of the specimens after removal from the capsules revealed extensive damage to the specimens which appeared to be caused by corrosion or possibly erosion. The exact identity of the specimens has not been determined to date, but it appears that the Mo and Mo-TZM specimens suffered the major damage with some damage also to the W - 25Re sheet specimens. Investigations are underway to evaluate the nature of the apparent corrosion of these specimens.

Creep-Rupture Tests

A summary of creep-rupture tests on sheet-type tungsten specimens is shown in Table 3.2. A number of electropolished tungsten-rod specimens were creep-rupture tested at 1100°C. Tests conducted during the current reporting period included control and irradiated specimens from capsules ORM-12 and ORM-13.

TABLE 3.2

SUMMARY OF CREEP-RUPTURE TESTS ON TUNGSTEN[a] AT 1100°C

Specimen No.	Condition	Stress, kg/mm^2	Rupture Life, hr	Linear Creep Rate, sec^{-1}
201	Control	34.45	4.93	1.85×10^{-6}
206	ORM-12[b]	34.45	8.89	1.4×10^{-6}
212	Control	35.86	3.59	2.78×10^{-6}
213	Control	35.86	3.26	2.55×10^{-6}
203	ORM-12	35.86	7.00	1.65×10^{-6}
202	Control	37.26	2.64	4.00×10^{-6}
207	ORM-12	37.26	4.20	2.80×10^{-6}
204	ORM-12[c]	37.26	4.01	2.43×10^{-6}
214	Control[d]	17.58	8.69	7.40×10^{-6}
215	Control[d]	18.63	2.68	1.53×10^{-5}
205	ORM-12[d]	18.63	4.08	1.41×10^{-5}

[a]Cold-worked 0.5 mm sheet; tested in cold-worked condition unless otherwise denoted. All tests were conducted in a hydrogen atmosphere.
[b]ORM-12 Capsule irradiated at reactor ambient temperatures in ORR F-2 facility to 3.2×10^{19} nvt, ($E_n \geq 1$ Mev).
[c]Irradiated (ORM-12) plus annealed in hydrogen for 3 hours at 1100°C.
[d]Specimens annealed as a group at 1900°C for 1 hour in hydrogen prior to testing.

Tungsten - Figure 3.6 presents a plot of 1100°C tests on cold-worked tungsten-sheet material. The irradiation to a fast neutron dose of 3.2×10^{19} nvt increases the rupture life by a factor of about 1.6 when compared to corresponding control data. As expected, this radiation-induced hardening was not as significant as in the case of recrystallized tungsten where a factor of 2.6 increase in rupture life was observed at the same temperature for a fast neutron dose of 2.5×10^{19} nvt.†

The creep rates of the tungsten specimens are shown in Figure 3.7. This plot and the values shown in Table 3.2 indicate that all of the irradiated specimens possessed lower

*"High-Temperature Materials Program Progress Report No. 27, Part A," GE-NMPO, GEMP-27A, September 30, 1963, Figure 3.1, p. 27.

†Ibid., Figure 3.7, p. 33.

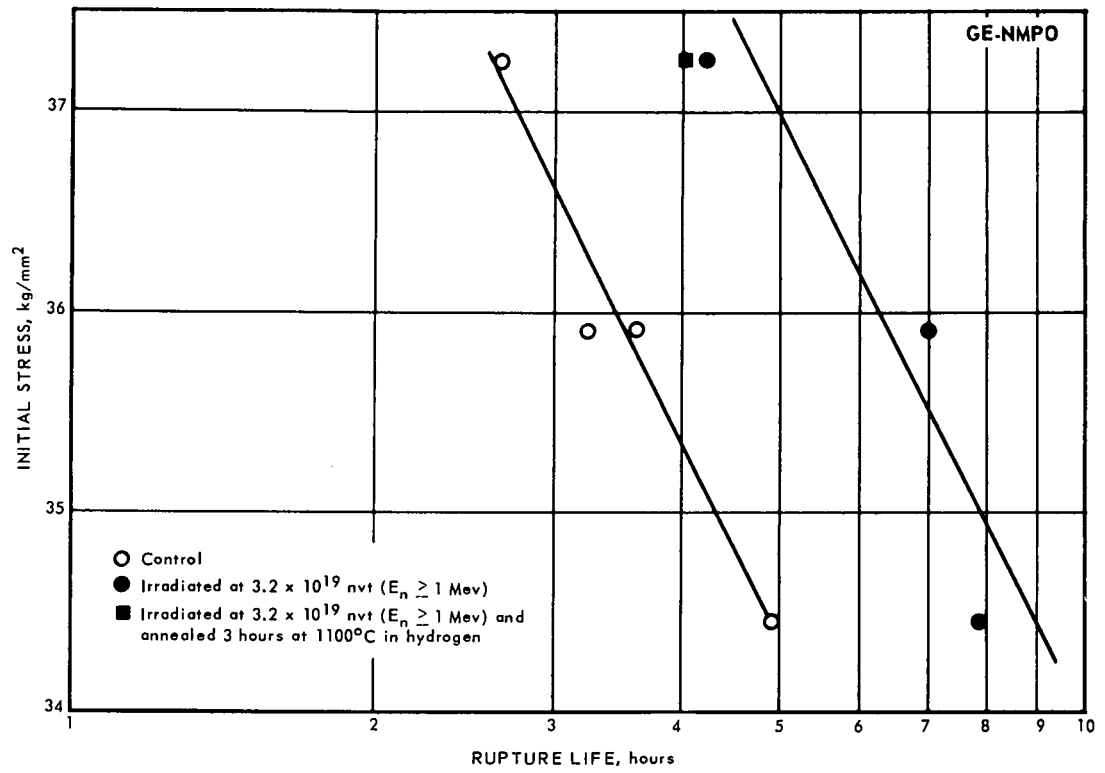

Fig. 3.6 – Stress-rupture strength of tungsten sheet specimens tested at 1100°C in hydrogen

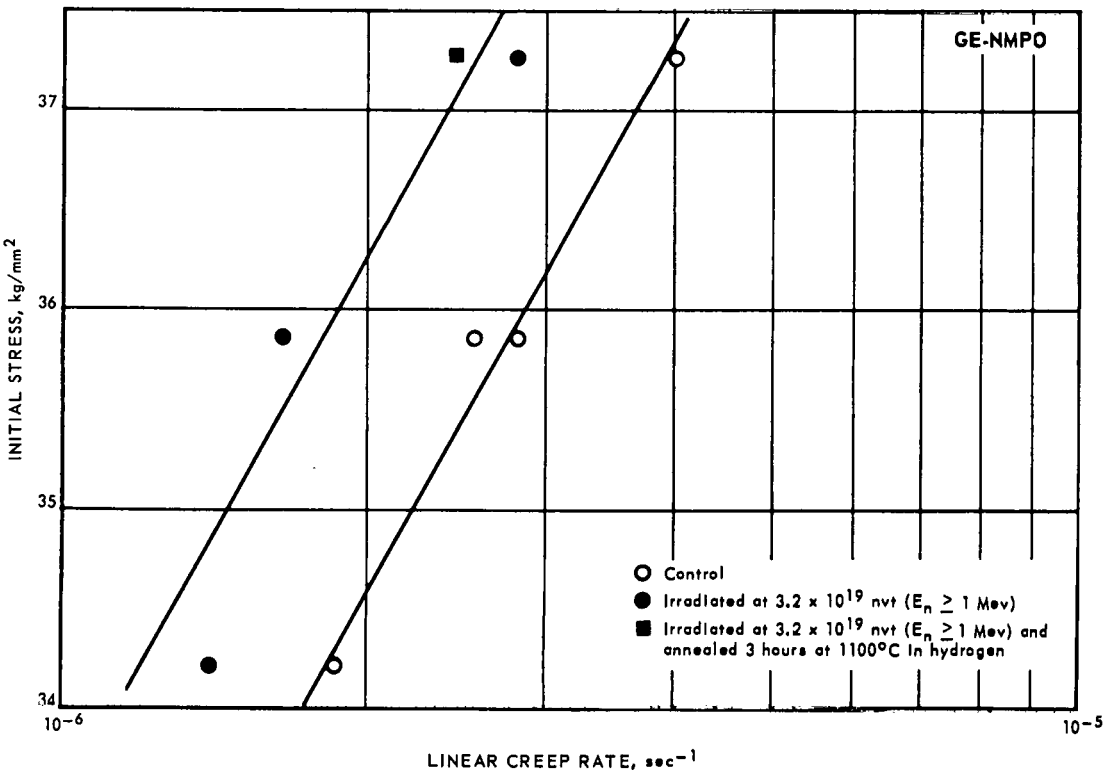

Fig. 3.7 – Initial stress versus linear creep rate of tungsten sheet specimens tested at 1100°C in hydrogen

creep rates than the control specimens. Irradiated specimen No. 204 was annealed in hydrogen for 3 hours at 1100°C prior to testing. Although the rupture life and creep rate varied slightly in comparison to an as-irradiated specimen (No. 207), the differences are not considered significant. Here again, the creep rates of the cold-worked specimens were reduced by a factor of about 1.6 and, as shown previously,* the creep rate of recrystallized tungsten was reduced by a factor of about 2.0 for a slightly lower fast neutron dose when tested at the same temperature.

An elongation versus time plot of the two irradiated specimens and a control specimen tested at 37.26 kg/mm^2 and 1100°C is shown in Figure 3.8. The 3-hour anneal of an irradiated specimen at 1100°C did not significantly change the creep curve.

Two control and one irradiated specimens were annealed at 1900°C in hydrogen for 1 hour and then tested at 1100°C. The irradiated specimen tested at a stress of 18.63 kg/mm^2

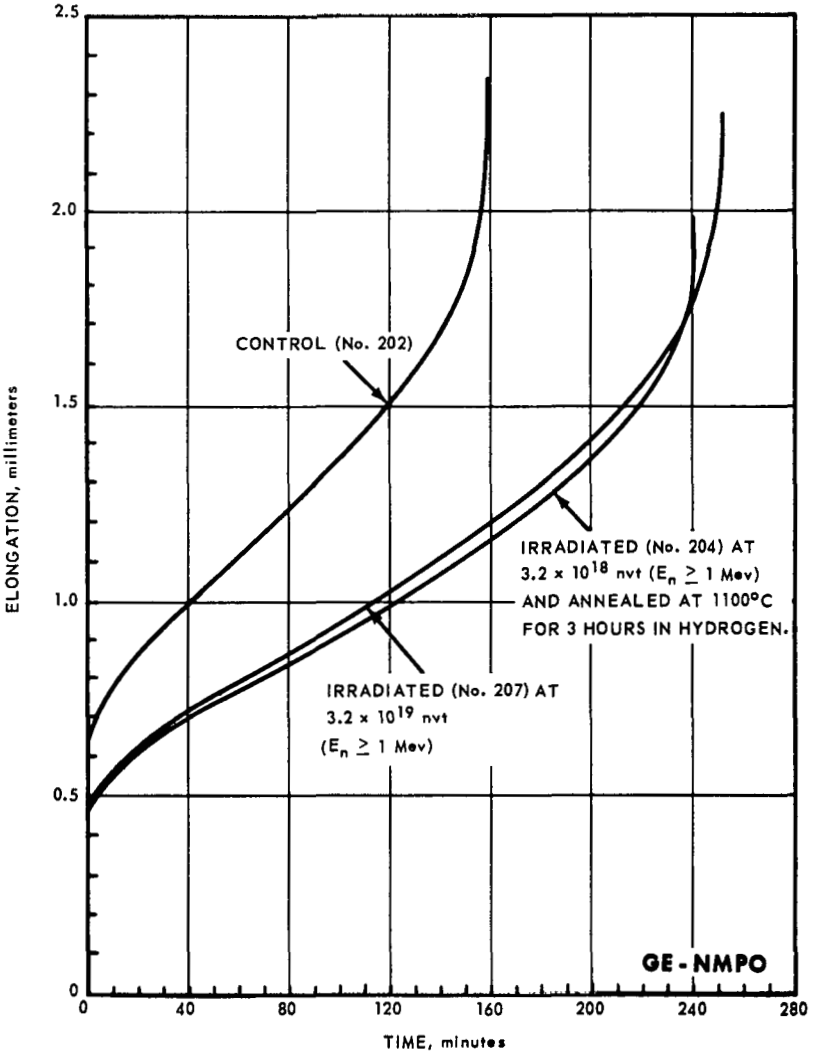

Fig. 3.8 – Elongation versus time for tungsten sheet specimens tested at 37.26 kg/mm^2 and 1100°C in hydrogen

*Ibid., Figure 3.7, p. 33.

possessed a longer rupture life and a slightly lower creep rate than the corresponding annealed control specimens. The elongation versus time plot of the two specimens is shown in Figure 3.9. These data, although limited, indicate that all of the radiation-induced strengthening is not removed by the recrystallization anneal at 1900°C. A similar effect has been observed in the tungsten resistivity tests. Annealing the irradiated specimens at 1900°C, for instance, did not completely remove the radiation-induced increases in resistivity. It can be noted that the third-stage creep appears to start at approximately the same elongation value for both specimens with the irradiated specimen exhibiting a longer period in third-stage creep prior to fracture.

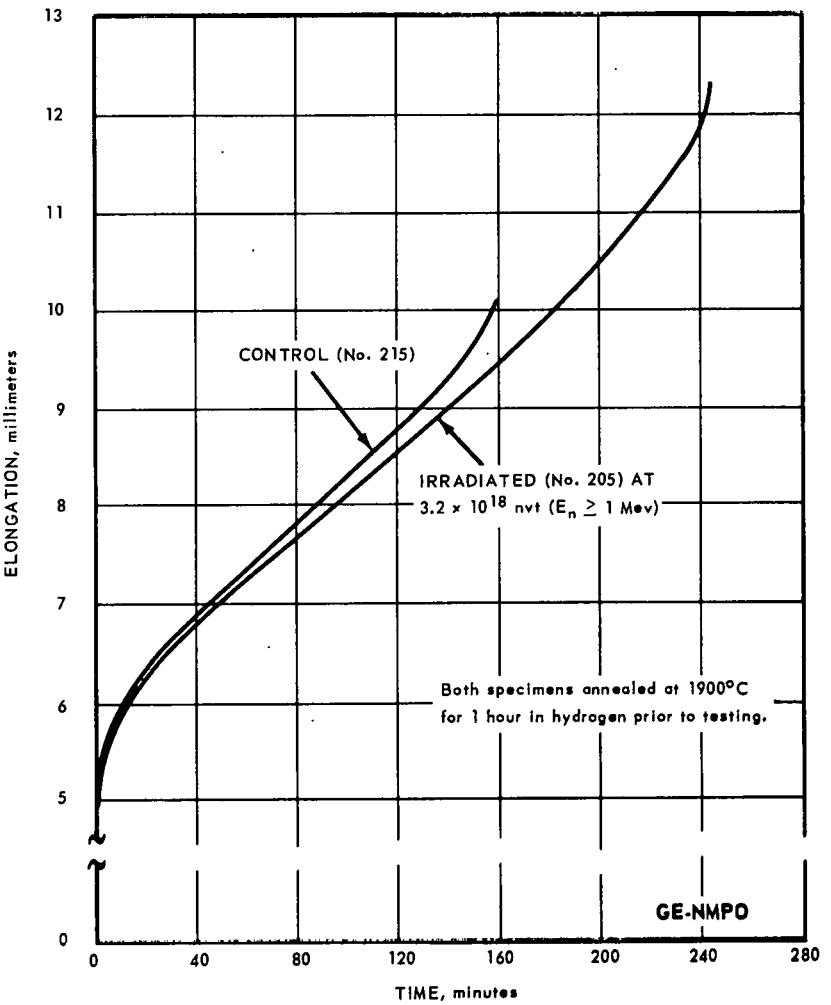

Fig. 3.9 – Elongation versus time for tungsten sheet specimens tested at 18.6 kg/mm^2 and 1100°C in hydrogen

Electropolished Specimens - Grinding of tungsten-rod specimens produces a distorted or cold-worked surface layer. The effective thickness of this layer varies with the many process variables. Most of the work reported in the literature, however, deals with the effect of surface finish on the room-temperature properties of refractory metals, and very little is reported for the elevated-temperature mechanical properties. Atkinson, et al.,*

*R. H. Atkinson, et al., "Physical Metallurgy of Tungsten and Tungsten-Base Alloys," WADD Technical Report No. 60-37, May 1960.

reported that as-ground tungsten single-crystal specimens, at room temperature, exhibited brittle fracture while electropolished specimens were ductile. Other investigators have reported*† the effect of surface conditions on tensile and bend properties of polycrystalline tungsten. Wolf‡ determined by X-ray back reflection investigation and room-temperature tensile tests on single-crystal tungsten specimens that an electrolytic diameter reduction of 0.051 millimeter was sufficient to remove the deformed surface layer. Stephan§ reported that 0.127 to 0.254 millimeter had to be removed from the diameter to eliminate the effect of the distorted surface layer on room-temperature tensile properties of polycrystalline tungsten specimens.

A series of creep-rupture tests was conducted at 1100°C at GE-NMPO on tungsten specimens with varying electrolytic diameter reductions. Electropolishing was accomplished with equipment and techniques previously described.• A summary of the tests is given in Table 3.3. Plots of the creep rates, rupture life, and final elongations are shown in Figure 3.10. As may be noted, diameter reductions up to 0.203 millimeter did not yield any significant changes in the creep rates, although there appeared to be a 3 percent increase. The scatter in results of specimens having 0.203 to 0.229 millimeter reductions is believed to be caused by misalignment. The same size split-collar grips designed for the larger diameter specimens were used for all tests. Note that all specimens with diameter reductions of less than 0.203 millimeter failed within 3.2 millimeter of the center of the gage length (44.5 mm). The final elongation of these same specimens varied from 12.5 to 13.7 millimeters which was within 5 percent of the average.

TABLE 3.3

CREEP-RUPTURE PROPERTIES OF ELECTROPOLISHED TUNGSTEN SPECIMENS[a]

Specimen No.	Diameter Reduction By Electropolishing, mm	Rupture Life, hr	Linear Creep Rate, 10^{-5} sec^{-1}	Final Elongation, mm	Point Of Failure
276	none	2.58	3.05	12.8	Center of gage length[b]
277	none	2.78	2.93	12.5	Center of gage length
272	0.104	2.20	2.98	12.8	3.2 mm below center of gage length
271	0.168	2.61	3.09	13.7	3.2 mm below center of gage length
274	0.208	1.66	3.80	12.2	7.9 mm below center of gage length
273	0.213	1.93	3.21	11.4	6.4 mm below center of gage length
275	0.234	2.39	2.45	10.8	11.1 mm below center of gage length

[a]Tungsten specimens from recrystallized rod L tested at 1100°C and 20.36 kg/mm^2 in a hydrogen atmosphere.
[b]Gage length is 44.5 mm.

The rupture life tends to show a decrease with the amount of surface removed by electropolishing consistent with the gradual increase noted in the corresponding creep rate. The scatter in the rupture-life data is probably caused by the sensitivity of third-stage creep mechanisms to the specimen alignment and also to the grain boundaries exposed to the surface which may be affected to some degree by the electropolishing. A nominal spread of ±18 percent is shown for the rupture life of the electropolished specimens. However, it

*J. R. Stephan, "Effect of Surface Condition on Ductile-To-Brittle Transition Temperature of Tungsten," NASA, TN D-676, Lewis Research Center, February 1961.

†J. R. Stephan, "An Exploratory Investigation of Some Factors Influencing the Room-Temperature Ductility of Tungsten," NASA, TN D-304, Lewis Research Center, August 1960.

‡U. E. Wolff, "Orientation Dependence of the Tensile Properties of Tungsten Single Crystals at Room Temperature," Report LMC-62-191, G.E. Co., Cleveland, Ohio, July 2, 1962.

§J. R. Stephan, op. cit.

•"High-Temperature Materials Program Progress Report No. 19, Part A," GE-NMPO, GEMP-19A, January 25, 1963, pp. 24–25.

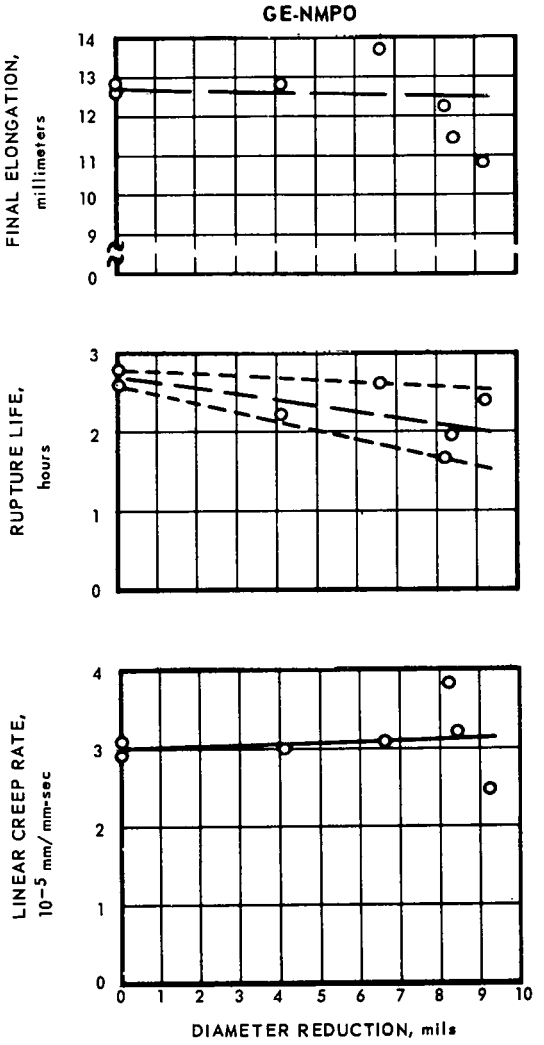

Fig. 3.10 – Effect of electropolishing on creep-rupture properties of tungsten

should be pointed out that the as-ground specimen data generated in the past showed good reproducibility when tested at the same temperature and stress.

Elongation and Reduction in Area - Ductility indices of tungsten-rod specimens have shown little spread in values. Rod Y specimen tested at 1100°C and 20.4 kg/mm^2,* for instance, yielded values which only deviated 2.4 percent in elongation and 1 percent in reduction in area from the average value, although these specimens were tested under five conditions: control, control annealed at 1400°C, irradiated ORM-6 and ORM-8, irradiated ORM-6 and ORM-8, and annealed at 1100°C or 1400°C.

A histogram plot of the ductility indices versus the three test temperatures for various stress levels of tests on Rod X material is shown in Figure 3.11. It indicates that the ductility of recrystallized tungsten decreases with temperature in the 1100° to 1400°C range and that irradiation decreased the ductility only slighly at all three temperatures.

*"High-Temperature Materials Program Progress Report No. 25, Part A," GE-NMPO, GEMP-25A, July 31, 1963, Table 3.3, p. 23.

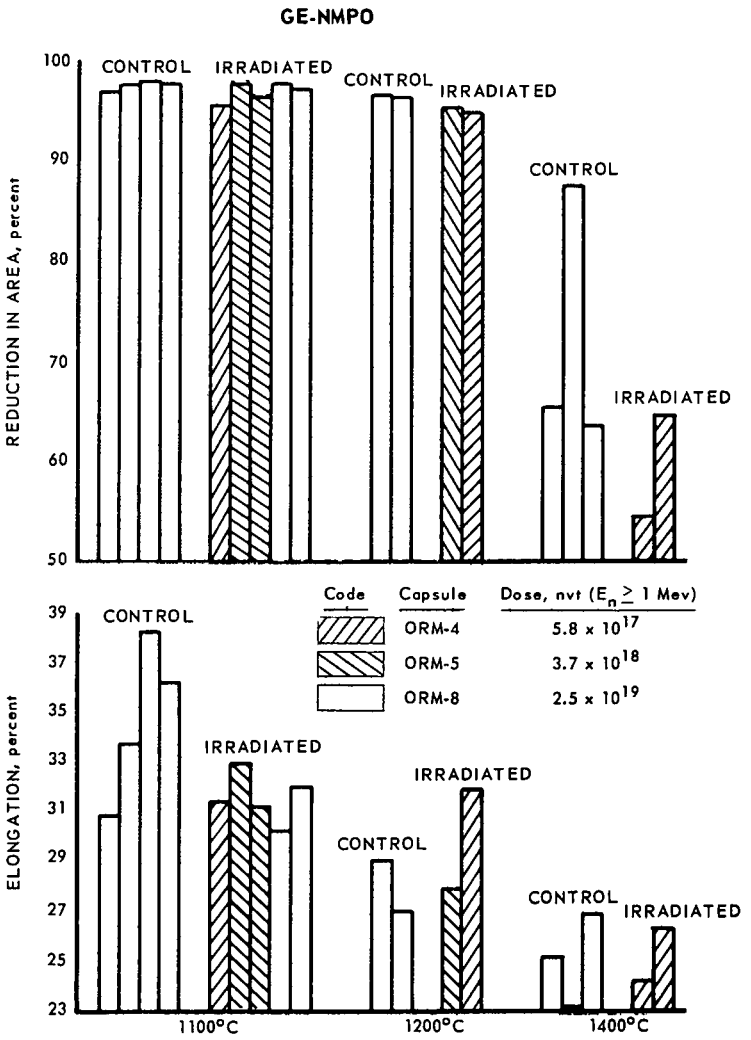

Fig. 3.11 – Ductility indices for tungsten (Rod X) creep-rupture-tested specimens

Resistivity Tests

The measurement of resistance change as a function of post-irradiation annealing of tungsten and W - 25Re continues to be a useful tool for observing radiation-induced defects. Primary emphasis during this report period was on isochronal annealing of irradiated specimens from capsule ORM-14. Isothermal annealing studies initiated previously* have been temporarily discontinued until the precision of the resistance measuring apparatus is improved. Higher currents will be used so that a greater potential drop across the test specimens can be obtained.

Three specimens from ORM-14, irradiated to a fast neutron dose of 1.3×10^{19} nvt are presently being examined in the following conditions:

1. Recrystallized tungsten irradiated in the as-received condition (No. 117).
2. Recrystallized tungsten irradiated following a 1-hour pre-irradiation heat treatment at 1900°C in H_2 (No. 175).
3. Recrystallized W - 25Re irradiated in the as-received condition (No. 700).

*"High-Temperature Materials Program Progress Report No. 27, Part A," GE-NMPO, GEMP-27A, September 30, 1963, p. 40.

In addition, a control specimen for each type of material with the corresponding heat treatment is annealed simultaneously with the irradiated sample. Tungsten specimen No. 117 has the same pre-irradiation treatment as those previously reported.*†

The measured resistivity for the three specimens and their corresponding control specimens as a function of annealing temperature is shown in Figure 3.12. The similarity of annealing behavior of the three specimens is illustrated in Figure 3.13 where the data are normalized to unity for the as-irradiated condition. The experimental points represent the new data generated for the samples from ORM-14; the two smooth curves represent the data reported previously which were obtained from other irradiations.* Additional data points generated at temperatures of 1740°C and 1900°C from specimens which were irradiated in capsules ORM-7 and ORM-11 are also shown in Figure 3.13.

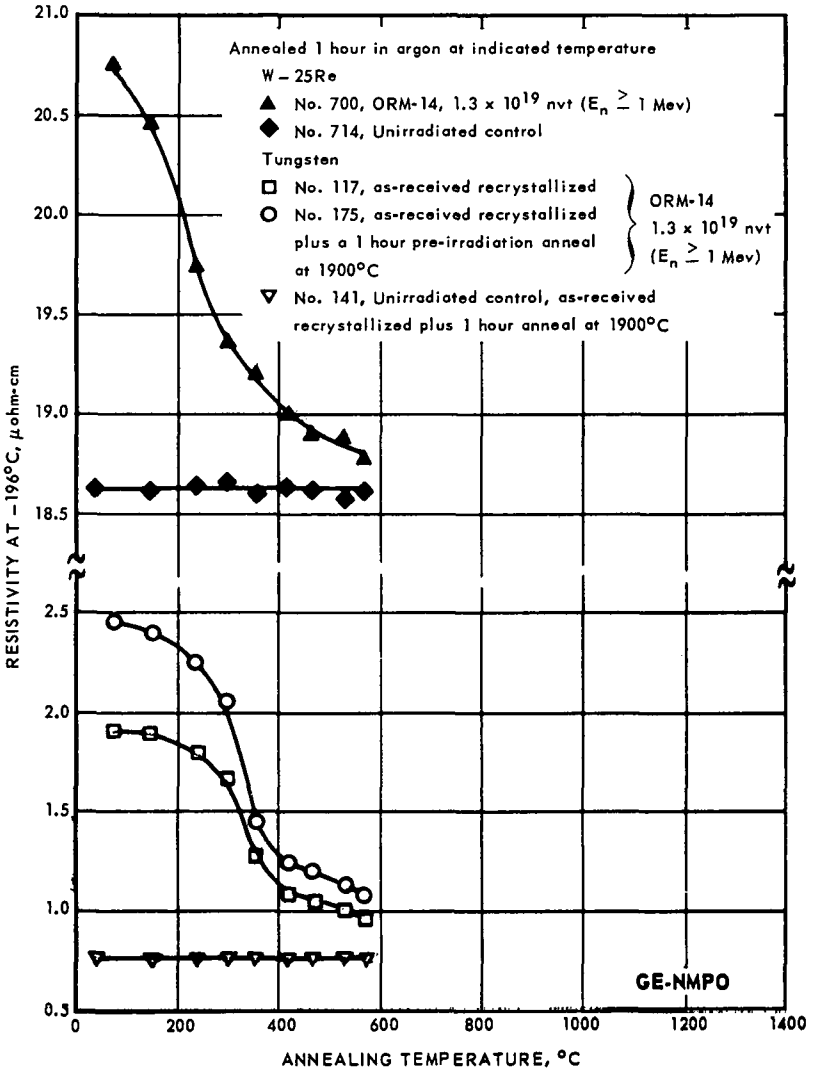

Fig. 3.12 – Isochronal recovery of irradiated tungsten and W – 25Re

*Ibid., Figure 3.9, p. 35.

†"High-Temperature Materials Program Progress Report No. 25, Part A," GE-NMPO, GEMP-25A, July 31, 1963, Figure 3.11, p. 31.

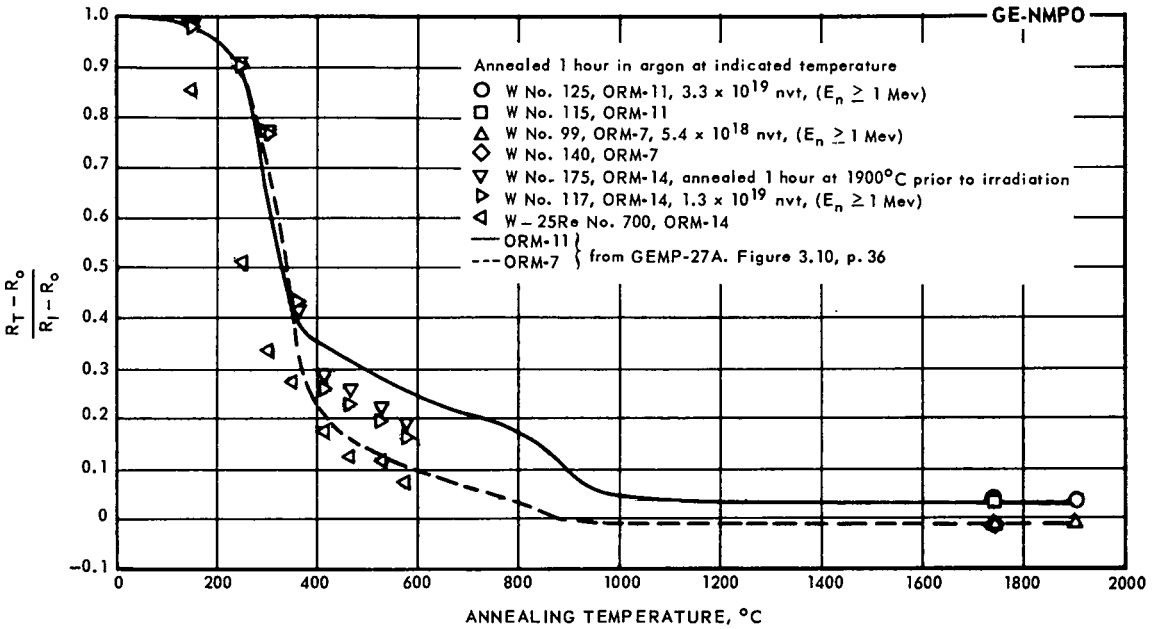

Fig. 3.13 – Normalized isochronal recovery of recrystallized irradiated tungsten and W – 25Re

The shape of the third-stage annealing curve in the temperature range of 200° to 350°C appears to be identical for all the tungsten specimens which were irradiated to various dosages. Above 350°C, the ORM-14 specimen data follow paths parallel to and are bracketed by the data from the other irradiations.

The tungsten specimen (No. 125) which received the 1900°C pre-irradiation anneal showed a greater increase in resistance. This increase was about 220 percent compared to an increase of about 140 percent for the as-received specimen (No. 117) which received about the same dose. The difference is also apparent in Figure 3.12.

Based on the data presented in Figure 3.14, it appears that the increase in resistance varies linearly with fast neutron dose above 5 x 10^{18} nvt for the as-received recrystallized

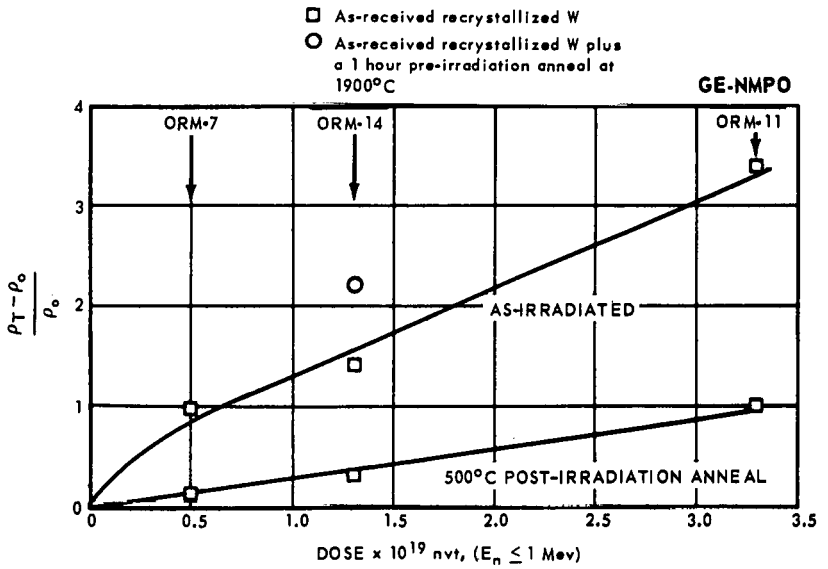

Fig. 3.14 – Increase in resistivity as a function of neutron dose

tungsten. After the post-irradiation 500°C annealing treatment the remaining radiation-induced resistivity increment appears to be a linear function of dose, even if extrapolated back to zero.

Figure 3.14 again shows the effect of pre-irradiation treatment on the observed radiation-induced changes. In each case, the value $(\rho_T - \rho_0)/\rho_0$ was calculated for a control (ρ_0) specimen which received a pre-irradiation heat treatment identical to the irradiated samples. The corresponding value of ρ_0 for specimen No. 175 was 0.76 micro-ohm centimeter, and for specimen No. 117 it was 0.78 micro-ohm centimeter.

The W - 25Re sample appears to have a recovery spectrum similar to tungsten, although about 100°C lower in temperature. In addition, the magnitude of the resistance increase caused by the irradiation is not as great for this material as that observed for tungsten. The W - 25Re control data (see Figure 3.12) shows scatter that is not observed in the tungsten control data. This amount of scatter, however, is small compared to the changes observed in the irradiated material during isochronal annealing.

HIGH-TEMPERATURE ALLOY PROGRAM

A-286 Creep-Rupture Tests

Testing of irradiated A-286 specimens from capsule 33MT-99 (4.9×10^{19} nvt, $E_n \geq 1$ Mev) was continued. Test results on heats RV403-5A and RV403-5C are plotted in Figure 3.15 and listed in Table 3.4. Irradiated specimens from heat RV403-5A (0.00085% B) show consistent and significant losses in rupture life and in ductility. Heat RV403-5C (0.010% B) did not exhibit significant changes in the rupture life when compared to the control data of both heats, although there was a significant reduction in the elongation.

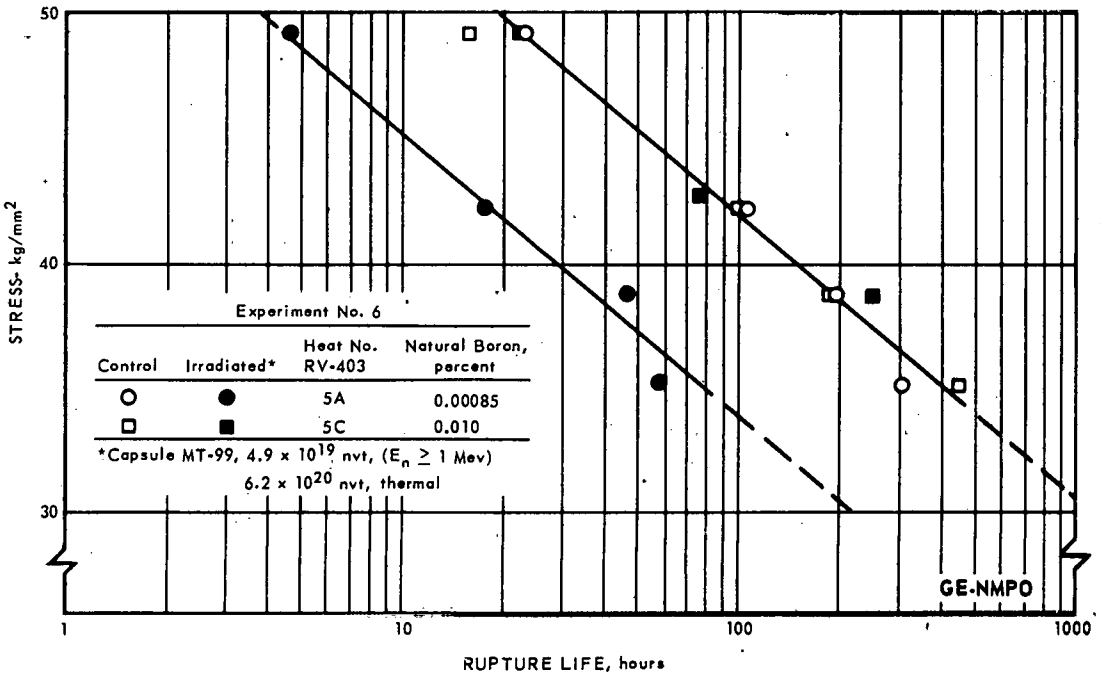

Fig. 3.15 – Stress-rupture strength of boron-containing A-286 specimens at 650°C

The creep behavior of specimens for a stress of 38.7 kg/mm² and at 650°C from both heats is shown in Figure 3.16. Very little variation is noted for the control data from each heat. The second-stage creep rate, however, appears to be significantly reduced

TABLE 3.4

STRESS-RUPTURE RESULTS ON A-286 SPECIMENS AT 650°C

Specimen	Heat	Stress, psi	Stress, kg/mm²	Rupture Life, hours	Elongation, percent in 3.81 cm	Reduction In Area, percent
Controls						
112AS[a]	RV403-5A[b]	50,000	35.2	305.9	11.2	26.8
113AS	RV403-5A	55,000	38.7	194.5	7.67	19.1
111AS	RV403-5A	60,000	42.2	106.3	17.7	22.2
114AS	RV403-5A	70,000	49.2	23.3	17.3	25.2
147AS	RV403-5C[b]	50,000	35.2	456.7	(11.2)[c]	-
145AS	RV403-5C	55,000	38.7	191.9	10.5	31.8
144AS	RV403-5C	60,000	42.2	98.8	21.5	33.1
146AS	RV403-5C	70,000	49.2	15.7	12.3	33.4
Irradiated (33MT-99)						
106AS	RV403-5A	50,000	35.2	58.9	(0.7)[c]	-
107AS	RV403-5A	55,000	38.7	46.4	(0.7)[c]	-
104AS	RV403-5A	60,000	42.2	18.0	1.9	~4.1
110AS	RV403-5A	70,000	49.2	4.6	(0.8)[c]	-
140AS	RV403-5C	55,000	38.7	252.1	(1.9)[c]	-
137AS	RV403-5C	60,680	42.7	76.9	(1.6)[c]	-
143AS	RV403-5C	70,000	49.2	22.4	(1.7)[c]	-

[a]Estimated dose - 5 x 10^{19} nvt, $E_n \geq 1$ Mev.
[b]RV403-5A contains 0.00085 percent natural boron.
RV403-5C contains 0.010 percent natural boron.
[c]Estimated from dial gage elongation measurements.

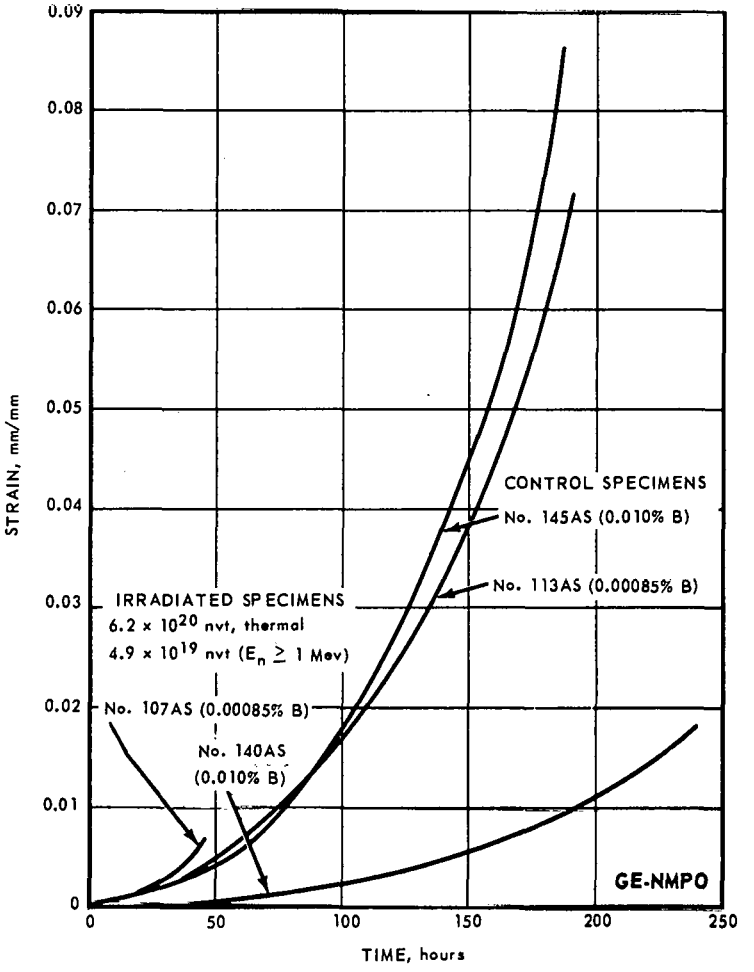

Fig. 3.16 – Strain versus time curves for boron-containing A-286 specimens at 650°C and 38.7 kg/mm²

(approximately by a factor of 5) for the irradiated specimen from the 0.010-percent B-containing heat. A factor of about 4 to 5 reduction in elongation is also observed. The second-stage creep rate of the specimen from the low-boron-containing heat (0.00085% B) appears to be similar to that of the control specimen from both heats for the first 20 hours of test, but it appears that the duration of the third-stage creep was much shorter. There was about a factor of 10 reduction in elongation of this specimen when compared to the control specimen tested at the same stress. The pronounced effect of the irradiation on the lower percentage of boron may be caused by the depletion, by some mechanism, of critical amounts of boron atoms which are most likely present in the grain-boundary regions. The possible grain-boundary boron depletion and the subsequent influence it may have on the local stoichiometry of the principal elements of the various precipitate phases in this alloy under stress,* may result in the observed poor third-stage creep properties.

A model will be postulated to explain these observed differences after the microstructure of the stressed regions of these specimens has been observed by optical and electron microscopy.

Structure Studies

Electron microscope studies on Rene' 41 and Hastelloy X control and irradiated specimens have been in progress, and some of the preliminary observations are discussed below. These observations were made in the unstressed button-head region of the test specimen and may not reflect the phase changes or distributions which may have occurred in the stressed portion of the specimen.

At a test temperature of 650°C, the irradiated Rene'41 material appears to contain more grain-boundary precipitate and a more continuous grain-boundary precipitate than the unirradiated material. The periphery of the intragranular precipitates appears to be attacked more heavily by the etchant on the irradiated material. The irradiated material, given a standard heat treatment, also appears to contain less and larger γ' precipitate phase than the unirradiated material, especially at 870°C. This phase size, however, is quite sensitive to pre- and post-irradiation heat treatment.

The Hastelloy X material did not show any observable changes caused by irradiation when tested at 650°C. At the higher test temperature (870°C), the precipitate particles tend to take a more regular (geometrical) shape and are more aligned along crystallographic planes in the irradiated material.

FUNDAMENTAL STUDIES

Introduction

These studies concern computer experimental results on the initial (primary) damage state produced in iron by external-source neutron irradiation. In this context the term "damage state" refers to the way in which defects, directly produced during irradiation, are distributed at the level of atomic dimensions, as well as the total number of defects produced. An attempt was made to estimate how the damage state produced by neutrons from a given energy spectrum changes as a function of the irradiated sample size and to compare the damage states produced in a sample of a given size by neutrons from different energy spectra. The earlier work estimated the difference between the primary damage states produced in iron by irradiation in the Oak Ridge Graphite Reactor (ORGR) and that produced by irradiation in the water-moderated Engineering Test Reactor (ETR).† In the

*R. F. Decker, J. P. Rowe, and J. W. Freeman, "Boron and Zirconium from Crucible Refractories in a Complex Heat-Resistant Alloy," NACA-1392, 1958.

†See Appendix A for a description of the neutron spectra used in these calculations to represent irradiations in the ETR and ORGR.

course of this research it became apparent that the size of the sample and the angular distribution of the incident neutrons exerted an influence comparable to that associated with a major change in the neutron energy spectrum.

Short descriptions of the size effect in iron samples have been given in earlier papers.* A more complete account of this particular effect and a general description of the damage state produced in neutron-irradiated iron at low (liquid helium) temperature are given in the present study. All of the results presented were obtained in a series of computer experiments wherein samples of a given size and shape were irradiated by neutrons from either an isotropic incident distribution or a collimated beam entering the sample at normal incidence. The radiation conditions for which these calculations are appropriate are as follows: A single sample was assumed to be positioned in a reactor test hole so that neutrons impinged upon each free surface of this sample. It was also assumed that the sample was sufficiently small so that the flux perturbation it produced was completely negligible and that the irradiation temperature was sufficiently low that all defects produced were immobile. Finally, the radiation exposure was assumed to be sufficiently small so that the damage state produced was always heterogeneous.†

The effect of sample size, neutron angular distribution, and neutron energy spectrum on the damage state produced in a finite sample are of both theoretical and technological interest. In the theoretical sense, the results indicate that the damage state produced in wires and foils subjected to the same incident neutron energy-angle spectrum and exposure need not be identical, and should in fact exhibit significant differences. Specifically, an irradiation exposure sufficiently small to produce only a heterogeneous damage state in wires can produce a homogeneous state in foils. It is not necessary to elaborate upon the possible confusion to which this circumstance could lead in an attempt to reconcile wire and foil radiation effects data. From a technological standpoint, the results indicate that there is a distinct possibility that the use of mechanical property data obtained from the irradiation of small‡ samples, as a basis for designing large structural parts in a nuclear reactor, can lead to faulty engineering decisions. The computational method employed can also be used to analyze the response of certain solid-state dosimetry elements to different neutron spectra, but no calculations of this nature were performed at this time.

Most of the computations were performed for slabs and square-base parallel-piped columns. Supplementary runs for semi-infinite and infinite sample geometry were made to provide limiting values and also a means for assaying the intrinsic worth of using infinite medium calculation results in the analysis of radiation damage data for finite samples. The smallest slab thickness or column base dimension considered was 0.02 centimeter, i,e., 0.008 inch foils and wires. Recent quenching experiments done by Cotterill and Segall§ show that the loss of defects to surface sinks in foils less than 0.01-centimeter thick is sufficiently large that the results of damage state calculations for low-temperature irradiation should have little significance as a basis for estimating the damage state after annealing at an elevated temperature. However, they found this loss to be negligible in

*J. R. Beeler, Jr., "Effect of Sample Size on Neutron Damage in Iron," *Transcripts of American Nuclear Society*, Vol. 6, 1963, p. 144; J. Moteff and J. R. Beeler, Jr., "Reactor Spectrum Determination and Its Influence on Primary Knock-On Atom Spectra in Finite Test Specimens," Neutron Dosimetry, pp. 461–479, International Atomic Energy Agency, Vienna, 1963.

†A heterogeneous damage state is one wherein the individual primary knock-on cascade damage regions do not overlap; a homogeneous damage state is one wherein these regions do overlap.

‡A later section "Sample Size Criteria" is devoted to the definition of small and large samples. For the present consider a small iron sample as one with dimensions less than 1.5 cm.

§R. M. J. Cotterill and R. L. Segall, "The Effect of Quenching History, Quenching Temperature, and Trace Impurities on Vacancy Clusters in Aluminum and Gold," *Philosophical Magazine*, Vol. 8, 1963, p. 1105.

0.025-centimeter foils. This being the case, the results presented for dimensions ≥ 0.02 centimeter should give an appropriate qualitative description of the initial, atomic-level damage state from which bulk annealing processes would proceed at an elevated temperature after a low-temperature irradiation.

The largest finite dimension thickness or base dimension, considered with the assumption of a macroscopically uniform damage distribution, was 8 centimeters. This upper limit was determined conservatively from Reif's * Monte Carlo calculations of the spatial variation of the energy deposition in neutron-irradiated iron slabs. According to his results, the radiation-induced defect concentration should be nearly uniform in an iron sample, irradiated under the conditions assumed in the present study, with thickness less than 12.7 centimeters.

Computational Model

Radiation damage formation in neutron-irradiated metals can be thought of as a two-stage process. In the first stage, neutrons displace a set of metal atoms from their normal sites in the crystal. In the second stage, each of these energetic displaced atoms, called primary knock-on atoms, subsequently displaces other metal atoms in a cascade of elastic collisions as illustrated in Figure 3.17. (Ionization and excitation collisions do not produce displacements in metals.) The fundamental characteristics of the primary damage state produced by neutron irradiation are: (1) the number of displacements produced per cm^3 per unit exposure, (2) the number of primary knock-on atoms produced per cm^3 per unit exposure, (3) the size distribution of the cascade damage region volumes produced by primary knock-on atoms, and (4) the size distribution of vacancy and interstitial atom clusters produced within a primary knock-on atom cascade damage region.

If the differential energy spectrum, f(E), for the primary knock-on atoms (PKA) produced by neutron irradiation is known, as well as the number of PKA produced per incident neutron, Y, and the average number of atomic displacements, g(E), created by a PKA with energy E, then the total number of displacements, D, produced per incident neutron is given by:

$$D = Y \int_0^\infty g(E)\, f(E)\, dE \qquad (1)$$

A Monte Carlo calculation† was used to compute f(E) and Y. A deterministic dynamic calculation‡ (CASCADE), which accounted for the influence of the exact lattice structure of the irradiated metal sample, was used to compute the displacement function g(E). If a sample is sufficiently small that the macroscopic PKA concentration is uniform, the number of vacancies, d, and the number of PKA, y, produced per unit volume by a unit exposure of one incident neutron/unit area of sample surface are:

$$d = D/\beta \qquad (2)$$

$$y = Y/\beta \qquad (3)$$

where β is the volume-to-surface ratio for the sample.

The ratio D/Y is the average number of atoms displaced by a PKA and is proportional to the average volume of the region damaged by a PKA. Program CASCADE results in-

*H. Rief, "Calculation of the Energy Deposition Due to Elastic Neutron Scattering by a Monte Carlo Technique," *Transcript of American Nuclear Society*, Vol. 6, 1963, p. 142.

†J. R. Beeler, Jr., and J. L. McGurn, "A Method for Computing Primary Knock-On Spectra and Populations In Polyatomic Material Irradiated by Neutrons," GE-NMPO, GEMP-101, 1961.

‡D. G. Besco and J. R. Beeler, Jr., "Computer Programs Describing Collision Cascades in Binary Materials, Parts I, II, and III," GE-NMPO, GEMP-192, GEMP-200, and GEMP-243, 1963.

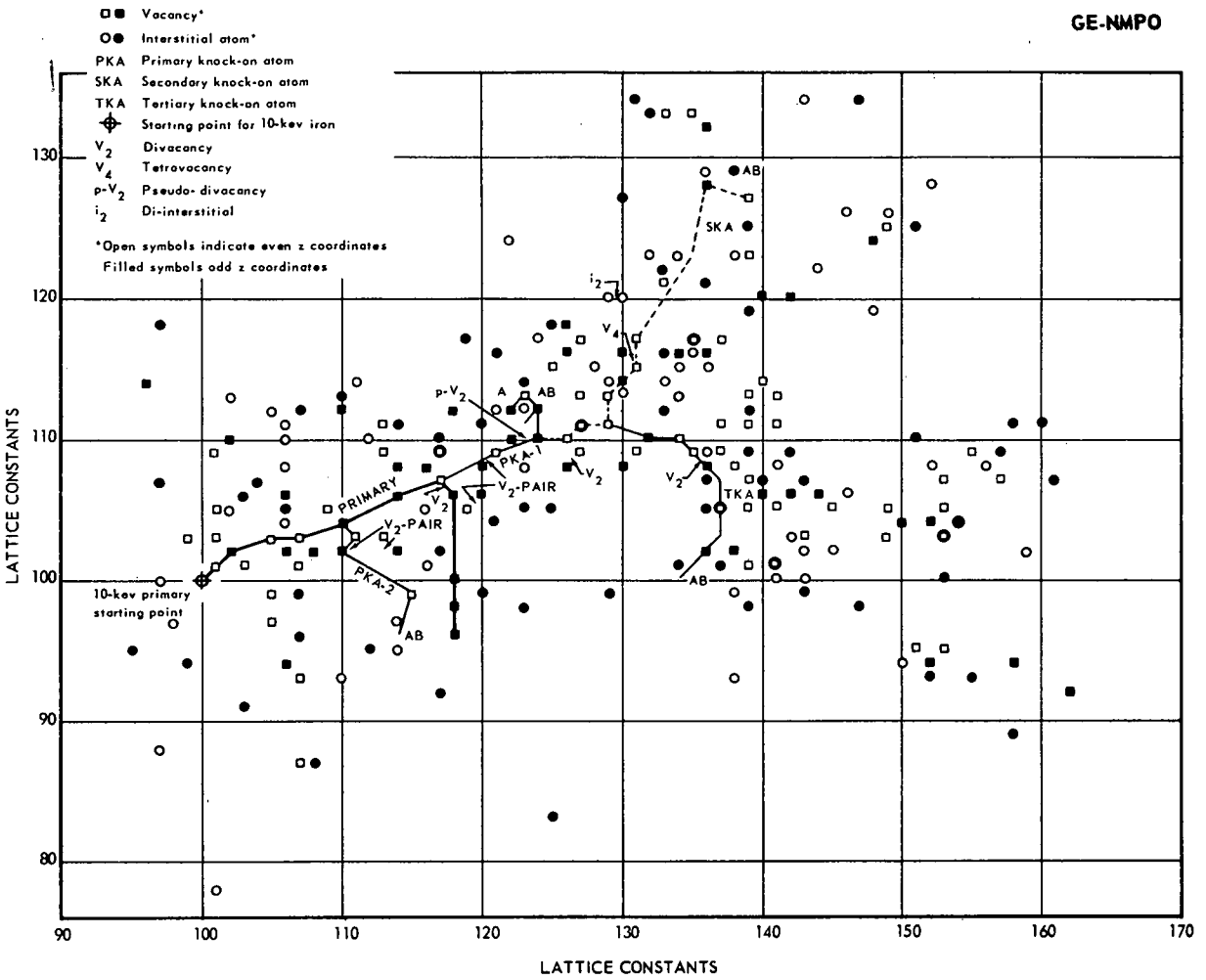

Fig. 3.17 – Damage pattern produced in an elastic collision cascade initiated by a 10 kev iron atom in iron

dicated an average initial displacement concentration of 3 atomic percent in a PKA cascade volume at 0°K. This amounts to an average volume of 33.3 Ω per displacement in iron (BCC) where Ω is the volume per atom. Preliminary Monte Carlo annealing calculations, based on the initial, non-uniform, atomic level damage state computed by Program CASCADE, indicate that approximately 50 percent of the mobile defects anneal out within a time interval $\Delta\tau = 25\tau$, where τ is the mean jump time for the mobile defect with the largest jump frequency.

Anisotropic neutron scattering in the center of mass system as a function of neutron energy and nuclear type was presented by using experimental angular distribution data* (Appendix B) in the Monte Carlo calculation. PKA displacements by neutrons were assumed to result only as a consequence of elastic neutron scattering with nuclei. A neutron history was terminated when the neutron either was absorbed, escaped from the sample, or slowed down to such a low energy (< 350 ev) that it could no longer produce displacements

*M. D. Goldberg, V. M. May, and J. R. Stehn, "Angular Distributions in Neutron-Induced Reactions," Sigma Center, Brookhaven National Laboratory, BNL-400 (Revised), 1962.

via elastic collisions. The recoil displacement mode associated with thermal neutron absorption was ignored.* A displacement energy E_d = 25 ev was adopted for iron in the Monte Carlo PKA production calculations, but the value, 16 ev, was used in the Program CASCADE calculations for g(E) and the distribution of defect cluster sizes. The reasons for using these apparently different displacement energy assignments are as follows:

1. The displacement energy is a function of direction in a crystal. Vineyard's group† found that E_d ranges from 17 to 38 ev in iron and exhibits a well-defined value for each principal crystallographic direction. Therefore, a middle-ground displacement energy of 25 ev was assumed in the continuous medium Monte Carlo calculations for PKA production by neutrons.
2. In Program CASCADE, however, a displacement decision is based on the direction of the ejected atom and the local, discrete atomic configuration in the BCC iron lattice. The appropriate displacement energy for use in Program CASCADE is that for the easiest displacement direction (16 to 17 ev). A full description of how CASCADE decides whether or not an atom is displaced is given elsewhere.‡ Frenkel pairs separated by no more than one lattice constant are automatically strain annealed (annihilated) by CASCADE during the PKA collision cascade computation, in view of the Brookhaven results on Frenkel pair stability at $0^{\circ}K$.

In order to illustrate the essential parts of the neutron-trajectory tracing routine, a slab geometry is considered for the sake of simplicity. Let the slab thickness be t, the total macroscopic cross section be Σ, and the incident neutron angle with respect to the slab normal be θ. Each incident neutron was forced to make at least one collision in the sample and given an initial weight:

$$W_o = 1-\exp(-\Sigma t/\cos\theta) \tag{4}$$

The neutron free path from the entry point to its first collision point was selected from the conditional free path distribution $f_c(x)$, associated with the forced collision condition:

$$f_c(x) = \Sigma \exp(-\Sigma x/\cos\theta) \,/\, W_o \tag{5}$$

where x is the neutron penetration distance along the direction normal to the incident plane surface. The weight assigned to any PKA produced in the n-th neutron collision was:

$$W_n = W_{n-1}\,(\Sigma_n^s / \Sigma_n) \tag{6}$$

which is the weight of a neutron leaving the n-th collision. Each calculation used 10^4 neutron histories.

In general, the best estimates were obtained by forcing a number of collisions approximating the average number of collisions pertinent to the sample size concerned. If grossly more than the average number of collisions were forced, round-off errors would tend to show up in the form of fourth place inaccuracies in the PKA energy cumulative distribution function and the neutron balance. Tallies on the neutron collision, absoprtion, slowing down, and escape weights were kept to check neutron balance. If the neutron balance deviated by more than 0.01 percent from unity the run was discarded and forced collision requirements were modified until a proper balance was achieved.

*R. E. Coltman, Jr., C. E. Klabunde, D. L. McDonald, and J. K. Redman, "Reactor Damage in Pure Metals," *Journal of Applied Physics*, Vol. 33, 1962, p. 3509.

†C. Erginsoy, G. H. Vineyard, and A. Englert-Chowles, "Dynamics of Radiation Damage in a Body-Centered Lattice," to be published.

‡J. R. Beeler, Jr., and D. G. Besco, "Range and Damage Effects of Tunnel Trajectories in a Wurtzite Structure," *Journal of Applied Physics*, Vol. 34, 1963, p. 2873; "Defect Configurations in Heavy-Atom Bombarded BeO," *Journal of Physical Society*, Japan, Vol. 18, Supplement III, 1963, p. 159.

An ionization collision energy threshold:

$$E^* = A \text{ kev} \tag{7}$$

was assumed in the PKA production calculations where A is the mass number of the metal atom.* Using this notation Equation (1) becomes:

$$D = Y \int_0^{E^*} g(E)\, f(E)\, dE + YE^* g(E^*)\, (1 - F^*) \tag{8}$$

where:

$$F^* = \int_0^{E^*} f(E)\, dE \tag{9}$$

is the fraction of all PKA produced with energies below E^*.

The displacement function used was that given by Program CASCADE:

$$g(E) = 0.376\ (E/E_d) \qquad 0 < E \leq 1.1 \text{ kev}$$

$$g(E) = 0.34\ (E/E_d) \qquad 1.1 < E \leq 12 \text{ kev}$$

$$g(E) = 0.28\ (E/E_d) \qquad 12 < E \leq 56 \text{ kev} = E^*$$

$$g(E) = g(E^*) \qquad E > E^*$$

where E_d is the displacement threshold energy. As the energy of a PKA increases, either it or its progeny tend to follow open channels in the crystal lattice.†‡ Energetic atoms produce negligible damage when following channel trajectories (paths) and this effect serves to make g(E) a decreasing function of energy in the elastic collision range. Damage production could be overestimated in the present calculations for at least two reasons:

1. The collision model used in Program CASCADE may slightly overestimate the magnitude of g(E);
2. PKA can in fact experience ionization collisions at energies less than E^*.§

Semi-Infinite and Infinite Media

Calculations were performed for infinite and semi-infinite media to provide a reference base for interpreting the results for samples with more than one free surface. In samples with more than one free surface, there are two transport modes for neutron loss, e.g., reflection and transmission. The effect of reflection loss was isolated by comparing the damage produced in an externally irradiated semi-infinite medium with that produced in an infinite medium containing an internal source. Calculations for slab geometry provided information on the essential changes in the damage state induced by allowing transmission loss in addition to reflection loss. Both monoenergetic and distributed neutron-energy spectra were used in the semi-infinite medium calculations to characterize the dependence of the damage state upon neutron energy.

*G. J. Dienes, and G. H. Vineyard, *Radiation Effects in Solids*, Interscience Publishers Inc., 1957, p. 9; H. Wollenberger, "Die Energieverteilung der Primaratome in Kupfer bei Bestrahlung mit Schnellen Monoenergetischen und Reaktor Neutronen," *Nukleonik*, Vol. 4, 1962, p. 25.

†M. D. Goldberg, V. M. May, and J. R. Stehn, "Angular Distributions in Neutron-Induced Reactions," Sigma Center, Brookhaven National Laboratory, BNL-400 (Revised), 1962.

‡D. G. Besco and J. R. Beeler, Jr., "Energetic Atom Tunneling in b.c.c.–f.c.c. Materials," *Bulletin of American Physical Society*, Vol. 8, 1963, p. 339.

§F. P. Ziemba, G. J. Lockwood, G. H. Morgan, and Everhart, "Resonant Electron Capture and Stripping in Moderately Large-Angle Atomic Collisions," *Physical Review*, Vol. 118, 1960, p. 1552; V. V. Afrosimov, Y. Gordeev, M. N. Panov, and N. V. Frederenko, "Characteristic Energy Losses in Single Collisions," to be published.

The monoenergetic source runs are first discussed and then those done using the ETR and ORGR distributed neutron-energy spectra (Appendix A). Individual damage contributions from each of the first five collisions of 1 Mev and 0.1 Mev neutrons are discussed to illustrate how the damage state evolves as a function of neutron collision order. This simple example also shows why the sample size can importantly affect the damage state. A collision order analysis was also applied to small samples, but the computational precision in these instances was not as good as it was in large sample calculations. All detailed discussion of the collision order analysis is, therefore, confined to large samples.

Semi-Infinite Medium: Monoenergetic Sources - Damage characteristics associated with complete neutron histories in semi-infinite iron are listed in Table 3.5 for irradiation by isotropically incident, monoenergetic neutrons. The most important feature of the data shown in this table and Figure 3.18 is the separation of the neutron-energy range into a light damage region and a heavy damage region. There are several indications that the damage state produced in iron by neutrons with energies less than approximately 1.5 Mev is qualitatively different from that produced by neutrons with energies above 1.5 Mev. All of these indications arise essentially from the circumstance that neutrons with energies in excess of 0.8 Mev are required to produce PKA with energies above the ionization limit (56 kev), a marked transition to highly forward scattering as the neutron energy increases from 1 to 3 Mev, and the existence of a broad minimum in the total neutron collision cross section which is centered about 1.2 Mev. To avoid confusion, PKA energies will always be expressed in kev and neutron energies in Mev.

TABLE 3.5

DAMAGE PARAMETERS FOR MONOENERGETIC NEUTRON IRRADIATION OF A SEMI-INFINITE IRON MEDIUM

E, Mev	Y	D	D/Y	<E>, kev	D*/D, %	ν_{max}	K*
9.5	47.8	22,900	478	49.0	45.3	15	0.2209
6.0	41.5	15,800	382	36.9	40	15	0.1552
3.0	37.5	11,500	306	24.0	40	15	0.1416
2.0	29.7	8,724	294	20.0	44.5	15	0.1333
1.0	28.5	5,360	188	10.5	9.5	15	0.0183
0.5	28.6	2,890	101	5.3	0	12	0
0.32	29.5	2,021	68.6	3.4	0	11	0
0.10	24.3	665	27.3	1.3	0	8	0
0.01	15.1	58.9	3.9	0.17	0	3	0

First of all, note that the fraction D*/D of all displacements caused by PKA with energies above E^* rises abruptly from 0.095 at 1 Mev to approximately 0.4 at 2 Mev. In addition, the average number of displacements, D/Y, in a single PKA cascade and the PKA yield per incident neutron, Y, both change significantly at about 1.5 Mev. D/Y is approximately 300 to 400 above 1.5 Mev, but it is approximately 100 below this energy. The curves of Figure 3.18 clearly illustrate these features. As mentioned earlier, D/Y is proportional to the average PKA cascade damage region volume and hence determines the level of neutron irradiation exposure required to produce a homogeneous damage state. Because no displacements are caused by ionization collisions and the assumption that all PKA with energies less than E^* experience only elastic collisions, the maximum value of D/Y, in this model, is found by Equation (10) to be 980.

The largest D/Y value obtained was 697 for 9.6 Mev irradiation of a small column. Because D/Y is the average number of displacements per PKA over all PKA energies, it must always be less than 980. ν_{max} is the largest vacancy cluster size, given by the

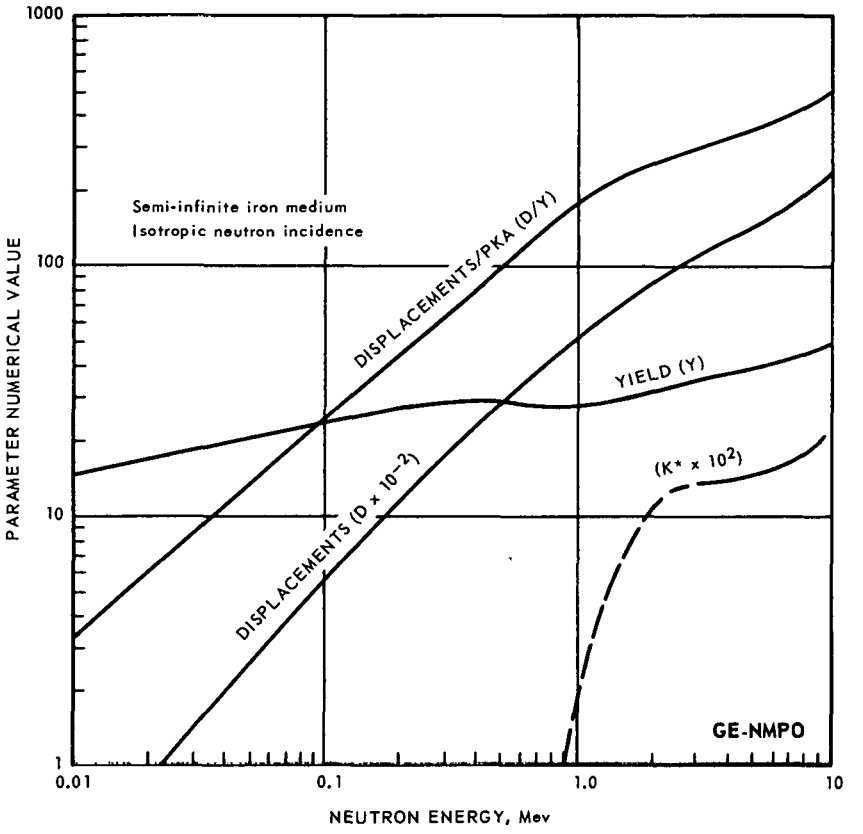

Fig. 3.18 – Damage parameters for a semi-infinite iron medium as a function of neutron energy for isotropic neutron incidence

CASCADE calculations, that can be created by any PKA produced during the collision history of a neutron entering the sample at the energy indicated. Let v* be the biggest vacancy cluster possible, i.e., a 15-vacancy cluster. The number of v* clusters produced is proportional to the large cluster factor, K* = (1 - F*), which also rises abruptly over the interval 1 to 2 Mev. These observations lead to the conclusion that neutrons with energies above 1.5 Mev produce a damage state containing large vacancy clusters v* and relatively large PKA cascade damage regions. Neutrons with energies below 1.5 Mev produce relatively small PKA cascade damage regions and only a small number of large v* clusters.

A rough description of how the displacement contributions of PKA in the energy ranges 0 to 1.0 kev, 1.1 to 12 kev, 12 to 56 kev, and greater than 56 kev change with neutron energy is given by the data points connected by line segments in Figure 3.19. The rise in Curve IV, above 6 Mev, is a direct consequence of the rise in K* over this energy range. Note that only PKA with energies above 12 kev contributed importantly to displacement production when the neutron energy exceeds 1.5 Mev. On the other hand, in the case of low-energy neutron irradiation (< 0.5 Mev), over half of the displacements are produced by PKA with energies below 12 kev. This circumstance is significant from the standpoint of annealing characteristics. As the energy of a PKA increases, v_{max} also increases. PKA start to produce clusters of 8 to 9 vacancies consistently at about 12 kev. Clusters of this size or larger show a strong tendency to grow by collecting mobile vacancies in these Monte Carlo annealing calculations.

There appear to be two factors which enhance this growth of large clusters in addition to the purely geometric circumstance that the probability for a migrating vacancy to inter-

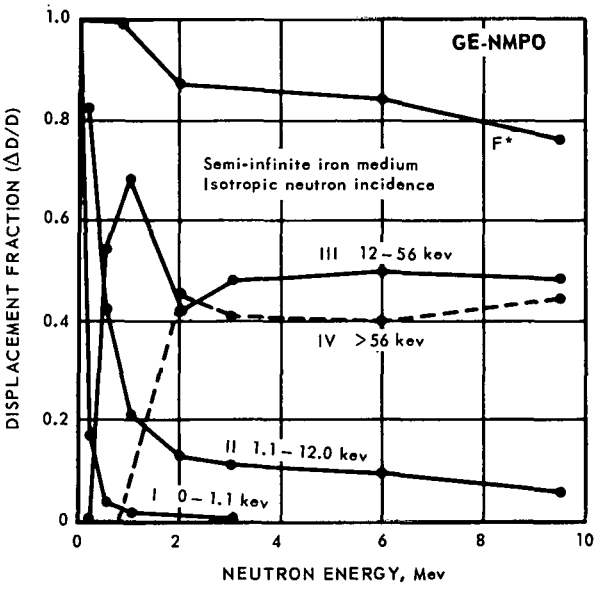

Fig. 3.19 – The fraction ΔD/D of all displacements produced by PKA, with energies in the four ranges indicated, as a function of neutron energy

cept a cluster increases with cluster size. First; clusters of the size concerned were usually found in regions relatively free of interstitial atoms, a damage configuration similar to Seegar's depleted zone concept.* This configuration appears to be the consequence of displaced atom escape from the cluster center to the periphery of the damage region via channeling and quasi-channeling. The absence of interstitials increases the probability that mobile vacancies in the vicinity of the cluster will migrate to it during annealing and decreases the vacancy-interstitial recombination probability. Second; lines of single vacancies were invariably left in the wake of quasi-channeled knock-on atoms near the cluster. It was not uncommon to find that a cluster of 8 to 9 vacancies would be enveloped by approximately 10 closely deployed mobile vacancies, most of which attached themselves to this cluster during annealing. Because it appears that clusters of 8 to 9 vacancies and larger grow during annealing at elevated temperatures, it is reasonable to expect that such clusters should not anneal out during irradiation at elevated temperatures. The results on cluster size distribution should, therefore, be pertinent to other than cryogenic irradiation temperatures. Furthermore, while mobile defects should anneal out during elevated-temperature irradiation by high-energy neutrons, these results indicate that the damage associated with large clusters should not. This bears on irradiation hardening and suggests hardening could increase with irradiation temperature in pure samples. As will be shown, the differences between high- and low-energy irradiation of small samples is even more striking in this regard.

A decomposition of the total number of PKA produced in an average neutron collision history into the individual contributions made by each neutron collision order proves to be very informative. In this respect the set of PKA produced by the n-th order neutron collision will be denoted by PKA_n. The displacement productivity of the PKA contained in PKA_1 is particularly important. Nearly all displacements are created by PKA_1 in small samples and the number of displacements produced by PKA_1 in large finite samples is at least twice as large as the number produced by any other set $PKA_{n>1}$. The PKA_1 energy

*A. Seegar, "The Nature of Radiation Damage in Metals," *Radiation Damage in Solids*, International Atomic Energy Agency, Vienna, 1962, p. 101.

spectrum in small samples is significantly affected by the sample size because neutrons from a distributed source with energies above 0.25 Mev tend to be preferentially transmitted without collision. This loss is especially severe for 0.6 to 2.5 Mev neutrons. Most of the PKA in small samples are, therefore, produced by a set of neutrons whose energy spectrum is softer than that of the incident (exposure) neutron spectrum.

PKA and displacement production for each of the first five neutron collisions in a semi-infinite medium are described by Table 3.6 for isotropically incident 1 Mev and 0.1 Mev neutron irradiation. These energies are close to the average neutron energies 0.943 Mev and 0.108 Mev for the ETR and ORGR spectra, respectively. Y_n denotes the number of PKA produced per incident neutron by n-th order collisions and the number of displacements produced by these PKA is represented by D_n. Note that the cumulative PKA production, $\Sigma_n Y_n/Y$, and displacement production, $\Sigma_n D_n/D$, build up slowly as the neutron-collision chain unfolds and that displacement production proceeds at a faster rate than does PKA production. If the straight-line log-log plot of the data in Table 3.6 is extrapolated to obtain an estimate of the lower boundary on the number of collisions required for complete PKA and displacement production, the indication is that at least 25 collisions are required to fill out displacement production and about 100 collisions to complete PKA production, in a semi-infinite medium. This collision order analysis for 1 Mev and 0.1 Mev neutrons clearly illustrates that the PKA produced in the initial stage of a neutron-collision history largely determine the total displacement production. In addition, Table 3.5 shows that neutrons with energies below 0.1 Mev, in a distributed spectrum, do not make a significant contribution to either the total displacement production, or the production of large vacancy clusters.

TABLE 3.6

PKA AND DISPLACEMENT PRODUCTION FOR THE FIRST FIVE COLLISION ORDERS OF 1 Mev (I) AND 0.1 Mev (I) NEUTRONS IN A SEMI-INFINITE IRON MEDIUM[a]

n	Y_n	$\Sigma_n Y_n/Y$	D_n	$\Sigma_n D_n/D$	$(D/Y)_n$
1 Mev (I)					
1	0.995	0.035	515	0.096	518
2	0.755	0.061	385	0.168	510
3	0.650	0.084	325	0.228	500
4	0.550	0.103	275	0.280	500
5	0.530	0.122	265	0.329	500
Y = 0.0667		D = 33.8	D/Y = 507		
0.1 Mev (I)					
1	0.992	0.041	69.8	0.105	70.4
2	0.746	0.072	51.2	0.182	68.6
3	0.651	0.098	43.2	0.247	66.4
4	0.533	0.120	33.9	0.298	63.6
5	0.504	0.141	31.3	0.345	62.1
Y = 0.129		D = 8.94	D/Y = 69.3		

[a]The values of Y, D, and D/Y are those for complete neutron histories; n denotes the neutron collision order.

The steady decrease in Y_n is caused predominantly by neutron loss via reflection rather than by absorption or slowing down to energies too low to produce PKA. Table 3.7 provides a detailed description of this reflection loss. In contrast to the slow buildup of PKA and displacement production, the reflection loss fraction builds up rather quickly during the first few collisions, attaining about 60 percent of its ultimate value R in the course of four collisions. The log-log plots of the data in Table 3.7 did not fall on a straight line, as did

TABLE 3.7

NEUTRON REFLECTION FOR THE FIRST FOUR COLLISION ORDERS OF 1 Mev (I) AND 0.1 Mev (I) NEUTRONS IN A SEMI-INFINITE IRON MEDIUM[a]

n	$\Sigma_n R_n$	$\Sigma_n R_n/R$	R_n/R
1 Mev (I)			
1	0.2193	0.271	0.271
2	0.3433	0.424	0.153
3	0.4153	0.512	0.058
4	0.4631	0.572	0.060
t	0.8106	1.000	-
0.1 Mev (I)			
1	0.2437	0.295	0.295
2	0.3479	0.421	0.125
3	0.4355	0.527	0.106
4	0.4852	0.588	0.061
t	0.8264	1.000	-

[a]The value R is the reflection fraction for a complete neutron history; n denotes the neutron collision order.

those for the data in Table 3.6. An exponential curve extrapolation of the data in Table 3.7 gave a lower boundary of approximately 30 collisions for the completion of neutron reflection.

Infinite and Semi-Infinite Media: Distributed Sources - In addition to the influence of neutron energy, the influences of the incident-neutron angular distribution and the neutron-scattering angle distribution were also considered in the distributed source calculations. The principal results are summarized in Tables 3.8 and 3.9. The letter I in parenthesis after a spectrum designation indicates isotropic neutron incidence and the letter N, normal

TABLE 3.8

DAMAGE PARAMETERS FOR ETR AND ORGR IRRADIATION OF A SEMI-INFINITE IRON MEDIUM

	ETR (I)	ETR (N)	ETR (N)[a]	ETR$^{\infty}$[b]	ORGR (I)
R	0.788[c]	0.708[c]	0.751[c]	-	0.806[c]
$\langle E \rangle$[d]	14.0	13.3	15.9	9.23	3.99
E_{eff}[e]	10.5	10.1	10.8	7.30	3.50
Y	19.6	27.2	21.5	81.5	7.85
D	3772	5021	4212	11,013	528
D/Y	192	185	196	135	67.2
K*[f]	0.0647	0.0600	0.0822	0.0366	0.0117

[a]Isotropic neutron scattering.
[b]Infinite medium.
[c]Fraction of incident neutrons with energies above 350×10^{-6} Mev which were reflected with energies above 350×10^{-6} Mev.
[d]Average PKA energy, kev.
[e]PKA energy which would give a number of displacements equal to D/Y, kev.
[f]Large cluster factor: $K^* \cong 1-F^*$.

TABLE 3.9

RELATIVE NUMBERS OF DISPLACEMENTS AND PKA ASSOCIATED WITH FOUR PKA ENERGY RANGES

ΔE, kev	ETR(I)	ETR(N)	ETR(N)[a]	ETR∞[b]	ORGR(I)
Fraction of all displacements produced by PKA in energy range indicated.					
0 - 1.1	0.014	0.015	0.015	0.023	0.058
1.1 - 12	0.175	0.183	0.151	0.227	0.324
12 - 56	0.481	0.484	0.423	0.485	0.447
>56	0.330	0.318	0.411	0.265	0.171
Fraction of all PKA produced in energy range indicated.					
0 - 1.1	0.4068	0.4123	0.4445	0.5000	0.6604
1.1 - 12	0.3299	0.3342	0.3344	0.3192	0.2601
12 - 56	0.1986	0.1935	0.1711	0.1442	0.0678
>56	0.0647	0.6000	0.0822	0.0366	0.0117

[a]Isotropic neutron scattering.
[b]Infinite medium.

incidence. When ETR neutrons entered the sample at normal incidence the number of displacements per incident neutron increased by 33 percent above that for isotropic incidence, and the fraction of neutrons lost via reflection dropped by about 10 percent. Because the reflection of normally incident neutrons is less than that for isotropically incident neutrons, i.e., the first-collision density spatial distribution penetrates further into the sample, the damage characteristics for ETR(N) irradiation tend to resemble those in the fourth column for the infinite ETR source. This tendency can be almost totally reversed by substituting isotropic center-of-mass neutron scattering for the actual anisotropic scattering distribution, as is shown by a comparison of the first two columns of Table 3.8 with the third column. This reversal is not quite complete because the average energy transfer in the isotropic scattering mode is larger than that for anisotropic scattering. In a semi-infinite medium, the use of isotropic scattering decreases the total number of displacements because the reflection loss is then augmented relative to that associated with anisotropic scattering. The converse of this behavior occurs in finite samples, because the PKA_1 energy spectrum is hardened by isotropic scattering, and displacement production by PKA_1 is the major displacement mode in small samples.

The fraction of all displacements created by PKA (Table 3.9), in the same four energy ranges previously used, behaves in a way consistent with the interpretation made of the data in Table 3.8. Collision history truncation via reflection during the first few collisions serves to increase the relative displacement contribution of PKA with energies above E^*, both for isotropic incidence with anisotropic scattering, and normal incidence with isotropic scattering. High-energy neutron reflection is more severe in the case of isotropic scattering than in the other two instances as is evidenced by the relative decrease in the displacement contribution of the 1.1 to 56 kev PKA energy range and the relative increase in the contribution of the range above E^*.

As previously mentioned, the average energies of the ETR and ORGR spectra used are 0.943 Mev and 0.108 Mev, respectively. The relative softness of the ORGR spectrum accounts for the drastic changes in the amount and the state of damage induced per neutron from the ORGR spectrum relative to that per neutron from the ETR spectrum. The increased reflection, in the case of the ORGR spectrum, is consistent with the rise in reflection with decreasing neutron energy obtained in the monoenergetic source calculations. It is interesting to note that while the fraction of all displacements produced by PKA with

energies below 1.1 kev is only 0.058, for ORGR (I) irradiation, about two-thirds of all PKA are produced with energies less than 1.1 kev, and that the fraction 0.0117 of the PKA created with energies above E* produce 17 percent of all the displacements. One sees that relatively minor changes in the magnitude of F(E) for E > 12 kev produce significant changes in the relative displacement production contributions.

As mentioned previously, the damage state produced in a small iron sample is generated mainly by PKA_1. (To be strictly correct one must amend this statement to say that PKA with energy spectra very similar to that of PKA_1 produce the damage state in small iron samples.) Hence, a comparison of the damage state produced by PKA_1 with that produced by the combination of sets $PKA_1, \ldots, PKA_n, \ldots$, in an infinite medium, should give a reasonably good qualitative picture of how the damage state in a small sample differs from that in an infinite medium. One should bear in mind, however, that this comparison does not account for the softening of the PKA energy spectra in small samples caused by uncollided transmission of high-energy neutrons. In essence, this comparison serves to illustrate purely the effect of neutron collision history truncation via neutron reflection.

In an infinite medium, D/Y = 135 and K* = 0.0366 (Table 3.8) when the ETR neutron spectrum is used. The first figure corresponds to an average PKA cascade damage region volume equal to 4496 Ω, and the second figure indicates that 3.7 percent of the PKA produced are capable of creating v* clusters. (The probability that a PKA capable of producing a v* cluster will actually do so is about 0.1 according to Program CASCADE results.) In the case of first collisions, however, the D Y value associated with PKA_1 is 306 displacements per PKA, which corresponds to an average damage region volume equal to 10,190 Ω. Furthermore, 12.5 percent of the PKA_1 can produce v* clusters. The damage state produced by PKA_1 is, therefore, composed of damage regions whose average volume $\bar{V}_1$ is 2.27 times the average PKA damage region volume $\bar{V}$ associated with a complete neutron collision history. In addition, 3.38 times as many v* clusters are produced by a PKA from PKA_1 than by a PKA from the union of all PKA_n produced in a complete collision history. These results together with those from a similar comparison for 1 Mev and 0.1 Mev irradiation of a semi-infinite medium are given in Table 3.10.

TABLE 3.10

FIRST COLLISION AND COMPLETE HISTORY FOR D/Y AND K*

	ETR Infinite		ETR (I) Semi-Infinite		0.1 Mev (I) Semi-Infinite		1.0 Mev (I) Semi-Infinite	
Parameter	FC[a]	CH[b]	FC	CH	FC	CH	FC	CH
D/Y	306	135	306	192	70.4	27.3	518	188
FC/CH	2.3	-	1.6	-	2.6	-	2.8	-
K*	0.125	0.037	0.125	-	0	0	0.173	0.018
FC/CH	3.4	-	1.9	-	1	-	9.6	-

[a]FC - First collision only.
[b]CH - Complete history

Finite Samples

The finite sample calculations were done in conjunction with an experimental study on the mechanical properties of iron and tungsten samples irradiated in the ETR. The usual procedure of running complementary experiments on the annealing of radiation-induced resistivity and of making transmission electron microscope observations on the behavior of dislocations in films prepared by thinning bulk samples was adopted in this investigation. A recent paper by Kuhlmann-Wilsdorf et al.,* shows the importance of also including high-

*D. Kuhlmann-Wilsdorf, H. J. Levinstein, W. H. Robinson, and H. G. F. Wilsdorf, "Experimental Verification of Theories on Dislocation Behaviour of Strained f.c.c. Metals," *J. Aust. Inst. Met.*, Vol. 8, 1963, p. 102.

resolution etch pit observations, as successive layers of material are removed from bulk samples, in a study of dislocation behavior.

Resistivity measurements are almost invariably made on irradiated wires, mechanical property measurements on either irradiated rod or sheet stock samples, and the films used in electron microscope work are usually prepared by thinning irradiated foils. Because the initial irradiated samples used in each of these companion investigations are of markedly different dimensions, it is possible that the damage states concerned and/or observed in each instance are not equivalent, even though all samples were subjected to a common irradiation exposure. If this were true, the intended information gain that is expected to be achieved in a complementary measurement procedure would be seriously vitiated.

One of the principal motivations for the finite sample study was to find out if a significant difference in the damage state produced by neutron irradiation could arise purely as an effect of sample size and, if this were the case, to establish the conditions for obtaining equivalent damage states in samples of different sizes and shapes. The present results indicate that the damage states in wires and columns (rods) are usually equivalent, but that a significant difference can exist between the damage state produced in foils or sheets relative to that produced in wires or columns. This difference is essentially manifested in the amount of exposure required to establish the homogeneous damage state. A second motivation was to estimate how valid is the use of either small sample data or the results of infinite medium calculations in predicting the damage state in a reactor pressure shell. The results applicable to pressure shells are incomplete because they do not describe the macroscopic spatial distribution of damage as a function of position in a thick slab irradiated only at one surface. The Monte Carlo program is being revised to give the PKA yield and energy spectrum, together with the energy spectrum of the neutrons producing these PKA, as a function of position in a thick slab.

Most of the slab and columnar samples treated were sufficiently small that a uniform damage distribution could be assumed. In these instances, the PKA density y, defined by Equation (3); the vacancy density d, defined by Equation (2); and the v* cluster density c* of Equation (11) were computed, each quantity being that produced per unit exposure (flux-sec). In addition, D/Y and the exposure ϵ_t, required to produce the transition from the heterogeneous to the homogeneous damage state during irradiation at liquid-helium temperature were computed. Two damage states are defined to be equivalent if they exhibit the same values for d, c*, and D/Y. This definition of equivalence ignores the possibility that the small vacancy cluster size distributions in two samples could be different even though the three equalities used to define equivalence were satisfied. However, it turned out that for a given neutron spectrum the small cluster size distribution appeared to be largely insensitive to changes in the size of the sample and the incident neutron angular distribution. Unless it is specifically stated otherwise, it can be assumed that variations in the small cluster size distributions were found to be insignificant.

The v* cluster density c* per unit exposure is defined to be:

$$c^* = y\,(1 - F^*)/10 \tag{11}$$

the factor 1/10 being the conditional probability that a PKA with energy above E* will produce a vacancy cluster v*. This factor was estimated from Program CASCADE results. The average volume of damage material per PKA is:

$$\overline{V} \doteq 33.3\ D/Y\ \Omega \tag{12}$$

and the damaged material volume per unit exposure per unit volume of material is $y\overline{V}$. Immediately one obtains:

$$\epsilon_t = 1/y\overline{V} = 1/d \tag{13}$$

as the exposure required for PKA damage region overlap, i.e., for a transition to the homogeneous damage state.

Displacement Density - Figure 3.20 describes the displacement density produced in slabs and columns by ETR irradiation for both isotropic and normal neutron incidence. Let d_s and d_c be the displacement densities in slabs and columns, respectively, and (I) and (N) refer to isotropic and normal neutron incidence as before. For $0.01 \leq b \leq 0.4$ centimeter, $d_c(I)$ is nearly constant, but $d_s(I)$ is strongly size dependent over the entire range considered. The ratio $d_s(I)/d_s(N) \geq 2.0$ for $t \leq 1.65$ centimeters and $d_s(I)/d_c(I) \geq 2.0$ for $t = b \leq 0.1$ centimeter. A run was made for a 2 by 2 by 0.02 cm foil to see if d_f for a foil of finite lateral extent would remain significantly larger than d_c for a 0.02-centimeter column (wire). The value $d_f(I) = 500 = 2\, d_c(I)$ was obtained. Neutrons entering the 0.02-centimeter-wide edge surfaces of this foil gave $d_f(I)$-edge = 312, a value 25 percent larger than $d_c(I)$. The dashed curve in Figure 3.20 gives the approximate behavior of $d_f(I)$ for $0.01 < t < 0.04$ centimeter. These results indicate that d(I) is markedly different in foils and wires of the same thickness and that the damage state is a function of the incident-neutron angular distribution in slabs. These differences are sufficiently large (at least a factor of 2) that they should be experimentally detectable. Furthermore, it appears

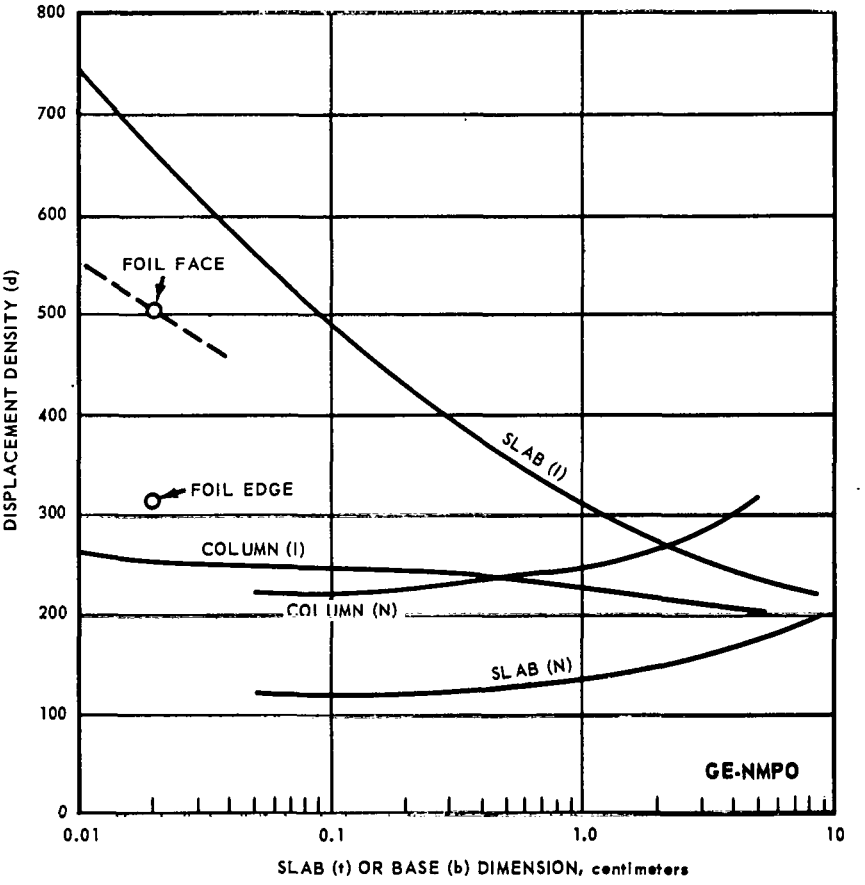

Fig. 3.20 – Displacement density, d, in iron columns and slabs subjected to ETR spectrum type irradiations.

that the damage state of isotropically irradiated wires and rods should be nearly equivalent in view of the constancy of d_c (I) over the interval $0.01 \leq b \leq 0.4$ centimeter. The ensuing discussion will show that since c* behaves in the same way as d, and since D/Y is nearly constant over a wider dimensional range than d, the equivalence for wires and rods is in fact complete. d_c (N) is nearly constant for $0.05 \leq b \leq 0.2$ centimeter, but its behavior for $b \leq 0.05$ could not be reliably estimated from the data at hand. Isotropic neutron scattering with iron was assumed for ETR (N) irradiation to estimate the effect of anisotropic scattering on displacement production. In the case of slabs, d (isotropic) was 52 percent larger than d (anisotropic) and in the case of column, 44 percent larger.

Displacements Per PKA - Except for ETR (N) irradiated slabs, D/Y was nearly constant for dimensions in the range 0.02 to 1 centimeter. D/Y for ETR (N) irradiated slabs decreased monotonically from an extrapolated value of 215 at t = 0.02 centimeter to 185 at t = 8 centimeters. The average <D/Y> over various dimensional ranges for slabs and columns is described by Table 3.11.

TABLE 3.11

AVERAGE VALUE <D/Y> OF D/Y OVER THE SAMPLE DIMENSION RANGES SPECIFIED

Spectrum	Shape	<D/Y>	Dimension Range, cm
ETR (I)	Column	215	$0.02 < b < 1.0$
ETR (N)	Column	215	$0.05 < b < 1.6$
ETR (I)	Slab	235	$0.02 < t < 1.25$
ETR (N)	Slab	205	$0.05 < t < 1.0$

Large Cluster Density - Program CASCADE results indicate that v* contains 15 vacancies in iron. The v* cluster density c* is plotted for slabs and columns in Figures 3.21 and 3.22, respectively. c* is nearly constant in columns for $b \leq 1$ centimeter, but is size dependent in slabs. Isotropic neutron scattering gave a v* cluster density about twice that given by anisotropic neutron scattering.

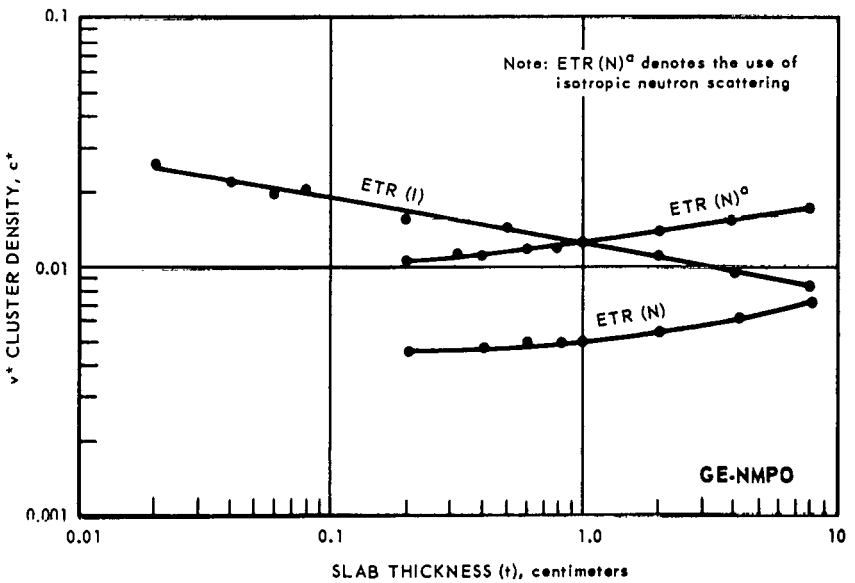

Fig. 3.21 – Large cluster density, c*, in iron slabs subjected to ETR spectrum type irradiation

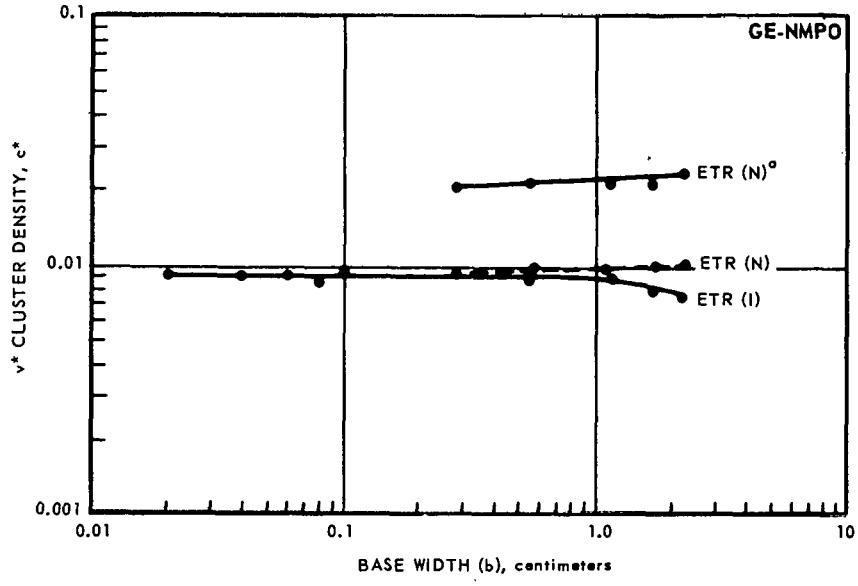

Fig. 3.22 – Large cluster density, c*, in iron columns subjected to ETR spectrum type irradiation

Exposure for Homogeneous Damage State - The exposures ϵ_t required to establish a homogeneous damage state at liquid-helium temperature are plotted in Figure 3.23 for slabs and columns. One notes that the exposure required to give a homogeneous state in wires is at least twice that required for foils, and that ϵ_t is the same for wires and columns provided b ≤ 0.3 centimeter. ϵ_t for isotropic neutron scattering was about 70 percent that for anisotropic scattering.

0.28-Centimeter Column

A column of length h = 6.35 centimeters and base dimension b = 0.28 centimeter was chosen as being the appropriate creep-rupture or tensile test specimen size for ETR (I)

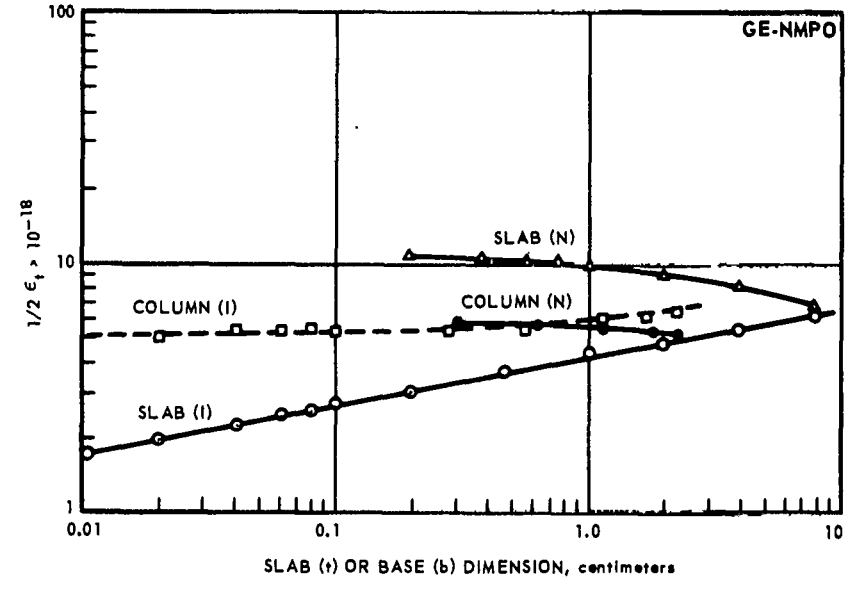

Fig. 3.23 – Exposure, ϵ_t, required to produce a homogeneous damage state in iron slabs and columns for ETR spectrum type irradiation at 0°K

irradiation experiments in order that the damage state be equivalent to that in the wire or rod samples used in the companion radiation-induced resistivity study. As indicated in the previous section, the choice of a sheet-stock creep-rupture test sample would not have been appropriate in this regard. Damage state calculations for monoenergetic and distributed neutron energy sources were performed. Because of the present general interest in the mechanical properties of neutron irradiated iron and because this particular sample size is an appropriate size for complementary measurement studies, the results of these calculations will be discussed in detail.

Monoenergetic Irradiation - Nearly all PKA were produced by neutron first collisions in the column. Second-order neutron collisions produced about 4.6 percent of the PKA in the column for neutron energies $E \geq 0.32$ Mev and 9.7 percent of the PKA for $E \leq 0.32$ Mev. It is important to recognize that, except for the PKA yield, the results of the monoenergetic calculations were not influenced by preferential uncollided transmission of high-energy incident neutrons.

The quantities Y, d, c*, and ϵ_t are plotted in Figure 3.24 versus neutron energy for isotropic incidence. Note that Y decreases with neutron energy and closely follows the variations in the neutron cross section (Appendix B). This behavior is opposite to that shown in Figure 3.18 for a semi-infinite medium, wherein Y increased with neutron energy. As will be shown, this decrease is caused by the uncollided transmission of high-energy neutrons. D/Y and D varied with neutron energy as shown in Figure 3.25. The magnitude of D/Y in the column was roughly 1.5 times that in the semi-infinite medium, for neutron energies above 1 Mev, and 2.6 times the semi-infinite medium value for lower neutron energies. At each neutron energy, K* assumed a larger value than that for the semi-infinite

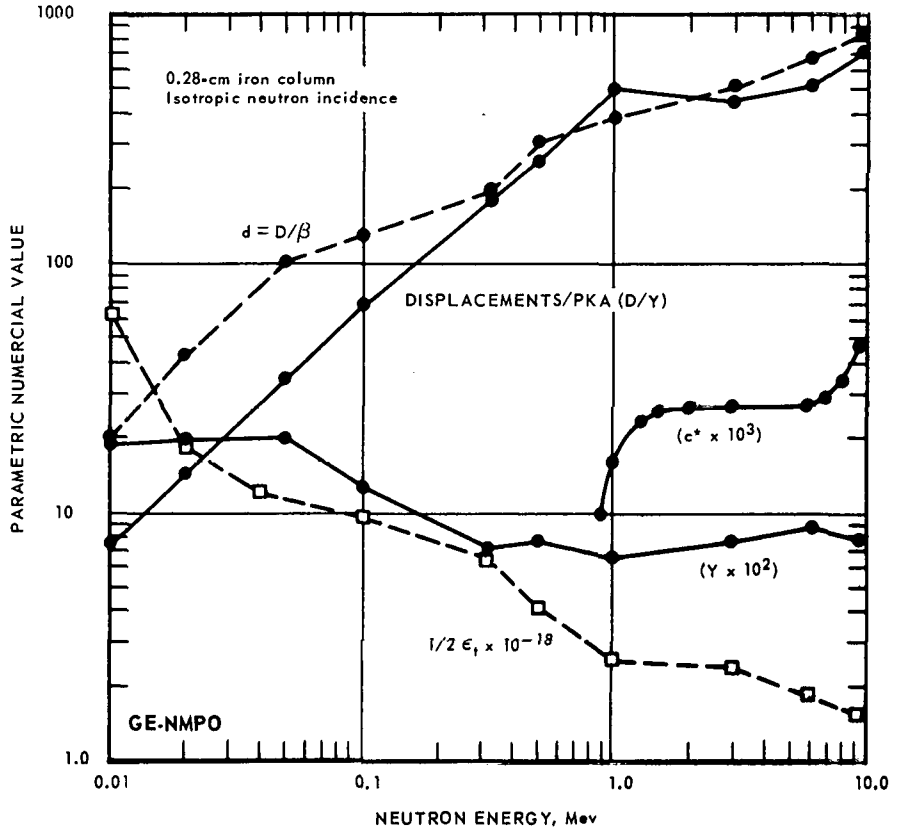

Fig. 3.24 – Damage parameters for a 0.28-centimeter iron column as a function of neutron energy for isotropic neutron incidence

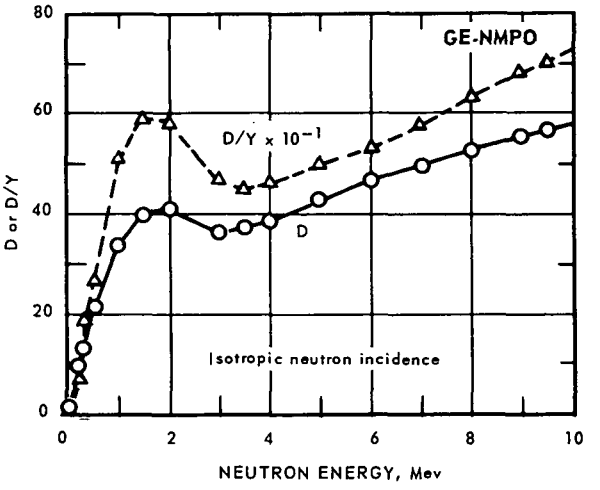

Fig. 3.25 – Variation of D and D/Y in a 0.28-centimeter iron column as a function of neutron energy

medium. These results indicate that the damage state in small samples differs significantly from that in large samples. The following discussion deals with these differences as they are manifested in K*, D/Y, and the relative displacement production by PKA in four different energy ranges. Particular emphasis will be placed on differences in the size distribution of the PKA cascade damage region volumes.

The behavior of K* as a function of neutron energy was quite interesting. If the average energy transfer fraction for elastic neutron collisions were energy independent, K* would increase monotonically with neutron energy. However, Figure 3.26 shows that K* exhibited a relative maximum at ~ 2 Mev and increased monotonically only for E > 4 Mev. A consideration of this maximum and those in Figure 3.25, should be important in analyzing the damage state produced in finite samples exposed to fission spectrum neutrons. This maximum occurred as a consequence of the way the neutron scattering angle distribution varies with energy in iron. As the neutron energy rises from 0.8 Mev to 3 Mev, there is a rapid transition from a semi-isotropic neutron scattering mode, in the center-of-mass system, to a highly forward scattering mode which persists up to 10 Mev. This causes a monotonic

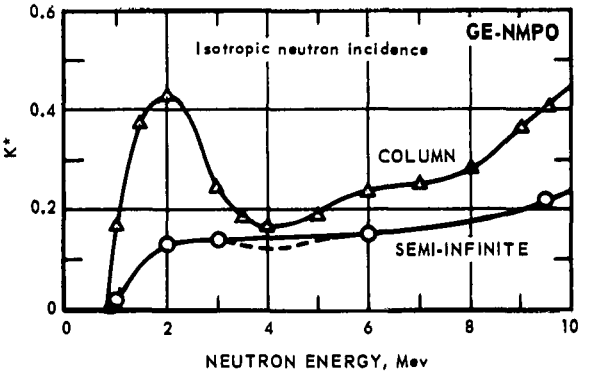

Fig. 3.26 – Variation of K* in a semi-infinite iron medium and a 0.28-centimeter iron column as a function of neutron energy

depression of the average energy transfer fraction, and therefore, impresses an attenuating effect on K*, with increasing neutron energy. As previously stated, neutron first collisions produce nearly all PKA in the column and the competition between the opposing effects noted above is directly manifested in the relative maximum of K* at 2 Mev. Because the PKA spectrum in a semi-infinite medium is the super-position of the individual PKA spectra produced by each of many neutron collision orders, the K* curve, in this case, appears to rise monotonically with neutron energy, and also lies below that for the column. It is possible that a slight dip occurs at approximately 4 Mev in the semi-infinite medium K* curve as is indicated by the dotted line.

The average volume of the cascade damage region produced by a PKA of energy E is:

$$V(E) = V_d\, g(E) \tag{14}$$

where V_d is the damage region volume per displacement. A constant value $V_d = 33.3\ \Omega$ was obtained in Program CASCADE damage studies for $E \geq 1$ kev. It is, therefore, possible to construct the cumulative distribution function G(V) for the cascade damage region volumes, as a function of V/V_d, from F(E) for PKA and the displacement function g(E). Figures 3.27 to 3.30 compare G(V) for a 0.28-centimeter column and that for a semi-infinite medium for 0.5, 1, 2, and 9.5 Mev neutron irradiations, respectively. The vertical ticks on each curve mark the average, $\langle V/V_d \rangle = D/Y$, for the distribution. Because it was assumed that PKA with energies above $E^* = 56$ kev experience only inelastic collisions and those with lower energies only elastic collisions, the fraction K* of all PKA produced constitute a monoenergetic source of 56 kev PKA in the displacement calculations. The abrupt rise above $V/V_d = 980$ in the distributions for 1, 2, and 9.5 Mev is meant to indicate this circumstance and separate the two curves plotted in each figure at $V/V_d = 980$. It does not mean that $V/V_d > 980$ was given by the computational model used.

A discussion of these distributions proceeds most easily if the high-energy cases are considered first. At 2 Mev and 9.5 Mev, the distributions for the column and semi-infinite medium are nearly parallel on the interval $300 < V/V_d < 980$, indicating that the relative

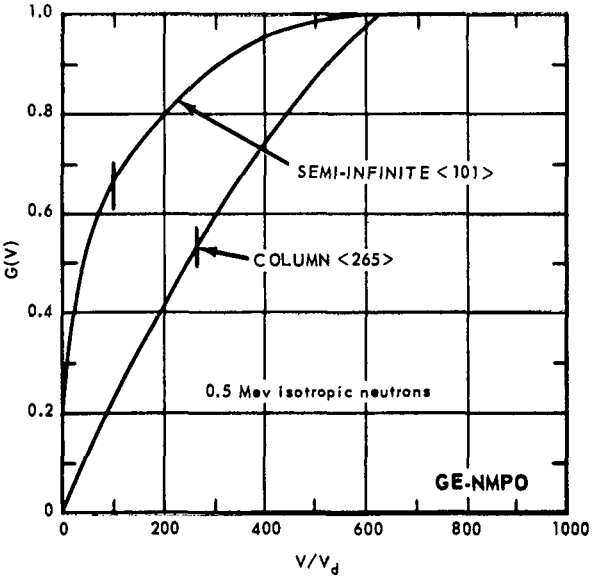

Fig. 3.27 – G(V) for a semi-infinite iron medium and a 0.28-centimeter iron column for 0.5 Mev (I) neutron irradiation

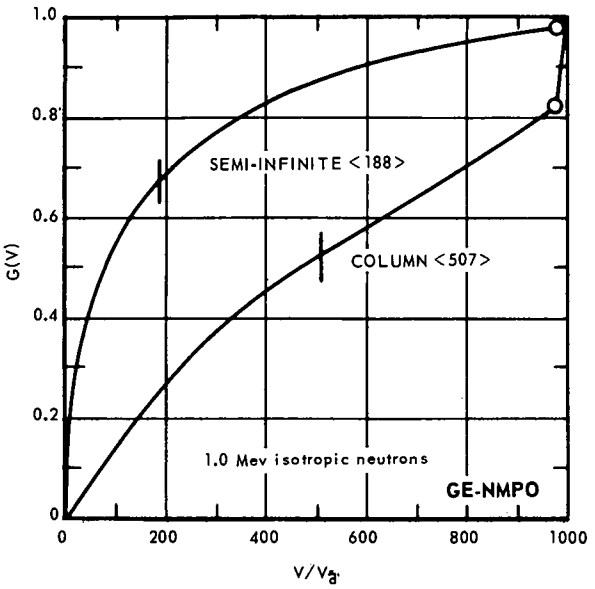

Fig. 3.28 – G(V) for a semi-infinite iron medium and a 0.28-centimeter iron column for 1.0 Mev (I) neutron irradiation

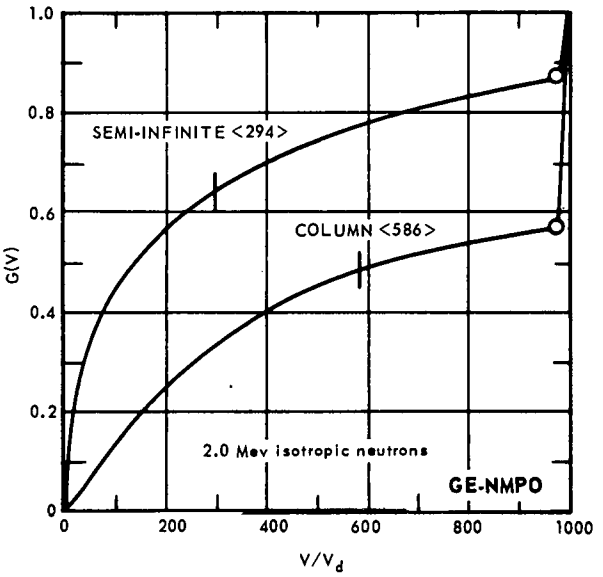

Fig. 3.29 – G(V) for a semi-infinite iron medium and a 0.28-centimeter iron column for 2.0 Mev (I) neutron irradiation

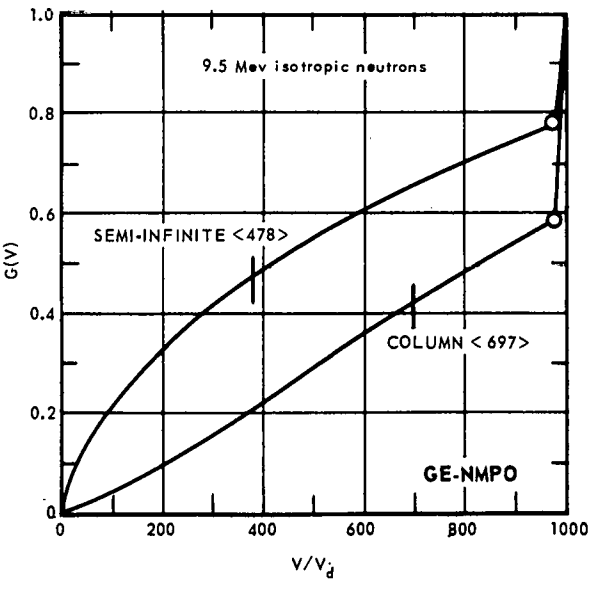

Fig. 3.30 – G(V) for a semi-infinite iron medium and a 0.28-centimeter iron column for 9.5 Mev (I) neutron irradiation

numbers of damage region volumes in this range are substantially the same regardless of sample size. The distributions G(V) for high-energy irradiation differ significantly only for $V/V_d < 300$ and $V/V_d = 980$. Damage region volumes $V/V_d = 980$ dominate the damage configuration in the column, their relative number being over 40 percent of the total number of cascade damage region volumes. At 9.5 Mev, these volumes are surrounded by an environment of lesser volumes, half of which are smaller than $V/V_d = 400$. At 2 Mev, half of the volumes in the environment are smaller than $V/V_d = 240$. On the other hand, only 10 to 20 percent of the cascade damage region volumes attain the maximum size $V/V_d = 980$ in the semi-infinite medium. At 9.5 Mev, their environment is made up of lesser volumes half of which are smaller than $V/V_d = 230$. At 2 Mev, half of the lesser environmental volumes are smaller than $V/V_d = 100$. Perhaps a more direct comparison of these damage pattern differences is conveyed by noting that over 50 percent of the volumes exceed $V/V_d = 630$ in the column, but no more than 21 percent exceed this size in the semi-infinite medium, following high-energy irradiations. The distributions for 1 Mev irradiation exhibit no parallel segments and the relative number of $V/V_d = 980$ volumes for the semi-infinite medium is insignificant. These 1-Mev curves illustrate a transition in the nature of the cascade volume distributions characteristic of high- and low-energy irradiations. Over half of the volumes in the semi-infinite medium are smaller than $V/V_d = 80$, the corresponding figure for the column being $V/V_d = 470$. It can be seen that the character of the distribution for the column at 1 Mev is very similar to that for the semi-infinite medium at 9.5 Mev. The transition in the shape of the volume distribution away from that for high-energy irradiations culminates in the distributions for 0.5-Mev neutron irradiation. In this instance, half of the cascade damage region volumes are less than $V/V_d = 40$ in the semi-infinite medium and those in the column tend to be uniformly distributed. A detailed Monte Carlo computer study on the manner in which these differences in the cascade volume distributions influence the annealing of mobile defects and the size distribution of clusters after annealing is in progress.

A description of the relative number of displacements produced in the column by PKA in the energy ranges 1.1 to 12 kev, 12 to 56 kev, and E > 56 kev is given by Figure 3.31,

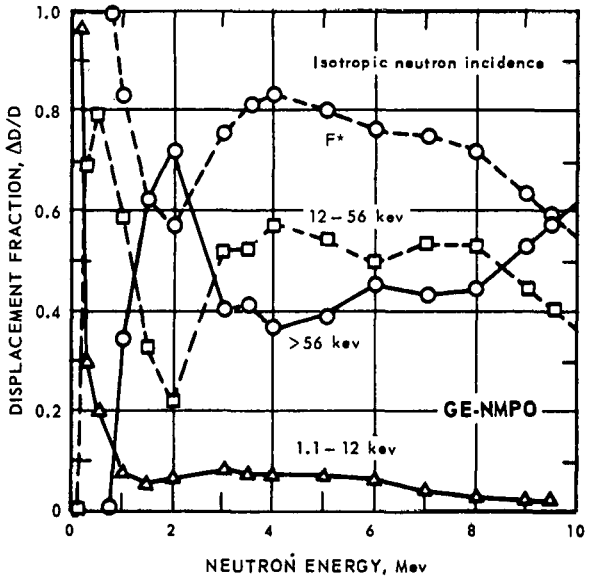

Fig. 3.31 – The fraction ΔD/D of all displacements produced in a 0.28-centimeter iron column by PKA, with energies in the ranges indicated, as a function of neutron energy

the counterpart of Figure 3.19 for the semi-infinite medium. The important feature of a comparison of the curves in these two figures is the pronounced soothing effect of long neutron collision chains in the semi-infinite medium. Once again, there is observed essential distinction between the root factors for damage production in small and large samples.

Distributed Sources - Distributed source calculations were performed to see how the energy dependent characteristics discussed above combine in the presence of preferential uncollided transmission of fast-incident neutrons from distributed sources, i.e., to gauge the extent of softening in the PKA energy spectrum as a result of uncollided transmission. Recall that in an infinite medium the set PKA_1 gave D/Y = 306 and K* = 0.125 for ETR neutrons. In the 0.28-centimeter column, ETR(I) irradiation gave D/Y = 220 and K* = 0.0835 and first collisions produced 91 percent of the PKA, the remainder being produced by second-order collisions. These figures indicate that preferential uncollided transmission of fast neutrons from the ETR spectrum caused a considerable decrease in damage production relative to that predicted by the infinite medium PKA_1 parameters. Using the result that 91 percent of the PKA produced in the column are PKA_2 and the infinite medium parameters, the values $D/Y \geq 278$ and $K^* \geq 0.114$ are predicted for the column, the equality to these numbers corresponding to an assumption of no damage production at all by $PKA_{n>1}$. It is, therefore, clear that preferential uncollided transmission of high-energy neutrons through the column led to a 28 percent decrease in D/Y and a 33 percent decrease in K* relative to the results predicted using the infinite medium PKA_1 parameters. Hence, a first-collision infinite medium calculation overestimates damage production (D/Y) by 40 percent of the true value for the column. Had isotropic scattering been assumed in the infinite medium calculation, the estimate would have been twice the true value. We chose D/Y for this comparison because it determines the exposure required to establish the homogeneous damage state.

In conclusion, the differences in the damage states produced in the 0.28-centimeter column by ETR(I) and ORGR(I) irradiation will be summarized. From Table 3.12 it is seen that the average size of a PKA cascade damage region is much smaller in an ORGR(I) irradiated sample than in one subjected to ETR(I) irradiation. This and the smaller PKA density, y, for ORGR(I) irradiation led to the result that the exposure to ORGR(I) neutrons, required to produce a homogeneous damage state, was four times larger than ϵ_t for ETR(I) irradiation. It was originally thought that the average PKA energy would be a useful index of damage productivity. It was found that this is not the case because this average overestimates the influence of high-energy PKA. An effective PKA energy defined as that PKA energy leading to D/Y displacements is a better index. The ETR(I) produced c* is about an order of magnitude larger than that produced by ORGR(I) irradiation. However, at the respective exposures ϵ_t for the two spectra, the large cluster concentration in an ETR(I) irradiated column reduces to 1.7 times that in an ORGR(I) irradiated column.

The fractions $\Delta D/D$ of all displacements produced by PKA with energies in each of four different energy ranges are listed in Table 3.13. It is because of the relatively greater fraction (factor of 1.74) of displacements caused by PKA with energies above 56 kev and

TABLE 3.12

DAMAGE STATE CHARACTERISTICS FOR A 0.28-CM IRON COLUMN SUBJECTED TO ETR AND ORGR TYPE IRRADIATION

Spectrum	D/Y	d	$c^* \times 10^3$	$t \times 10^{-18}$	y	<E>, kev
ETR(I)	220	242	9.2	10.64	1.10	16.6
ORGR(I)	62.7	58.5	1.3	21.9	0.93	3.3
ETR(I)/ORGR(I)	3.51	4.14	7.1	0.486	1.2	5.0

TABLE 3.13

RELATIVE NUMBER OF DISPLACEMENTS PRODUCED IN A 0.28-CM IRON COLUMN

PKA Energy, kev	ΔD/D, % ETR(I)	ORGR(I)
0 - 1.1	1.3	6.8
1.1 - 12	15.4	31.9
12 - 56	46.2	40.0
>56	37.1	21.3

the relatively small fraction (factor of 0.48) caused by PKA with energies in the range 1.1 to 12 kev, that D/Y for ETR(I) radiation far exceeds that for ORGR(I) irradiation. Distributions of V/V_d for ETR and ORGR irradiation are plotted in Figure 3.32.

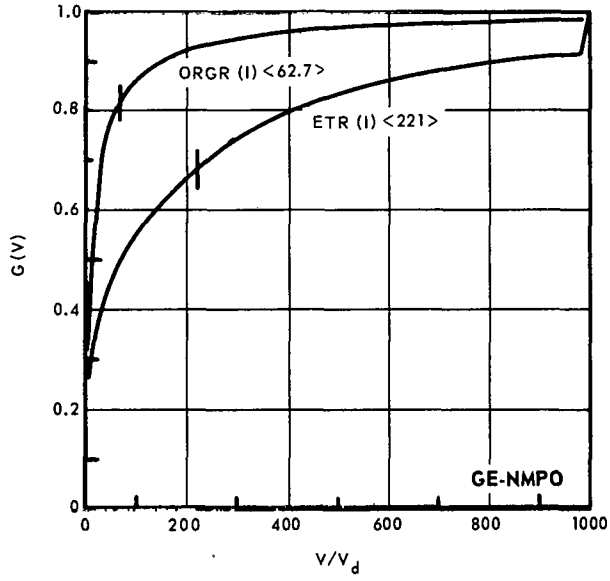

Fig. 3.32 – G(V) for a 0.28-centimeter iron column for ETR(I) and ORGR(I) spectrum type irradiation.

Small Cluster Size Distribution

According to Program CASCADE calculations, the size distribution of vacancy clusters produced by PKA with energies above 5 kev is nearly independent of the PKA energy for the small clusters v_1, v_2, ..., and v_6 where v_n denotes a cluster of n vacancies. Moreover, nearly all vacancies produced were members of these small clusters. This feature makes the small cluster size distribution relatively insensitive to changes in the reactor neutron spectrum as shown by Table 3.14. Only in the instances where neutrons with energies E > 0.10 Mev rarely occurred in the distribution would the small cluster size distribution exhibit a marked change from those listed in Table 3.14. In this regard it is pertinent to recall that the average neutron energy for the ORGR spectrum is 0.108 Mev. Interstitials appeared as isolated defects. The largest interstitial cluster observed contained only three defects.

Sample Size Criteria

The appropriate way to describe the interaction of particle irradiation with matter is largely determined by the average length of a particle collision history associated with

TABLE 3.14

FRACTION OF VACANCIES CONTAINED IN SMALL CLUSTERS v_1 TO v_6 AND THE VALUE OF c* IN A 0.28-CM IRON COLUMN EXPOSED TO ETR AND ORGR IRRADIATION

Cluster Size	Percent Of Vacancies	
	ETR(I)	ORGR(I)
v_1	60.0	62.0
v_2	22.7	22.2
v_3	10.5	9.55
v_4	3.82	3.47
v_5	1.97	1.86
v_6	0.99	0.92
$v_n \geq 3$	17.3	15.8
$c^* \times 10^3$	9.2	1.3

the particular irradiation effects of interest. In this regard there are two extreme cases, one being that in which only the consequences of single collisions are important, and the other being that in which the effects produced in each of a larger number of collisions are important (multiple scattering). The transition region between these two extremes is called the plural scattering domain,* and it is this domain which is pertinent to a description of neutron irradiation damage in finite samples. A simple average chord length treatment is usually sufficient in the case of single-collision domain problems and a diffusion theory treatment is commonly used to describe multiple scattering processes in infinite media. A good description of plural scattering phenomena in finite samples is, however, more difficult. In the neutron plural scattering domain, it is essential to treat each collision in the scattering chain on an individual basis because the free flight distance and scattering angle distributions are usually rapidly changing functions of the particle energy and the particular type of target encountered. These comments bear on the question of defining a small and large sample size because, for a given material and incident-neutron energy-angle distribution, the size of the sample determines the average length of a neutron-collision chain.

The present results indicate that a definition of small and large samples, appropriate to a discussion of neutron irradiation damage, should usually be based on a consideration of the sample size required to cause a transition from the single-collision to the plural-collision domain. In the case of isotropic neutron incidence, instances occur wherein the transition from a domain of less than one collision per neutron to the single-collision domain is a meaningful criterion for distinguishing between small and large samples. Three criteria for defining small and large samples are proposed and evaluated. These criteria are based on the consideration of: (1) the probability for an incident neutron to make at least one collision, (2) the sample size required for an incident neutron to produce a specified number of PKA, and (3) the sample size required for an incident neutron to produce a specified number of displacements.

*H. A. Bethe and J. Ashkin, "Passage of Radiations Through Matter," *Experimental Nuclear Physics*, Vol. I, 1953, p. 287.

First-Collision Probability Criterion - A common rule for distinguishing between large and small samples, on the basis of the neutron first-collision density, is to regard a small sample as one with dimensions less than a characteristic neutron mean free path. This is, in principle, an easy rule to use and it is found that its predictions are in fair agreement with a more appropriate but less easily applied criterion, the application of the latter criterion being limited in the sense that its use requires a computer. In the case of a slab irradiated by normally incident, monoenergetic neutrons, the mean free-path rule specifies a first-collision probability $p_1 \leq (1 - 1/e) = 0.632$ for small samples. In general, the first-collision probability is:

$$P_1 = \int_S dr_S \int_{S_o} dr_o \int_{\Omega} d\vec{\Omega} \int_0^{\infty} dE \left\{1 - e^{-\Sigma(E)\,[r_S(\vec{\Omega}) - r_o]}\right\} x \left[f(r_o)\, g(\vec{\Omega})\, h(E)\right] \qquad (15)$$

where

r_S = a point on the sample surface S
r_o = the neutron entry point on a specified portion S_o of S
Ω = the incident neutron direction into the sample
Σ = the neutron macroscopic cross section
E = the incident neutron energy.

The differential distribution functions f, g, and h characterize the entry point, incident direction, and incident energy of a neutron. In general, $g(\vec{\Omega})$ will be a function of the neutron energy. This integral is automatically evaluated by the neutron initial weight subroutine of the Monte Carlo program. Table 3.15a lists the dimensions of columns and slabs required to give $P_1 = 0.632$ for ETR irradiation and uniform f. Note that no difference was indicated in the dimensions of slabs and columns for ETR(N) irradiation as must follow from this criterion. This occurrence is one of the principal defects in the mean free-path rule. For slabs, the isotropic incidence thickness is roughly one-half that for normal incidence. Had all neutrons exhibited the same mean free path it would have been exactly one-half the normal incidence thickness since g is uniform for isotropic incidence. Uncollided transmission of neutrons via short chords through the right-angle corners of the column account for the requirement of a relatively large column base dimension. This effect also contributes to a relatively large neutron-escape fraction after the first collision, with respect to that for a slab of the same dimension, and illustrates why a rigorous size definition must give different dimensions for columns and slabs exposed to normally incident neutrons.

TABLE 3.15

UPPER LIMIT ON SMALL SAMPLE DIMENSIONS (CM) GIVEN BY FOUR PROPOSED SAMPLE SIZE CRITERIA FOR ETR IRRADIATION OF IRON SAMPLES

	Material Dimensions, cm			
	ETR(I)		ETR(N)	
Criterion	Column	Slab	Column	Slab
a. First collision	4.6	0.95	2.2	2.2
b. Yield	3.8	1.1	2.6	1.8
c. Unit yield	5-6	1.7	3.4	2.4
d. Damage	6-7	1.5	3.5	2.6

PKA Yield Criteria - The first-collision probability rule does not distinguish between incident neutrons sufficiently energetic to produce PKA and unproductive incident neutrons. This deficiency could be corrected by using the appropriate non-zero lower limit on the energy integral, but the insensitivity to sample shape in the case of normally incident irradiation would remain. A generally more meaningful criterion, free from both defects in the first-collision probability rule, would be to regard a sample as small if the PKA yield were less than that associated with first collisions in an infinite medium. This requirement would automatically pertain only to productive neutrons and would in addition account for the fact that a transparency to productive neutrons remaining after the first collision is certainly an important characteristic of a small sample.

In the case of ETR irradiation, the PKA yield $Y_1(\infty)$ for first-collision neutrons in an infinite iron medium was 0.694. The column and slab dimensions required for this yield are listed in Table 3.15b and those for a unit yield in Table 3.15c. In iron, the dimensions given by the $Y = Y_1(\infty)$ requirement are fairly close to those given by the mean free-path rule, and in addition, they distinguish between columns and slabs when the neutrons enter a sample at normal incidence. As will be shown, the $Y = Y_1(\infty)$ size criterion turns out to be more significant than the unit yield criterion and the term "yield criterion" will hereafter refer to the former size description.

Damage Production Criterion - A natural extension of the yield criterion is a prescription based on the damage produced per first-collision neutron in an infinite medium. The dimensions required such that the number of displacements per incident neutron in finite samples is equal to $D_1(\infty)$ for first-collision neutrons in an infinite iron medium are given in Table 3.15d for ETR irradiation. These dimensions are larger than those given by any of the above mentioned criteria and it appears that the damage criterion is not a good sample size prescription because the length of the neutron collision required to satisfy it exceeds that shown to be characteristic of small samples.

D/Y for slabs is plotted in Figure 3.33 as a function of slab thickness. The dimensions given by the mean free path and yield criteria are indicated by arrows. These two size criteria apparently serve to indicate the termination of a plateau in the D/Y curve. In the case of normally incident radiation, D/Y decreases monotonically with slab thickness up to $t \simeq 2.0$ centimeters and then levels off at a constant value for $t > 10$ centimeters. In this regard, it is pertinent to mention that the total neutron loss fraction (reflection plus transmission) for slabs decreases as t approaches 10 centimeters from below and then levels off at the reflection loss fraction for a semi-infinite medium for $t > 10$ centimeters. No runs were made for $t > 10$ centimeters except for the semi-infinite medium calculation.

Calculations were made for $0.02 < t \leq 80$ centimeters using ETR(I) irradiation. In this instance, a D/Y plateau occurs over the interval $0.02 < t < 1$ centimeter and thereafter the curve falls off to the value for D/Y for a semi-infinite medium, this value being nearly attained at $t = 80$ centimeters. Hence, with respect to the average size of a PKA damage region, and ETR(I) irradiated slab with $t < 1$ centimeter is clearly a small sample and an ETR(N) irradiated slab with $t > 2$ centimeters is a large sample.

The size criteria for columns indicate a transition dimension about twice that of the largest column base dimension considered. Therefore, it is not possible to compare the proposed size criteria in the case of iron columns. D/Y increased monotonically for ETR(I) irradiation and decreased monotonically for ETR(N) irradiation as the column base was increased to 2.25 centimeters. However, in similar calculations for BeO it was possible to compare the transition dimension given by the size criteria with a transition point in the D/Y curve. The column base dimension was allowed to vary up to fixed length dimension $h = 8.9$ centimeters in the BeO calculations. As in the case of iron, D/Y decreased mono-

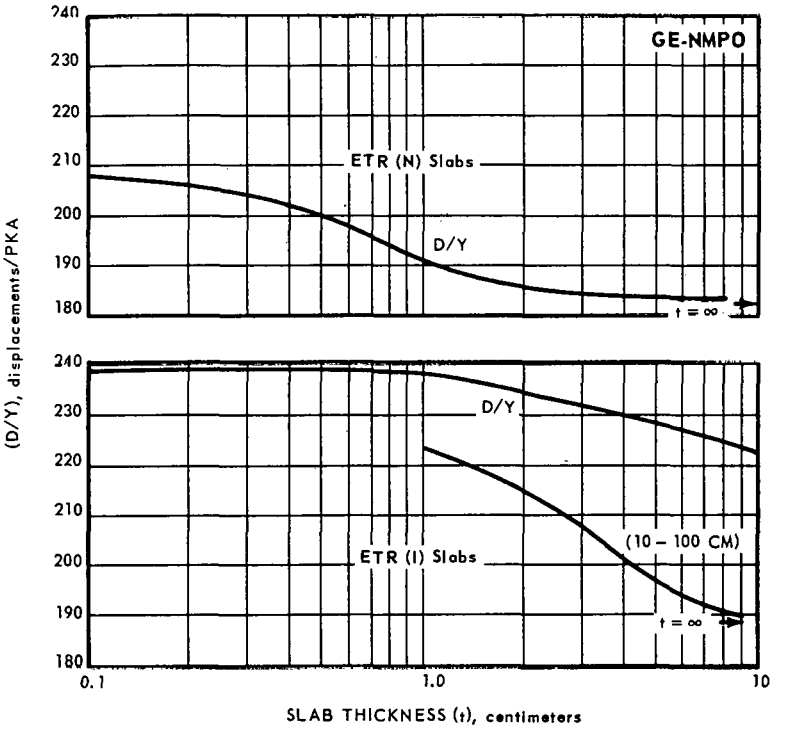

Fig. 3.33 – Variation of D/Y with slab thickness for ETR spectrum type irradiations

tonically for ETR(N) irradiation, but fell off from a plateau on 0.02 centimeter < b < h/4 for b > h/4. The transition dimension given by the yield criterion for ETR(I) irradiation of BeO columns was also h/4, but that given by the mean free-path rule was h/2.

These results for iron and BeO indicate that the proposed yield criterion probably indicates the termination of small sample behavior for the case of isotropic irradiation and the onset of larger sample behavior for the case of normally incident irradiation. The unit yield and damage production criteria do not appear to be useful prescriptions in that the number of collisions required to satisfy them apparently exceeds the average collision chain length pertinent to small samples, as indicated by the D/Y data.

CONCLUSIONS

Irradiation of Mo and Mo-TZM test specimens in contact with reactor moderator water results in a serious corrosion problem.

The effects of neutron irradiation are more pronounced for the case of recrystallized material. For instance, the creep rate of cold-worked irradiated (3.2×10^{19} nvt) tungsten test specimens was reduced by a factor of 1.6 when tested at a temperature of 1100°C. The creep rate of the recrystallized irradiated (2.5×10^{19} nvt) test specimen was reduced by a factor of 2.0 at the same temperature. The corresponding rupture life of the cold-worked irradiated test specimen was increased by a factor of 1.6, and that of the recrystallized specimen was increased by a factor of 2.6.

The elongation and the reduction in area of control and irradiated tungsten specimens did not deviate significantly when compared at the same temperature and stresses.

A 1900°C anneal of an irradiated cold-worked specimen in a hydrogen atmosphere does not completely remove the irradiation-induced hardening when compared to a control specimen which was heat treated at the same time.

Post-irradiation annealing of tungsten resistivity specimens irradiated at 3.3×10^{19} nvt ($E_n \geq 1$ Mev) up to 1900°C did not completely remove all the radiation-induced increase in this property.

The apparent number of defects generated by neutron irradiation at reactor ambient temperatures is linear with neutron dosage from 5×10^{18} to 33×10^{18} nvt.

Surface finish of recrystallized tungsten specimens which were fabricated by grinding does not significantly change the creep rate at 1100°C up to a 0.178-millimeter electrolytic reduction in diameter. Third-stage creep, and consequently the rupture life, was affected more by the electropolishing process.

Stress-rupture studies on A-286, containing various amounts of natural boron and irradiated to a fast neutron dose of about 5×10^{19} nvt, show that the greatest radiation-induced effect occurs in specimens containing the least amount of boron (0.00085%). The rupture life of specimens containing about 0.01 percent boron was within 25 percent of that of the corresponding control data, whereas the life of the specimens having lower boron concentration was reduced about 500 percent. The elongation of both types of specimens was seriously reduced by the irradiation with the greater reduction occuring for the specimen containing the least amount of boron. The second-stage creep rate of the lower boron content specimen was essentially unchanged by the irradiation. However, the irradiation did significantly reduce the creep rate of the higher boron containing specimen.

Perhaps the most important indication given by the computer study is that the difference between the damage states in neutron-irradiated iron samples caused by either differences in sample size, incident-neutron angular distribution, or incident-neutron energy spectra are principally differences in the distribution of the PKA cascade damage region volumes and the V* cluster density. In contrast to expectations, the size distributions of small vacancy clusters in PKA cascade damage regions was very nearly independent of the irradiation conditions unless the energy spectrum of the irradiating neutrons pertained exclusively to neutrons with energies less than 0.1 Mev.

Infinite medium calculations do not give a good estimate of the damage state in a finite sample even when only the damage parameters associated with PKA created by first-order neutron collisions in an infinite medium are used to make the approximation. An exact treatment of uncollided incident-neutron transmission through finite samples must be made in order to properly estimate the damage state produced.

Wires and slabs subjected to the same neutron irradiation energy spectrum and exposure will, in general, exhibit nonequivalent damage states. On the other hand, isotropically irradiated iron wires and rods with diameters less than 0.4 centimeter will exhibit very nearly equivalent damage states when subjected to the same neutron spectrum and exposure.

The heterogeneous damage state produced in large samples is essentially different from that produced in small samples. Specifically the spread in the size distribution of the PKA cascade damage regions about the average size will be much greater in large samples than in small samples. In addition, the absolute number of large clusters produced per incident neutron in large samples greatly exceeds that produced in small samples. These circumstances lead to questioning the direct application of irradiation data and test results for small samples in the design of large structural parts for a reactor.

WORK PLANNED FOR NEXT PERIOD

Creep-rupture testing of Mo and Mo-TZM control and irradiated specimens will be continued.

Room-temperature tensile testing of control and irradiated tungsten specimens after various annealing temperatures will be continued.

The irradiation capsule will be designed and fabrication initiated for the elevated-temperature tungsten creep-rupture specimen irradiations.

Isothermal resistivity recovery studies will be continued on tungsten and W - 25Re specimens. Isochronal studies will continue on Mo and Mo-TZM resistivity specimens. Hardness recovery studies will also be continued on these materials.

Fatigue and creep-rupture testing will continue on the high-temperature alloys.

Computer studies on irradiation defects produced in a tungsten medium will be considered.

APPENDIX A
REACTOR SPECTRA

Partial descriptions of the cumulative distribution functions for the ETR and ORGR neutron flux energy spectra used in these calculations are listed in Table A1. Neutrons with energies less than 3.5×10^{-4} Mev are incapable of producing PKA in iron if a displacement energy of 25 ev and a maximum energy transfer fraction of 0.070 from a neutron to an iron nucleus are assumed. The last entry in Table A1 for each spectrum designates the fraction of these unproductive neutrons. The cumulative distribution functions actually used in the computations were renormalized such that all incident neutrons were productive neutrons and the results then adjusted to a per incident neutron basis for the actual spectra over the energy range 2.54×10^{-8} to 10 Mev.

A multigroup, diffusion theory computer program (G-2) was used to compute the neutron flux spectrum in the ETR at a radial distance of 25.3 centimeters from the central longitudinal axis of the reactor core.*† D. K. Holmes' determination of the neutron-flux spectrum for hole 12 of the ORGR reactor was used to prepare the cumulative distribution function for the ORGR.‡

TABLE A1

CUMULATIVE DISTRIBUTION FUNCTION VALUES FOR THE ETR AND ORGR NEUTRON FLUX SPECTRA

E, Mev	ETR	ORGR
10.0	1.0	1.0
3.6	0.9305	-
3.0	0.8951	0.9985
2.0	0.8757	0.9933
1.0	0.7061	0.9697
0.5	0.6175	0.9356
0.3	0.5675	0.9126
0.1	0.4748	0.8609
0.05	0.4417	0.8137
0.00035	0.2652	0.5309

*W. E. Niomuth, (private communication).

†D. J. Campbell, "Program G-2," GE-ANPD, XDC 58-4-63, 1958.

‡D. K. Holmes, "Measurement of the Neutron Spectrum in Hole 12 of the ORGR," *Solid State Physics*, Vol. 2, 1956, p. 409.

APPENDIX B
TOTAL NEUTRON CROSS SECTIONS AND FORWARD SCATTERING CHARACTERISTICS FOR IRON

A plot of the neutron mean free path in iron as a function of energy as given by the GE-NMPO nuclear data tape,* is shown in Figure B1. A complete description of the 100-group angular distribution functions is too long for presentation here, however, Table B1 and Figure B2 describe the variation in the value of the cosine of the center-of-mass scattering angle for which the cosine cumulative distribution function assumed the value 0.5 as a function of neutron energy. The total neutron cross section is also listed.

Fig. B1 – Neutron mean free path in iron as a function of energy

*R. G. Herrmann, T. A. Hoffman, F. D. Wenstrup, and A. Wilcox, "IBM-7090 Programs to Compile and Modify a Nuclear Data Tape," GE-NMPO, APEX-708, 1961; J. W. Zwick and T. J. Kostigen, "Twenty-Five Group Reactor Nuclear Data Tape," GE-NMPO, APEX-709, 1961.

TABLE B1

THE VALUE OF COS θ[a] FOR WHICH THE CUMULATIVE DISTRIBUTION FUNCTION IS 0.50 AND THE NEUTRON TOTAL CROSS SECTION IN IRON

E[b]	cos θ	Σ, cm-1
9.5	0.8500	0.2827
9.0	0.8553	0.2862
8.0	0.8594	0.2938
7.0	0.8628	0.3025
6.0	0.8663	0.3076
5.0	0.8547	0.3023
4.0	0.8406	0.2943
3.0	0.8192	0.2706
2.5	0.7219	0.2560
2.0	0.4874	0.2469
1.4	0.2295	0.2336
1.0	0.1900	0.2321
0.9	0.1813	0.2318
0.8	0.1967	0.2350
0.7	0.2456	0.2471
0.6	0.2610	0.2612
0.5	0.2572	0.2755
0.4	0.2508	0.2668
0.34	0.2903	0.2602
0.32	0.3067	0.2584
0.30	0.2929	0.2639
0.20	0.0343	0.3381
0.10	0.0800	0.4555

[a] θ = center-of-mass scattering angle.
[b] These energies are the upper limits of some of the 100 energy groups. The The cos θ and values listed are group averages.

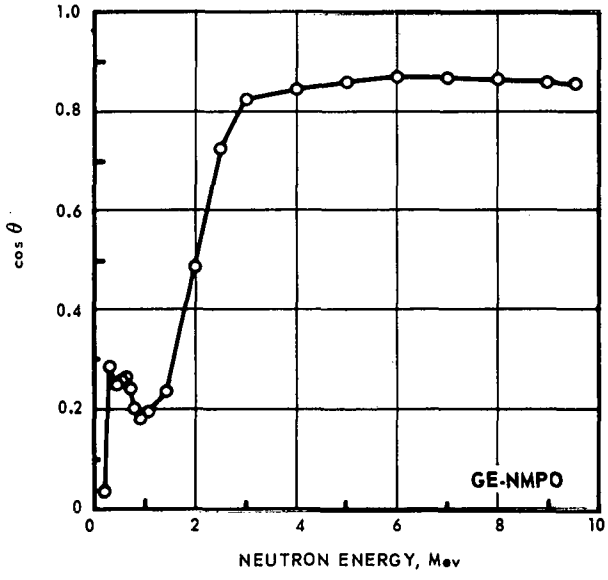

Fig. B 2—Cosine of the center of mass scattering angle for neutrons in iron for which the cumulative distribution function $F(\cos\theta) = 0.5$ as a function of neutron energy—$F(o) = 0.5$ for isotropic scattering

APPENDIX C

The "High-Temperature Materials Program Progress Reports" previously issued in this series are listed below. The first two reports were each issued as one document, containing both the classified and unclassified portion. The subsequent reports were issued as two documents; part A, the unclassified portion and part B, the classified portion.

Report No.	Report Period	Publication Date
NMP-HTMP-1	May 1961 - June 30, 1961	July 15, 1961
GEMP-2	July 1, 1961 - July 31, 1961	August 15, 1961
GEMP-3, A and B	July 1, 1961 - August 31, 1961	September 15, 1961
GEMP-4, A and B	August 1, 1961 - September 30, 1961	October 15, 1961
GEMP-5, A and B	August 15, 1961 - October 15, 1961	November 15, 1961
GEMP-6, A and B	September 15, 1961 - November 15, 1961	December 15, 1961
GEMP-7, A and B	October 15, 1961 - December 15, 1961	January 15, 1962
GEMP-106, A and B (First Annual Report)	Calendar Year 1961	February 28, 1962
GEMP-9, A and B	January 1, 1962 - February 15, 1962	March 30, 1962
GEMP-10, A and B	January 1, 1962 - March 15, 1962	April 16, 1962
GEMP-11, A and B	February 15, 1962 - April 15, 1962	May 15, 1962
GEMP-12, A and B	March 15, 1962 - May 15, 1962	June 15, 1962
GEMP-13, A and B	April 15, 1962 - June 15, 1962	July 31, 1962
GEMP-14, A and B	May 15, 1962 - July 15, 1962	August 15, 1962
GEMP-15, A and B	June 15, 1962 - August 15, 1962	September 14, 1962
GEMP-16, A and B	July 15, 1962 - September 15, 1962	October 15, 1962
GEMP-17, A and B	August 15, 1962 - October 15, 1962	November 15, 1962
GEMP-18, A and B	September 15, 1962 - November 15, 1962	December 14, 1962
GEMP-19, A and B	October 15, 1962 - December 15, 1962	January 25, 1963
GEMP-177, A and B (Second Annual Report)	Calendar Year 1962	February 28, 1963
GEMP-21, A and B	January 1, 1963 - February 15, 1963	April 23, 1963
GEMP-22, A and B	January 1, 1963 - March 15, 1963	April 30, 1963

Report No.	Report Period	Publication Date
GEMP-23, A and B	February 15, 1963 - April 15, 1963	May 31, 1963
GEMP-24, A and B	March 15, 1963 - May 15, 1963	June 20, 1963
GEMP-25, A and B	April 15, 1963 - June 15, 1963	July 31, 1963
GEMP-26, A and B	May 15, 1963 - July 15, 1963	August 16, 1963
GEMP-27, A and B	June 15, 1963 - August 15, 1963	September 30, 1963
GEMP-28, A and B	July 15, 1963 - September 15, 1963	November 11, 1963

ADVANCED TECHNOLOGY SERVICES

GENERAL ELECTRIC